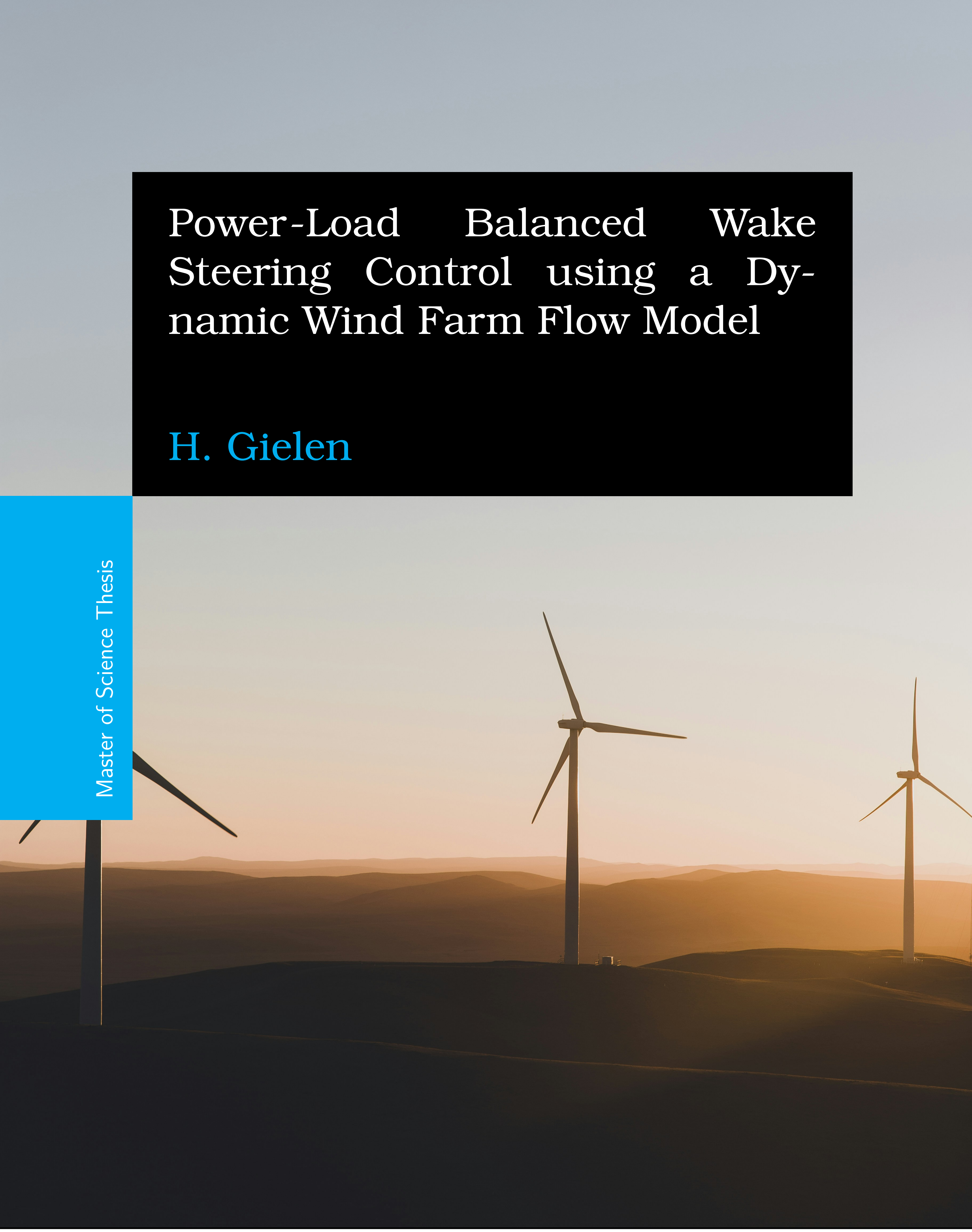

Power-Load Balanced Wake Steering Control using a Dynamic Wind Farm Flow Model

H. Gielen

Master of Science Thesis

TU Delft Delft University of Technology

Delft Center for Systems and Control

Youwind

Power-Load Balanced Wake Steering Control using a Dynamic Wind Farm Flow Model

MASTER OF SCIENCE THESIS

For the degree of Master of Science in Systems and Control at Delft University of Technology

H. Gielen

January 8, 2026

Faculty of Mechanical Engineering (ME) · Delft University of Technology

Abstract

To meet global climate goals, the deployment of renewable energy sources such as wind energy must increase significantly. As wind farms grow in size and density, wake interactions between turbines limit overall performance. Wind Farm Flow Control (WFFC) addresses this challenge with the aim of improving overall wind farm efficiency. Wake steering is a promising control strategy, in which upstream turbines are intentionally misaligned with the wind direction to redirect their wakes away from downstream turbines to increase power production.

Most wake-steering studies rely on steady-state models and focus primarily on power maximization. However, reducing the cost of wind energy also requires extending turbine lifetime, since downstream turbines operating in wake-induced flow experience increased fatigue loading. Aeroelastic simulators can capture these load dynamics, but they are too computationally expensive for control-oriented applications. An efficient alternative is to use load surrogate models that predict fatigue loads from simple inflow and operational quantities. At the same time, the transition from steady-state flow models to dynamic flow models enables the representation of time-varying wake evolution and provides a more realistic environment for evaluating control strategies.

In this thesis, the dynamic wind farm model OFF is coupled with a sector-averaged load surrogate model that predicts damage equivalent loads (DELs) from turbine operation conditions and simple inflow quantities sampled across the rotor plane. The implementation process is described in detail, together with the challenges and limitations encountered. This integrated framework is then used to develop a power-load balanced control strategy that incorporates tower base fatigue loads, and is applied in both the steady state model FLORIS and OFF to assess its performance under more realistic conditions.

A case study with three turbines and three time-varying wind direction signals shows that the resulting *balanced controller* in OFF achieves power gains of up to 12.57% and tower base load reductions of up to 14.40% compared to the baseline. A comparison between FLORIS and OFF reveals that FLORIS provides an upper bound on predicted power gains and load reductions. The structural differences between steady-state and dynamic models explain the observed differences in predicted power and load responses.

Table of Contents

List of Figures

List of Tables

Acknowledgements

First, I would like to thank my supervisor, Jan-Willem van Wingerden, for introducing me to the opportunity to carry out my master's thesis in Barcelona. Exploring a new city and culture alongside my thesis work was a valuable and enriching experience. I am grateful for his guidance and the helpful insights that helped shape the direction of this research.

I would also like to thank my daily supervisor, Daan van der Hoek, for always being willing to help and for consistently making time for me. Your support and feedback were greatly appreciated throughout the thesis process.

I am especially grateful to my supervisors at Youwind, Pieter Gebraad and Thomas Lokken, for taking the time for our weekly meetings. These discussions strongly motivated me to make steady progress and made the research process both engaging and enjoyable. I really appreciated the support, guidance, and positive spirit you brought to our collaboration.

In addition, I would like to thank everyone at Youwind for warmly welcoming me and making me feel included as part of the team.

I am also very thankful to my family and friends for their unconditional support and encouragement throughout this period.

Finally, this thesis marks the end of my time at TU Delft. Looking back, I am grateful for the experiences, knowledge, and opportunities that this university has provided me over the past years.

Delft, University of Technology H. Gielen
January 8, 2026

Chapter 1

Introduction

1-1 Motivation

In 2015, the Paris Climate Agreement set the goal of keeping global warming below 1.5 $^{\circ}C$ above the pre-industrial average by 2050. However, recent observations show that the global mean temperature surpassed this limit in 2024, making it an all-time record at the time [1]. To mitigate further temperature increase, renewable energy needs a substantial increase [2].

In 2024, wind energy accounted for 19% of the electricity consumed across the EU, with the total installed wind power capacity reaching 231 GW [3]. Figure 1-1 illustrates the expected growth in annual wind power installations in the EU over the period 2025 to 2030, compared to previous years. To reach the EU's renewable energy target of 42.5% by 2030, wind energy installations must average 36 GW a year between 2025 and 2030, based on a wind power capacity target of 425 GW [3]. As can be seen in Figure 1-1, this is well above the expected wind power installation.

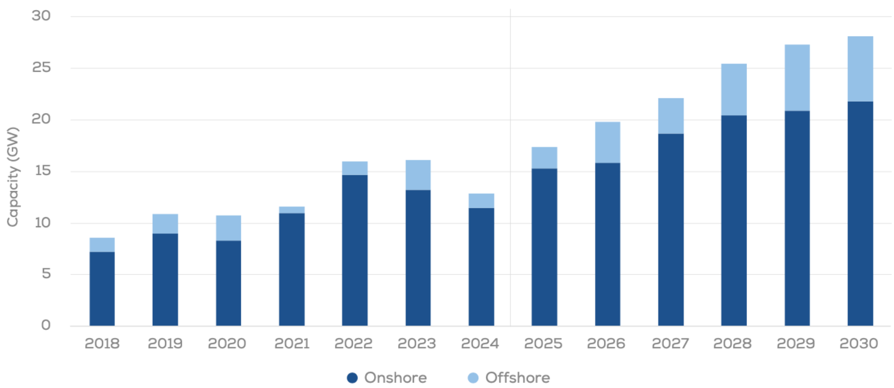

Figure 1-1: Expected annual wind power installations in the EU over 2025-2030 [3].

An important aspect of reaching these goals is ensuring that wind turbines and wind farms operate to their full capacity. This can be improved by minimizing turbine downtime caused by maintenance or flaws and by optimizing operational performance. Improved operation of the wind farm can reduce wake losses, this is caused by upstream wind turbines that extract kinetic energy from the wind, reducing wind speed and increasing turbulence for downstream turbines. These downstream turbines operate in reduced or disturbed wind flow, resulting in less available energy to generate power from and increased structural loads [4]. To illustrate, in Figure 1-2, the wakes became visible due to fog in specific weather conditions. Operation in wake conditions increases wear and reduces the lifetime of components, which can therefore attribute to the downtime of the wind turbine. Wind Farm Flow Control (WFFC) addresses these challenges to achieve a farm-wide goal, such as maximizing Annual Energy Production (AEP) or minimizing loads [4].

The primary goal of WFFC is to reduce the overall cost of wind energy, which can be achieved by addressing a number of technical objectives. Most of the existing research focuses primarily on increasing the power output of the wind farm [5], [6], [7]. However, the effects of this collective power maximization on structural loads remain unclear [8]. Accurate fatigue load prediction usually requires costly aero-servo-elastic simulations [9]. To overcome this problem, new approaches introduce load surrogate models, which use simplified inputs to estimate loads on the turbine components in a faster and more scalable way, as is done in [10]. For future wind farm control applications, it becomes more important to address not only power optimization but also other aspects, such as structural loads.

Figure 1-2: Specific weather conditions with fog allow the wakes formed in an off-shore wind farm to become visible [11].

1-2 Background Information

1-2-1 Wind Farm Flow Control Strategies

WFFC takes a farm-level perspective aimed at reducing wake losses and improving overall efficiency. This is achieved by going from a **greedy control**, where each turbine aims to optimize its own power production, to a collaborative approach. Three widely studied strategies are **wake steering**, **axial-induction control**, and **wake mixing control**.

The first strategy, **wake steering** or **wake redirection** control, is illustrated in Figure 1-3. In this strategy, an upstream turbine is intentionally given a yaw offset or yaw misalignment angle, which deflects its wake away from downstream turbines. By shifting from a full wake overlap, where the entire rotor plane is covered by the wake, to a partial overlap, in which only part of the rotor plane is affected, as visualized in Figure 1-3, the downstream turbine experiences a higher overall incoming wind speed and thus more available kinetic energy to generate power. In addition to power gains, wake steering can also reduce fatigue loading: turbines operating in wake conditions experience elevated turbulence intensities, which increases fatigue loads [12]. Redirecting wakes can therefore benefit both the fatigue life and power production of downstream turbines. However, partial wake conditions can also result in an asymmetric loading, which could increase fatigue loads despite the increase in power output.

The second control strategy is **axial induction control**, which increases downstream power production by de-rating upstream wind turbines [13]. Figure 1-4 illustrates this approach. The axial induction factor a describes the relationship between the free-stream wind speed and the reduced wind speed at the rotor plane and can be lowered through adjustments of the blade pitch angle [14], [15] or generator torque [16]. Reducing a at the upstream turbine decreases its power output and the thrust force it exerts on the flow, resulting in a higher wind speed in the wake. This preserves more kinetic energy in the wake, increasing the potential of power generation for the downstream turbine.

The third control strategy is **wake mixing control**. In contrast to wake steering, which aims to redirect the wake, wake mixing focuses on accelerating wake dissipation by enhancing mixing with the surrounding flow, thereby increasing wind speeds at downstream turbines. Wake mixing can be achieved through active blade pitch modulation, and two approaches are commonly used [17]. **Pulse wake mixing** applies periodic collective pitch variations to induce axial thrust oscillations. **Helix wake mixing** uses individual blade pitch variations to generate time-varying yaw and tilt moments, resulting in a helicoidal wake structure [14]. Both strategies aim to enhance wake recovery and are illustrated in Figure 1-5.

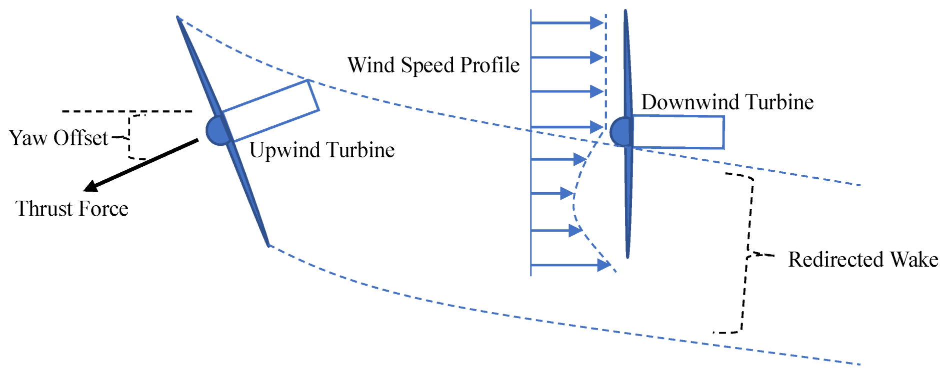

Figure 1-3: Wake steering: the upstream turbine is intentionally given a yaw offset to redirect its wake away from the downstream turbine. This increases the overall incoming wind speed for the downstream turbine and thereby its power production [18].

1-2-2 Control Algorithms

Control strategies are most commonly applied in open-loop, depending on steady-state wind farm engineering models, where current flow conditions are used to look up precomputed steady-state control solutions [20]. For each ambient condition, optimal yaw angle set points are determined in

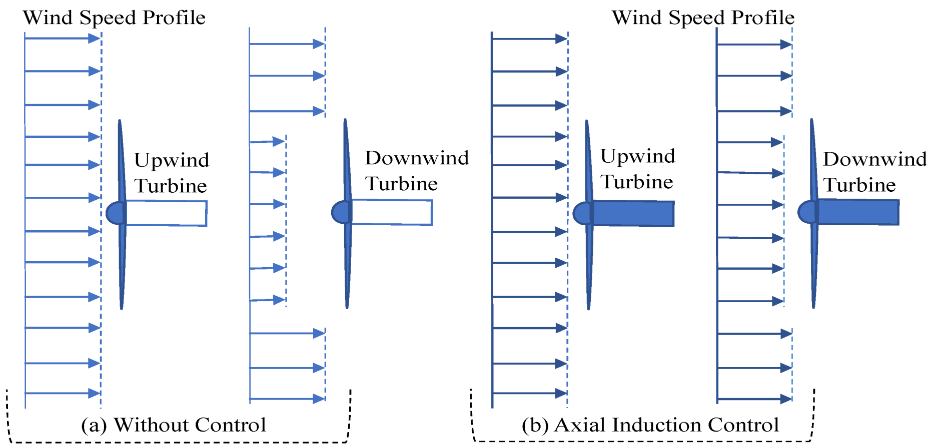

Figure 1-4: Axial induction control: (a) without control, the upstream turbine extracts significant kinetic energy from the flow, leading to a large velocity deficit in its wake; (b) when the upstream turbine is de-rated, it exerts a lower thrust force on the wind, producing less velocity deficit and increasing the power production potential of the downstream turbine [18].

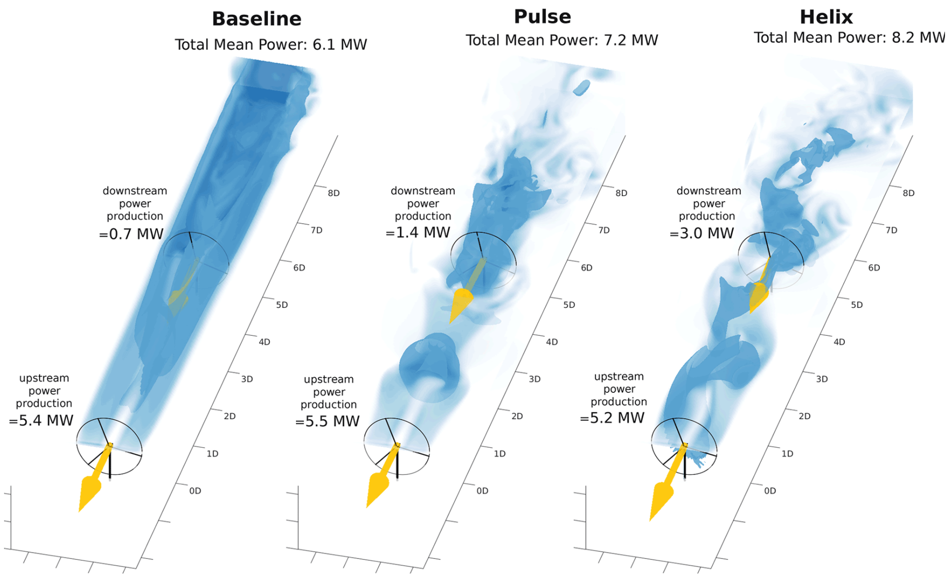

Figure 1-5: Wake mixing control: comparison of the baseline case (left), Pulse wake mixing (middle), and Helix wake mixing (right) for a two-turbine configuration under full wake overlap. Both strategies promote wake mixing, accelerating wake recovery and increasing downstream wind speeds [19].

advance and stored in a Look-up Table (LuT) [4]. A limitation of this approach is its inability to react to unexpected changes in the environment or turbine behavior.

In contrast, closed-loop control takes real-time measurements from the wind farm to continuously optimize their control set points online. This makes the strategy more flexible and resilient [21]. Figure 1-6 shows a simple representation of the fundamental difference between closed-loop and open-loop control.

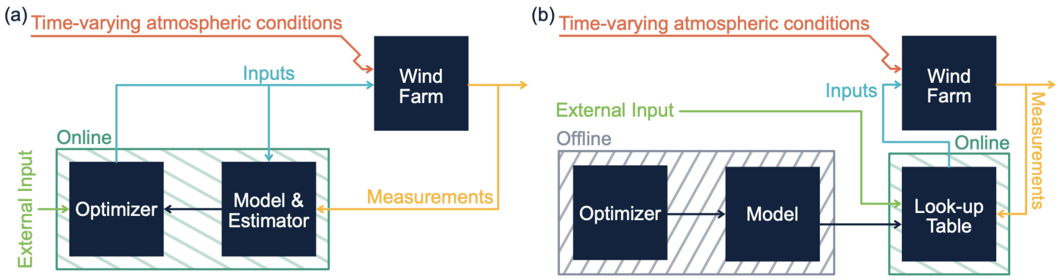

Figure 1-6: Overview of two distinct wind farm control strategies: (a) online closed-loop control, and (b) open-loop control based on the LuT approach [21]. The external input corresponds to the ambient inflow conditions, such as wind direction, turbulence intensity, and wind speed.

Another important distinction in control strategies is whether the controller relies on a surrogate model, a simplified mathematical representation based on the physics of the wind farm [21]. Such model-based controllers depend on accurate models to predict system behavior and optimize control actions. The next section will go into these wind farm models in more detail.

Alternatively, control can be done through data-driven approaches, where the system is controlled without knowing the underlying physics or having an explicit model. Instead, the controller learns the behavior of the system directly from input and output data using machine learning techniques, such as neural networks or reinforcement learning [22], [23]. Although model-free control can overcome some of the weaknesses of surrogate-based approaches, such as the sensitivity to model miscalibrations and under-represented dynamics, it also remains challenging. In particular, wind farms are slow systems with a wide range of states, such as varying wind directions and speeds, and are subject to high disturbance and turbulence. As a result, collecting enough training data for reliable control can be very time consuming. For these reasons, model-free control is outside the scope of this thesis.

1-2-3 Wind Farm Flow Models

For wind farm control, real-world data sources such as Supervisory Control and Data Acquistion (SCADA) and Light Detection and Ranging (LiDAR) technologies are used to monitor input and output data. SCADA is a real-time monitoring system and collects data on turbine level such as power output, rotor speed, blade pitch angle and yaw alignment. LiDAR is a remote sensing technology that uses lasers to measure wind speed and direction ahead of the turbine and is able to capture the incoming wind field. Besides using real-world data, wind tunnel experiments can be used [24]. These setups allow investigating wake behavior, turbine interaction, and control strategies in a reproducible environment.

However, to make the control more accessible and suitable for model-based control a model surrogate or simulation is most commonly used. These approximate the behavior of wind turbines and their interactions through mathematical models of varying complexity. Wind farm simulation models can be classified according to their level of fidelity, which gives a balance between physical accuracy and computational efficiency [4].

Low-fidelity Models

Low-fidelity models, such as FLOw Redirection and Induction in Steady-state (FLORIS) [25], Frandsen [26], PyWake [27] and FOXES [28], rely on static wake solvers. These models solve simplified parametric equations to approximate wake effects and wind turbine interactions, examples are the Jensen model [29], which assumes a simple top-hat profile, the Gaussian wake model, by Bastankhah *et al.* [30], or the double-Gaussian model by Ishihara and Qian [31]. Low-fidelity models use steady-state assumptions to estimate wake behavior, such as velocity deficit and wake deflection, based on a reduced set of inputs. Although these models lack the ability to capture dynamic flow phenomena, their speed and simplicity make them more suitable for tasks that require a large number of simulations, such as optimizing the wind farm layout and estimation of the AEP.

High-fidelity Models

To accurately capture the full flow behavior of a wake, the three-dimensional unsteady Navier-Stokes equations must be solved. However, without making significant assumptions, it is not possible to solve these equations [13]. Instead, Computational Fluid Dynamics (CFD) methods use numerical analysis and algorithms to solve the Navier-Stokes equations. Large Eddy Simulation (LES) was developed to resolve these partial differential equations by simulating the large turbulent motions and approximating the smaller ones with simplified models [32]. Most high-fidelity models rely on LES to provide the most detailed and accurate description of the complex aerodynamic interactions within a wind farm. While this makes them particularly suitable for validation studies and understanding flow physics, their high computational cost makes them too demanding for model based control. An example of a commonly used open-source tool based on LES developed by the National Renewable Energy Laboratory (NREL) is Simulator for Offshore Wind Farm Applications (SOWFA) [33]. Other examples are UTD Wind Farm (UTDWF) developed at UT Dallas [34], and SP-wind by Meyers and Meneveau [35].

Medium-fidelity Models

To bridge the gap between low- and high-fidelity approaches, medium-fidelity models have been developed. These models aim to capture the critical dynamics and accuracy of high-fidelity formulations while preserving the simplifications and computational efficiency of low-fidelity models. By doing so, they enable the use of closed-loop control methods and account for model uncertainties [36]. These medium-fidelity models include simplified representations of the flow and turbines, without solving the full turbulence structure. Medium-fidelity models cover a wide spectrum. At the lower end of the fidelity range, quasi-dynamic wind farm simulators, such as FLOw Redirection and Induction Dynamics (FLORIDyn) [37] and PossPow [38] use low-fidelity rotors and wake profiles in a time-stepping simulation [39]. These models can either implement their own wake representations or be coupled with existing simplified steady-state wake models, such as PyWake or FLORIS. This makes them suitable for real-time feedback control and other possible wind farm operations [4].

Closer to high-fidelity models are more computationally demanding models that consider a two-dimensional space to approximate the Navier-Stokes equations [13]. Examples include models based on the 2-D Ainslie [40] and 2-D dynamic wake meandering (DWM) [41] model, such as WFSim [36] and HAWC2Farm. The last model combines a DWM model with HAWC2, an aeroelastic wind turbine simulator. This allows them to capture the essential load dynamics across turbines while maintaining manageable computational cost [39]. Simulations from such aeroelastic wind farm simulators, such as FAST.Farm [42], can provide data for training or calibrating of data-informed surrogate models. They are also used for validation of optimized control settings for power or structural loads, especially when higher-fidelity LES simulations would require higher computational cost [43].

Table A-1 in Appendix A summarizes the main properties of wind farm models based on their fidelity. This table was constructed and discussed during the literature review conducted prior to this thesis [44].

1-3 Problem Statement and Gaps

WFFC aims to reduce the overall cost of wind energy. In addition to increasing power production, extending turbine lifetime and lowering maintenance costs also contribute to this objective. Wake steering is a control strategy with the potential to do both. By intentionally applying a yaw misalignment angle at upstream turbines, the wake can be redirected from downstream turbines, increasing their power production potential. Since wakes significantly increase turbulence intensity (TI) and thereby fatigue loads, redirecting the wake can also reduce structural loading. However, this must be applied carefully, as partial wake overlap can result in asymmetric loading and potentially increase fatigue.

Existing wind farm models range from low-fidelity to high-fidelity. Low-fidelity wake models are widely used for layout and AEP optimization, but they are too simplified for accurate load predictions. Higher-fidelity aeroelastic wind farm simulators are able to capture load dynamics, but their high computational cost makes them unsuitable for model-based control. A promising solution is to use data from aeroelastic wind farm simulators to train load surrogate models [9]. These surrogate models map simple inflow quantities to load predictions, allowing load estimations within lower-fidelity control-oriented models.

The shift from steady-state, low-fidelity models to medium-fidelity models capable of capturing more dynamic behavior is an actively researched area. These dynamic models maintain computational efficiency while providing a more realistic description of wind farm dynamics and enabling more advanced control that accounts for model uncertainties and unforeseen circumstances. Steady-state models assume that changes in operating conditions of an upstream turbine immediately affect the downstream turbine. In reality, there is a delay, as the wake needs time to propagate downstream. Recent studies have shown that dynamic wake descriptions result in improved performance, such as better correlation and lower normalized root-mean-squared-error (RMSE) when comparing the simulated and measured power signals [4]. These findings highlight the need for dynamic modeling in control-oriented applications, particularly under more realistic changing inflow and operating conditions.

Identified Research Gaps

Most wake steering studies still rely on steady-state models, even though dynamic wake propagation has been shown to be important for more realistic predictions. Moreover, load surrogate models have been presented and validated very promisingly, with the advantage that they can be transferred across frameworks as long as the required inputs can be extracted. However, limited work has investigated their performance across different wake models and particularly within dynamic wind farm simulations. Consequently, it remains unclear what the potential of a load surrogate model is in a dynamic simulation and how time-varying flow dynamics affect surrogate accuracy and controller performance.

1-4 Thesis Objective

Based on the problem statement and gaps identified in the literature, the following research objective was formulated.

Research Objective

"The objective of this thesis is to develop and evaluate a power-load balanced wake steering control strategy that couples a dynamic flow model with a load surrogate model, aiming to achieve both power gain and load reduction."

This objective requires three main components:

1. a dynamic wind farm flow model,
2. a load surrogate model, and
3. a controller.

In the literature research prior to this thesis [44], several load surrogate models and dynamic wind farm flow models were investigated. They were evaluated based on how well the required inflow inputs of the surrogate model and the wind farm framework align. The dynamic models were further assessed with a focus on their control-oriented performance and potential. Based on this evaluation, the dynamic framework OFF by Becker *et al.* [45] was selected as the most suitable choice for this thesis, together with the sector-averaged load surrogate model by Guilloré *et al.* [8]. In this thesis, these components are combined, together with a controller that includes the predicted fatigue loads.

To achieve the objective, the thesis is structured around two main research questions. These research questions are divided into sub-questions to allow for a systematic approach in answering the main questions.

Research Question 1

"What is the role and performance of a load surrogate model when applied within a dynamic wind farm flow modeling framework?"

1.1 How does the load surrogate model perform when coupled with OFF?

1.2 How do modeling inconsistencies between OFF and the surrogate training framework affect load prediction accuracy?

1.3 To what extent can the prediction accuracy of the load surrogate model be improved, and what limitations constrain further reductions in the root mean squared percentage error (RMSPE)?

1.4 How does the choice of sampling time affect the trade-off between computational cost and relative damage accuracy?

Research Question 2

"What power-load trade-offs arise when fatigue loads are included in a wake steering control strategy under dynamic flow conditions?"

2.1 How does the inclusion of fatigue loads in the control objective affect optimal yaw misalignment behavior?

2.2 What is the trade-off between power gain and fatigue damage for different power-load weightings?

2.3 How does a power-load balanced wake steering controller perform compared to a baseline and power-only strategy in a three-turbine case study?

2.4 How do dynamic wake effects influence predicted power and load responses compared to steady-state predictions?

1-5 Contribution and Outline

Contributions

The main contributions of this thesis are the following:

C.1 Extension of the dynamic wind farm flow model OFF with the sector-averaged load surrogate model to predict damage equivalent loads (DELs) on individual turbines within a wind farm.

C.2 Development of a LuT-based wake steering control strategy that balances power maximization and tower base fatigue load minimization using weighting factors.

C.3 Evaluation of the proposed controllers in a three-turbine case study using three 40-minutes wind direction signals.

C.4 Analysis of how tower base load reduction is achieved by the controller and where the trade-off between power gain and load reduction occurs.

C.5 Comparison between steady-state and dynamic model behavior to explain observed differences in predicted power gains and load reductions.

Outline and Roadmap

This thesis is structured as follows, providing a roadmap for addressing the main research questions and their sub-questions. First, Chapter 2 introduces the OFF framework, which combines the steady-state FLORIS model [25] with the dynamic wake advection principles of FLORIDyn [37].

Chapter 3 addresses Research Question 1 and describes the integration of the load surrogate model within OFF. Section 3-1 presents the sector-averaged load surrogate model by Guilloré *et al.* [8], including its required inputs. Section 3-2 explains how the required inputs are extracted from OFF, evaluates the accuracy of the predicted DELs, identifies the limitations, and outlines the steps taken to improve prediction accuracy. Moreover, it investigates how the choice of sampling time influences the trade-off between computational cost and relative damage accuracy.

Chapter 4 introduces the control strategy developed in this thesis and addresses Sub-questions 2.1 and 2.2. Section 4-1 describes the dead-band LuT-based yaw controller implemented in OFF, while Section 4-2 presents the formulation of a power-load balanced objective function and motivates the inclusion of tower base fatigue loads. The chapter also discusses the resulting optimal yaw misalignment behavior, which is explained through the observed trends in tower-base loading.

Chapter 5 applies and evaluates the developed control strategy in a three-turbine case study. Section 5-1 presents the simulation setup, including the wind direction time series and the selected controller parameters in OFF. Section 5-2 presents the predicted power gains and load reductions for several power-load weightings and motivates the selection of an optimal weighting for further analysis of the *balanced controller*. Section 5-3 discusses the resulting power-load trade-offs by comparing the *balanced controller* with the *power-only* and *baseline* strategies. Section 5-5 examines how dynamic wake behavior considered in OFF influences power and load predictions compared to the steady-state assumptions present in FLORIS. Through these analyses, Chapter 5 addresses Research Question 2.

Finally, Chapter 6 summarizes the main findings of the thesis and discusses its limitations, along with recommendations for future work.

Chapter 2

Dynamic Wind Farm Model OFF

This chapter introduces the dynamic wake modeling framework OFF, developed by Becker *et al.* [4]. OFF is an open-source, unified toolbox that allows evaluation and comparison between different control approaches. It interfaces with established steady-state models such as FLORIS [25] or PyWake [27], and supports the development and testing of control-oriented dynamic Wind Farm Flow Control (WFFC) strategies at low computational cost.

2-1 The OFF Framework

The framework OFF [4], an abbreviation based on OnWARDS [46], FLORIDyn and FLORIS, combines dynamic flow representations with steady-state wake evaluations. Its structure, illustrated in Figure 2-1, follows the FLORIDyn principles to model state dynamics such as wake advection, and employs FLORIS as the underlying steady-state wake model.

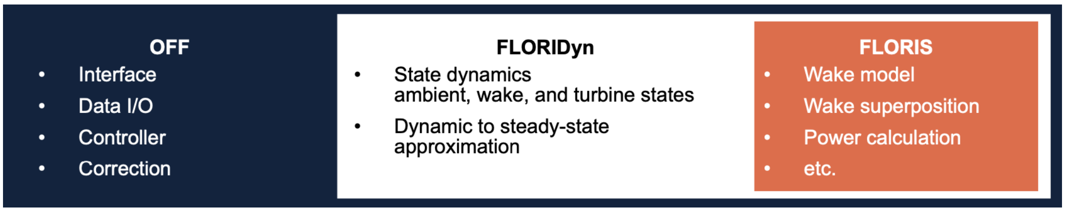

Figure 2-1: Overview of the OFF framework used in this thesis. OFF provides the interface between the wake solvers and the controller. FLORIDyn models the dynamic evolution of the flow, while FLORIS provides steady-state wake evaluations at the turbine locations [4].

Within OFF, the instantaneous flow field of the wind farm is evaluated by the underlying steady-state wake model FLORIS, while the evolution of the wake dynamics is modeled using the FLORIDyn principles. The following sections describe both components and their integration within OFF.

2-2 Underlying Models

2-2-1 Steady-state Model: FLORIS

A wake model in FLORIS is made up of four components that together constitute a wake. In this thesis, the Gaussian wake formulation following Bastankhah and Porté-agel [30] and Niayifar and Porté-agel [47] is used. The underlying models are: the Jimenez deflection model [48], the Crespo-Hernandez turbulence model [49], the Gaussian velocity deficit model [50] and, finally, the Sum of Squares Freestream Superposition (SOSFS) method is used for combining wakes to capture the coupled effects.

Velocity Deficit

The Gaussian model represents the velocity deficit as a Gaussian distribution in the spanwise direction. The wake region is divided into a near-wake zone and a far-wake zone, with the transition occurring after approximately two rotor diameters downstream of the turbine [47].

Before the introduction of the Gaussian model, simpler top-hat models, such as the Jensen model [29], were commonly used. These models assume a uniform velocity deficit across the wake, typically underestimating the deficit near the wake center and overestimating it near the edge of the wake [50]. Figure 2-2 illustrates the difference between the traditional top-hat and Gaussian profiles.

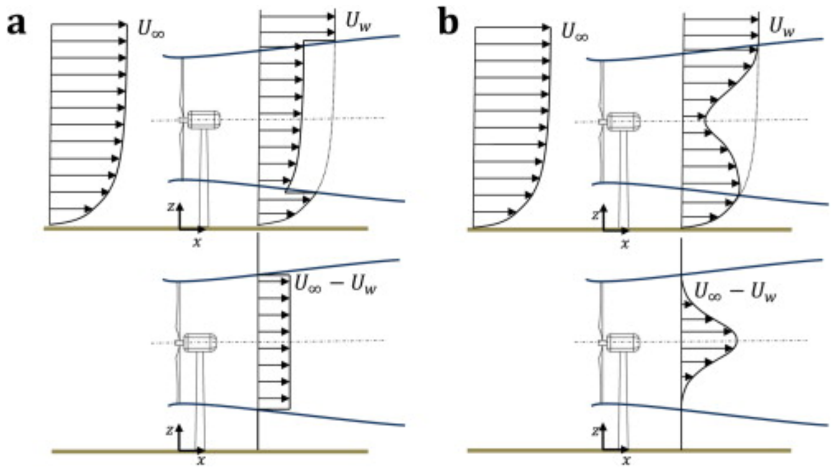

Figure 2-2: Velocity and velocity deficit profiles of a wind turbine assuming a top-hat (a) and Gaussian (b) distribution [50]. U_∞ represents the incoming wind velocity and U_W the wake velocity in the streamwise direction.

Several studies have shown that the normalized velocity deficit in turbine wakes follows a self-similar Gaussian distribution [50, 47]. As a result, the Gaussian model improves accuracy of wake predictions in both full- and partial-wake conditions.

An analytical expression for the velocity deficit behind a turbine in the far wake can be derived from the simplified Navier–Stokes equations. It is formulated by Bastankhah and Porté-Agel [50] as:

$$\frac{\Delta U}{U_\infty} = \left(1 - \sqrt{1 - \frac{C_T}{8\left(k^* \frac{x}{d_0} + \varepsilon\right)^2}}\right) \times \exp\left[-\frac{1}{2\left(k^* \frac{x}{d_0} + \varepsilon\right)^2}\left\{\left(\frac{z - z_h}{d_0}\right)^2 + \left(\frac{y}{d_0}\right)^2\right\}\right], \quad (2\text{-}1)$$

where $\Delta U = U_\infty - U_W$, k^* denotes the wake growth rate, x, y, z are the streamwise, spanwise, and vertical coordinates, z_h is the hub height, d_0 the rotor diameter, and ε a correction term depending on the thrust coefficient C_T.

The total thrust force and generated power are defined as:

$$T = \frac{1}{2} C_T \rho A_0 U_\infty^2, \qquad P = \frac{1}{2} \rho A U_W^3 C_P, \tag{2-2}$$

where ρ is the air density, A_0 the rotor area, U_W the streamwise wind speed, and C_P the power coefficient, which represent the turbine's efficiency in extracting energy from the wind.

The thrust and power coefficient follow the *cosine-loss* model, which describes the reduction in thrust and power as the turbine yaws away from the incoming wind direction.

$$C_T \approx 4a(1-a)cos\gamma, \qquad C_P \approx 4a(1-a)^2(cos\gamma)^{P_p}, \tag{2-3}$$

where a is the axial induction factor, describing how strongly the flow is decelerated by the turbine, and P_p is the cosine loss exponent, determining the power loss due to yaw misalignment.

In FLORIS, to run a model requires providing the turbine's C_T and C_P curves as functions of wind speed. The C_T and C_P curves are derived from turbine operational curves obtained through higher fidelity simulations or experimental measurements.

Turbulence Intensity
Turbine wakes increase the local turbulence intensity (TI), compared to the ambient TI. In FLORIS, the TI is modeled following the Crespo-Hernandez formulation [49]:

$$I = \sqrt{\sum_{j=0}^{N} (I_j^+)^2 + I_0^2}, \tag{2-4}$$

where I_0 is the ambient TI, and I_j^+ the added TI from upstream turbine j.

In practice, FLORIS uses the maximum contribution:

$$I = \max_j \sqrt{(I_j^+)^2 + I_0^2}, \tag{2-5}$$

based on the findings of Niayifar and Porté-Agel [50], who found that the local TI is dominated by the nearest upstream turbine. This assumption avoids overestimating the TI in overlapping wakes.

Each I_j^+ term depends on the turbine's induction factor a_j, the ambient TI I_0, and the normalized downstream distance (x/d_0):

$$I_j^+ = A_{\text{overlap}} \left(0.5 a_j^{0.8} I_0^{0.1} \left(\frac{x}{d_0} \right)^{-0.32} \right), \tag{2-6}$$

where $A_{overlap}$ represents the downstream rotor area influenced by the wake of turbine j. In the Gaussian wake model used in FLORIS, the added turbulence considers all turbines within a distance of 15 rotor diameters upstream and 2 in spanwise direction.

Wake Deflection

The wake models in FLORIS include wake deflection models that approximate the lateral displacement of the wake resulting from yaw misalignment of the turbine. Two wake deflection models are defined, of which the Jiménez model [48] is used.

The angle at the wake centerline is defined as:

$$\xi(x) \approx \frac{\xi_{\text{init}}^2}{1 + 2k_d \frac{x}{d_0}}, \tag{2-7}$$

$$\xi_{\text{init}}(a, \gamma) = \frac{1}{2} \cos^2 \gamma \sin \gamma C_T, \tag{2-8}$$

where ξ_{init} is the initial skew angle from the wake centerline and k_d is a tunable deflection parameter.

The total lateral displacement $\delta(x)$ of the wake centerline is obtained by integrating the deflection angle along the streamwise direction and is approximated by applying a second-order Taylor series approximation as demonstrated in [51]:

$$\delta(x) = \int_0^x \tan \xi(x)\, dx \tag{2-9}$$

$$\delta(x) \approx \frac{\xi_{\text{init}} \left[15 \left(\frac{2k_d x}{d_0} + 1 \right)^4 + \xi_{\text{init}}^2 \right]}{\frac{30k_d}{d_0} \left(\frac{2k_d x}{d_0} + 1 \right)^5} - \frac{\xi_{\text{init}} d_0 \left(15 + \xi_{\text{init}}^2 \right)}{30k_d}. \tag{2-10}$$

Wake Combination

Individual wake velocity deficits are combined using the SOSFS method proposed by Katíc *et al.* [52]. In this approach, the combined velocity is obtained using a sum of squares of the individual velocities:

$$\left(1 - \frac{U}{U_\infty}\right)^2 = \left(1 - \frac{U_1}{U_\infty}\right)^2 + \left(1 - \frac{U_2}{U_\infty}\right)^2, \tag{2-11}$$

where U_∞ is the free-stream velocity and U_1 and U_2 are the wake velocities from the individual turbines.

The models described above are modular in FLORIS. In [53], Annoni *et al.* provide an analysis of the various model options available in FLORIS. The specific model settings used in this thesis are those described here.

2-2-2 Dynamic Model: FLORIDyn

The dynamic component of OFF is based on the simplified wake dynamics implemented in FLORIDyn [37]. Instead of assuming steady-state conditions, it models the advection of wake states over time using Observation Points (OPs) that propagate downstream.

Each OP follows the wake centerline, representing the core of the wake, where the wind speed deficit and turbulence effects are the largest. New OPs are created at every time step and carry states from the rotor plane downstream with the free-stream wind speed along the main wind direction. Each OP maintains the following information:

- Turbine states x_T (such as the yaw angle or axial induction)
- Flow field states x_{WF} (such as the wind speed, direction and ambient turbulence intensity)
- Its own positional states x_{OP}

The FLORIDyn framework uses two separate coordinate systems, K_1 presents the wake coordinate system and K_0 presents the world coordinate system as illustrated in Figure 2-3. The downwind step is calculated in the wake coordinate system K_1 and translated to the world coordinate system K_0 using the rotation matrix $\mathbf{R_{01}}$, as expressed in [37]:

$$x_{OP,0}(k+1) = x_{OP,0}(k) + \mathbf{R}_{01}(x_{WF,\phi})[x_{OP,1}(k+1) - x_{OP,1}(k)], \tag{2-12}$$

where $x_{OP} = [x_{OP,0}, x_{OP,1}]^T$ denotes the positional state of the OP, with $x_{OP,0}$ in the world coordinate system and $x_{OP,1}$ in the wake coordinate system. $x_{WF,\phi}$ refers to the wind field state in the wind direction ϕ.

The update of the *positional states* x_{OP} in the wake coordinate is calculated with the following equation:

$$x_{OP,1,x}(k+1) = x_{OP,1,x}(k) + \Delta t x_{WF,u}, \tag{2-13}$$

$$x_{OP,1,y,z}(k+1) = \delta(x_{OP,1,x(k+1),x_T,x_{WF}}), \tag{2-14}$$

where Δt is the simulation time step, $x_{WF,u}$ the free-stream wind speed. The lateral and vertical locations are described by the deflection function δ, which results from the turbine's yaw misalignment and rotor tilt angle.

The definitions of *turbine states* x_T and *wind field states* x_{WF} depend on the underlying parametric wake description. The turbine state x_T includes all turbine-specific states that are required to calculate the wake shape. The wind field states x_{WF} include all states necessary for the propagation and calculation of the wake.

2-2-3 Integration within OFF

In OFF, the states are updated through three consecutive steps: prediction (Equation 2-15), correction (Equation 2-16) and control (Equation 2-17).

$$[\mathbf{x}_T(k), \mathbf{x}_{\text{amb}}(k), \mathbf{x}_{\text{OP}}(k)] = f_{\text{prediction}}(\mathbf{x}_T(k-1), \mathbf{x}_{\text{amb}}(k-1), \mathbf{x}_{\text{OP}}(k-1), \mathbf{c}), \tag{2-15}$$

$$[\mathbf{x}_T(k), \mathbf{x}_{\text{amb}}(k), \mathbf{x}_{\text{OP}}(k)] = f_{\text{correction}}(\mathbf{x}_T(k), \mathbf{x}_{\text{amb}}(k), \mathbf{x}_{\text{OP}}(k), \mathbf{m}(k), \mathbf{c}), \tag{2-16}$$

$$\mathbf{x}_T(k) = f_{\text{control}}(\mathbf{x}_T(k), \mathbf{x}_{\text{amb}}(k), \mathbf{x}_{\text{OP}}(k), \mathbf{m}(k), \mathbf{c}), \tag{2-17}$$

where $\mathbf{c}$ represents a set of parameters, k the time step, and $\mathbf{m}$ a set of measurements.

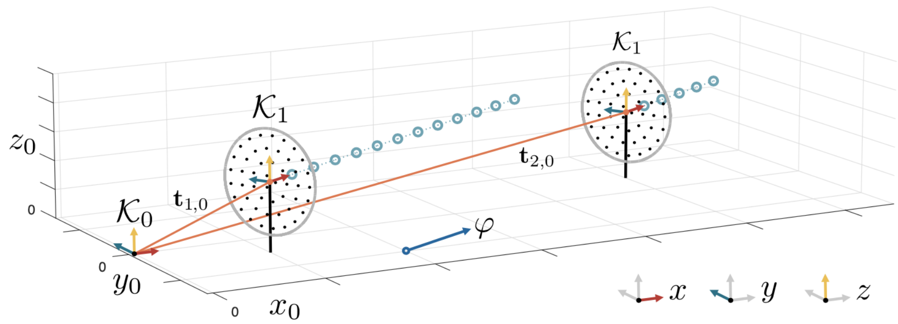

Figure 2-3: Visualization of the coordinate systems K_1 and K_0 and the propagation of the OPs downstream, following the centerline [37].

- The **prediction step** advances the model state by only using information from the previous time step, propagating the system forward based on its internal dynamics.
- The **correction step** integrates current measurements to refine the predicted states.
- Finally, the **control step** computes the control actions the turbine takes based on the current state and measurements.

OFF uses the concept of a Temporary Wind Farm (TWF) to approximate local ambient and wake conditions at a given turbine location. The TWF maps the current dynamic state to the steady-state wake model FLORIS for evaluation. These TWFs represent the static wake behavior within a heterogeneous flow field and allow the dynamic framework to operate independently of the underlying steady-state wake model, FLORIS.

Figure 2-4 illustrates this process for a three-turbine example. Turbines T1 and T2 operate in free-stream conditions, while T3 is subject to their wakes. T1 and T2 receive wind field input, add their own states, and generate the first OP, which adds its own states and propagates downstream. For each impacting wake, one OP is interpolated from the two closest OPs in that wake, minimizing the distance to T3. This interpolation process is illustrated in more detail in Figure 2-5. Its state is a distance-based interpolation of the two parent OPs. The resulting OPs approximate the environment of T3.

The resulting TWF is then passed on to FLORIS for evaluation. This returns predicted measurements such as the effective wind speed, TI, and the generated power.

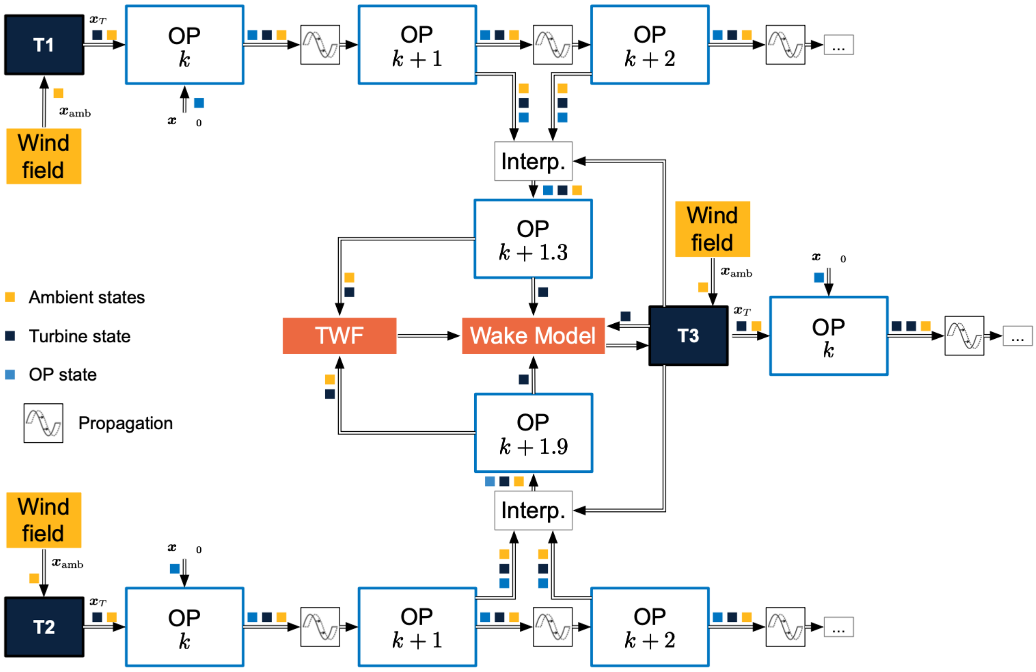

Figure 2-4: Turbines T1 and T2 operate in free-stream conditions and generate OPs that propagate downstream. For the downstream turbine T3, the inflow conditions are reconstructed by interpolating the two closest OPs per impacting wake, providing an approximation of the local flow environment at T3. The resulting TWF is passed to FLORIS for evaluation, yielding predicted measurements such as the effective wind speed, TI, and power output [4].

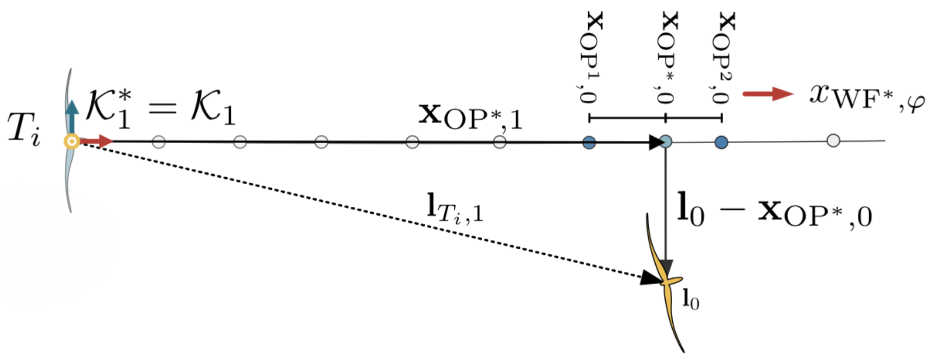

Figure 2-5: Interpolation of the two closest OPs to calculate OP^* and the position of l_0 [37].

Chapter 3

Load Surrogate Integration

This chapter presents the integration of a load surrogate model into the OFF framework and outlines the main contributions:

- Implementation of the sector-averaged load surrogate model in OFF, including a clear procedure to extract the required inputs.
- Identification of the challenges in transferring surrogate models between wind farm frameworks, caused by inconsistencies in wake modeling and turbulence definitions.
- Recommendation of a methodological approach to improve the accuracy of surrogate load predictions across modeling frameworks.
- Demonstration of how the choice of DEL sampling time affects the trade-off between capturing load fluctuations and maintaining computational efficiency in dynamic simulations.

This chapter thereby addresses Research Question 1 and all associated sub-questions.

Section 3-1 introduces the sector-averaged load surrogate model proposed by Guillore *et al.* [8]. Section 3-2 provides a step by step description of the model's implementation within the OFF framework, evaluates its performance on a three-turbine test case, and describes its application in dynamic simulations. Finally, Section 3-3 provides a summary of the main findings of this chapter.

3-1 Sector-Averaged Load Surrogate Model

Estimating structural loads in wind farms relies on computationally demanding aero-servo-elastic simulations, making them less suitable for optimization and control. This motivated the development of control-oriented load surrogate models that can approximate structural fatigue loads under varying operating conditions without the need for full-scale simulations [9].

Load surrogate methods can differ in the required inputs, the chosen functional mapping methods and the creation of high-fidelity training data [9]. Basic models often use mean wind speed and turbulence intensity to estimate fatigue loads, as is done in [54]. However, predicting loads caused by complicated spatial variations from one or more partial wakes remains challenging. To overcome this, the lateral and vertical shear are considered in [55]. Other approaches use properties of the wind farm itself, including turbine spacing, wind incident angles, and number of upstream turbines influencing a given rotor, as inputs to the surrogate model [56]. A practical method for load modeling is based on gridding, where simulations are performed for a wide range of possible conditions. These simulations are used to construct a LuT with the fatigue and extreme loads on all components of interest [57].

In this thesis, the focus is on the sector-averaged load surrogate model, developed by Guilloré at the Technical University of München (TUM) [8], which is based on sector-averaged mean wind speeds and turbulence intensities across the rotor plane. The model is used to estimate the damage equivalent loads (DELs) of a wind turbine under various control actions. These represent a single, constant-amplitude fatigue load that would produce equivalent damage over a limited time period [58].

The focus is on this model because it represents a state-of-the-art, control-oriented approach that includes wake steering applications. By dividing the rotor plane into multiple sectors, it can capture both full and partial wake overlap. It predicts the DELs using only simple, local inflow quantities and the operational state of the wind turbine. This simple input structure makes the model very suitable for integration into simplified wake models. Despite its simplified representation of the complex flow interactions and controller dynamics, the model has been shown to accurately characterize the DELs. These properties make the model particularly suitable for load-aware wind farm control and optimization strategies.

This section will go into the details of this model. The three main choices that are necessary to build a load surrogate model are the following.

1. Choice of dataset source
2. Choice of inputs to the surrogate
3. Choice of surrogate function

In addition to these, decisions must be made about the number of input cases, the number of turbulent seeds, the ambient conditions, and which wind farm control actions are included. A general approach to developing a load surrogate model is illustrated in Figure 3-1.

The model is location-agnostic, this means that the surrogate model can be used for all wind turbines in the farm, regardless of their position. Although the surrogate can be applied to any new wind farm set up, it can only be applied to the same wind turbines that match the type used during training of the surrogate, IEA 3.4MW [59] or IEA 22MW [60] in this case. Moreover, there is a limit to the inflows, the model cannot be used for wind speeds and turbulence intensities (TIs) that fall outside the training range of the model. The TUM model is control-oriented, which means that it captures the effects of different wind farm control strategies on fatigue loading. This model includes **wake steering**, by yaw misalignment and also **curtailment**, which involves deliberately limiting power generation. An overview of the model is given in Table 3-1.

3-1-1 Synthetic Data Generation

Panel (a) in Figure 3-1 can be seen as the synthetic data generation. To accurately capture structural loading, data from aero-servo-elastic simulations including dynamic wake effects is necessary; the

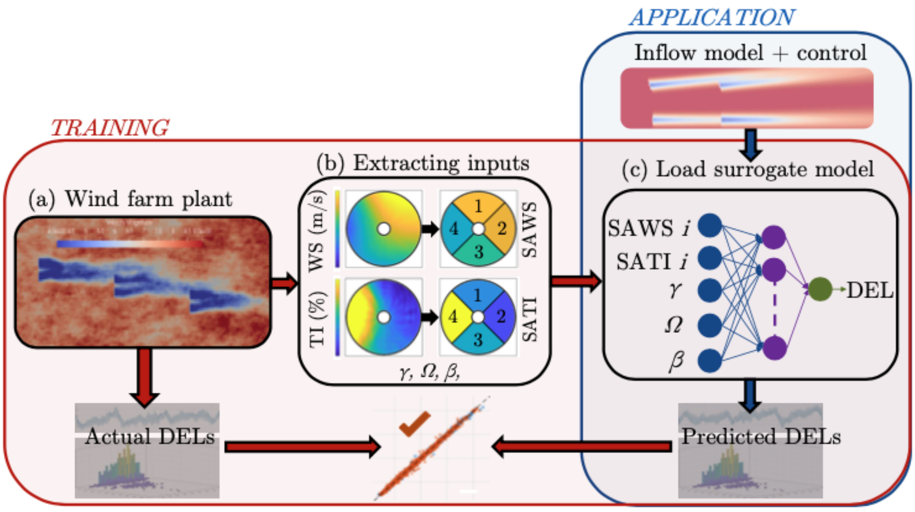

Figure 3-1: A general approach of load surrogate modeling [8].

Table 3-1: Overview of the sector-average load surrogate model [9].

Simulation code	FAST.Farm
Turbine model	IEA 3.4MW [59], IEA 22MW [60]
Number of turbines in training simulations	3
Surrogate inputs	Sector-averaged wind speeds (SAWS), sector-averaged turbulence intensities (SATIs), blade pitch angle, rotor speed, yaw misalignment
Surrogate function	Shallow Artificial Neural Network (ANN)

TUM model uses FAST.Farm [42] to compute local inflow and structural loading for each turbine in a farm. This framework integrates individual turbine simulations with OpenFAST [61] and utilizes the dynamic wake meandering (DWM) model [41] to compute wake interactions. The requirement of panel (a) is to get 10-minute DELs measurements and local inflow characterization from the aero-servo-elastic simulation.

3-1-2 Damage Equivalent Loads

The considered load channels are the following:

- **Blade root DEL**: blade root in-plane and out-of-plane bending moments
- **Shaft DEL**: shaft out-of-plane and yaw bending moments.
- **Yaw bearings DEL**: tower top fore-aft and side-side bending moments
- **Tower base DEL**: tower bottom fore-aft and side-side bending moments.

The considered components are shown in Appendix A, Figure A-1, together with the corresponding orientations of the bending moments in Figure A-2 and Figure A-3. For each time series, the 10-minute DEL is computed using the formula:

$$DEL = \left(\frac{\sum(n_i L_i^m)}{N_{eq}} \right)^{\frac{1}{m}} \tag{3-1}$$

where n_i is the number of load cycles of amplitude L_i, N_{eq} is the equivalent number of cycles (taken as per convention at 2×10^6 cycles over a lifetime of 20 years), and m is the Wöhler exponent of the S-N curve of the material (m=10 for the polymer material of the blades and $m = 4$ for the steel material of the main shaft and tower) [9]. For each load location, and at each time step, the two orthogonal load components are combined and projected onto all possible directions, with an angular step of 10 degrees. For each 10° section, this produces a time series of the directional load magnitudes, from which the corresponding DELs are computed using (3-1) [8]. The section with the maximum value is then taken as the representative fatigue load for that condition.

3-1-3 Inputs to the Surrogate

A consideration in the design process of a surrogate model is the selection of local inflow characteristics that are complex enough to capture the variation of fatigue loads across the wind farm, while being simple enough to be accessible for use in real-time and fast-response applications. Panel (b) in Figure 3-1 can be seen as post-processing the time series of the channels into quantities relevant for the surrogate model. For the TUM model these are the Sector-averaged wind speeds (SAWS) and Sector-averaged turbulence intensities (SATIs) across the rotor disk. Dividing the rotor plane into four sectors with their corresponding SAWS and SATIs (Figure 3-2) was found to be sufficient to achieve a desired level of accuracy.

In addition to the local inflow quantities, yaw misalignment is included as an input to account for the effects of wake steering. To capture the effect of curtailment, rotor speed and blade pitch angle are also incorporated. Altogether, the surrogate model uses 11 inputs: 4 SAWS, 4 Sector-averaged turbulence intensitiess (SATIs), yaw misalignment, rotor speed and blade pitch angle.

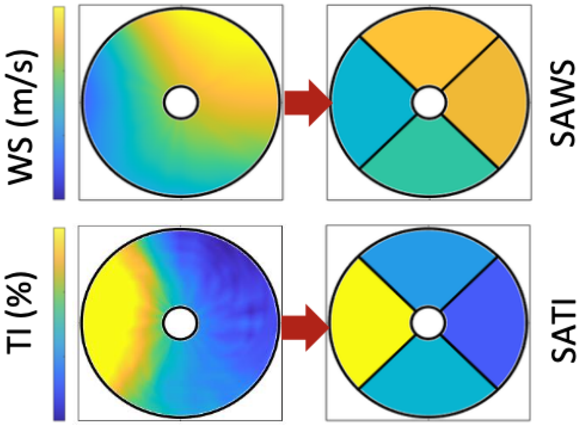

Figure 3-2: Processing the wind speeds and turbulence intensity into SAWS and SATIs [9].

3-1-4 Surrogate Function

After the dataset is constructed, it is randomly shuffled and split into a training and testing set. Panel (c) in Figure 3-1 can then be replaced by a fitting surrogate function. In the sector-averaged load surrogate model, this is a shallow Artificial Neural Network (ANN). For each load channel, a separate ANN is trained, consisting of one layer with 30 neurons. Once trained, each network can be evaluated as a simple mathematical function in fractions of a second, enabling complex optimization- and control-based applications.

3-2 Load Surrogate Model Implementation in OFF

This section describes the step-by-step implementation of the load surrogate model in the OFF framework. The inputs required for the sector-averaged load surrogate model can be reduced to nine for the purpose of wake-steering: four SAWS, four SATIs, and the turbine's yaw misalignment. Chapter 2 explained how in the OFF framework, the wind farm is evaluated by FLORIS at each time step; this means that the surrogate model is also indirectly implemented in NREL's FLORIS model [25]. A wake model in FLORIS is made up of four components that together constitute a wake; the Gaussian velocity deficit model [50], the Jimenez deflection model [48], the Crespo-Hernandez turbulence model [49] and, finally, the Sum of Squares Freestream Superposition (SOSFS) method is used for combining wakes to capture the coupled effects. These models were described in detail in Chapter 2.

Extracting the inputs is done in 3 steps:

1. **Create the rotor plane.** The rotor grid is created by defining a polar mesh with the radius of the rotor plane and azimuth angles from 0 to 2π, which is then converted into a 3D Cartesian grid that rotates with the yaw misalignment of the turbine. Although more advanced point distributions could be used to capture local variations in inflow, the uniform polar grid is computationally efficient and sufficient for this surrogate model.

2. **Sample the wind speed and the turbulence intensity across the rotor plane.** For each point on the rotor grid, the wind speed is obtained with the FLORIS function `sample_flow_at_points`.

To sample the turbulence intensity (TI), a similar function was developed that computes the full turbulence field and samples values at specified coordinates.

3. **Average the wind speed and the turbulence intensity into four sectors.** To compute the SAWS and SATIs, the rotor plane is divided into four sectors. Next, the wind speed and turbulence intensity are averaged for all grid points within each sector; this process is shown in Figure 3-6.

Example: Three-turbine case

To demonstrate the implementation, a test case with three (IEA 3.4MW [59]) turbines in a straight row layout is considered. The turbines are spaced six rotor diameters apart, and the inflow wind direction is aligned with the turbine row. The ambient TI is set to 6% and the inflow wind speed to 10 m/s. In this setup, the most upstream turbine (T0) operates in free flow under ambient conditions, while T1 operates in the wake of T0, and T2 operates in the wakes of both T0 and T1. The first turbine is intentionally yawed by 30° to deflect the wake and make the resulting changes in the downstream flow field visible. Figure 3-3 illustrates the resulting flow field and wake deflection for this set-up. As described in subsection 3-1-1, *Synthetic data generation*, a FAST.Farm dataset of 30 783 simulation cases was created from this three-turbine setup. For each operating point, the input variables to the load surrogate model are the SAWS, the SATIs and the turbine's yaw misalignment. The corresponding outputs are the DELs on the four load channels, mentioned in the previous section. This dataset was then used to train the load surrogate model and therefore serves as a reference for subsequent analysis.

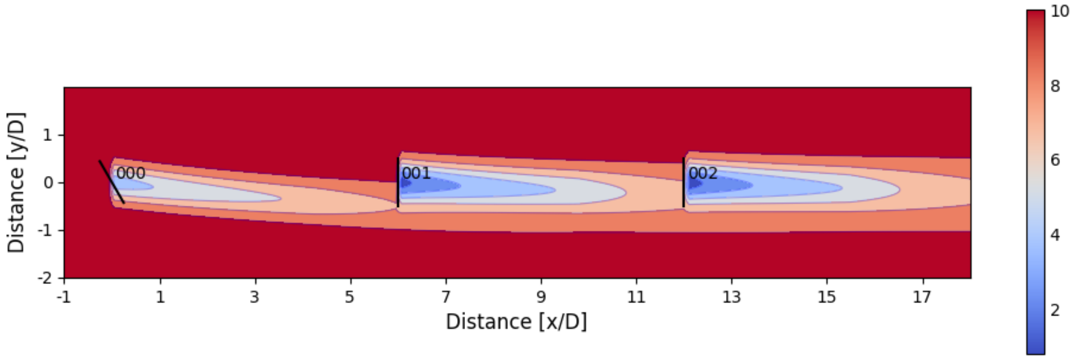

Figure 3-3: Horizontal plane at hub height (110 m) of the wind speed field for the three-turbine simulation case, where the first turbine (T0) is yawed by 30°. The inflow wind direction is aligned with the turbine row, and the turbine spacing is six rotor diameters. The wake deflection, caused by the yawed upstream turbine, and its impact on the downstream turbines are clearly visible.

The resulting wind speed and TI distributions over the rotor planes are shown in Figure 3-4. The TI shows a uniform distribution across the rotor cross-sections with sharp boundaries, consistent with the Crespo–Hernandez model [49], which assumes uniform turbulence intensity in the wake cross-section, as can be seen in Figure 3-5. In the final step, the rotor plane is divided into four sectors and the values are averaged to obtain the SAWS and SATIs (see Figure 3-6 for the wind speed; the same procedure is applied for the TI). A challenge encountered during the sampling process was that the rotor plane partially rotates into its own created wake when a yaw misalignment angle is applied. This effect is visible for T0 in Figure 3-3. Appendix B discusses several possible solutions to avoid this.

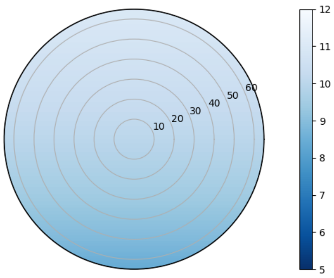

(a) Wind speed across the rotor plane of T0.

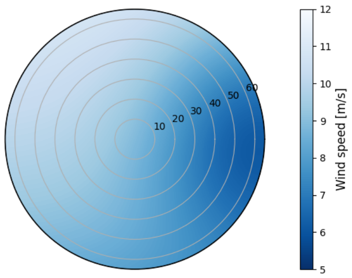

(b) Wind speed across the rotor plane of T1.

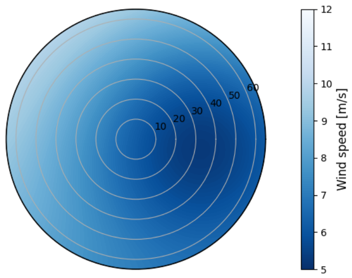

(c) Wind speed across the rotor plane of T2.

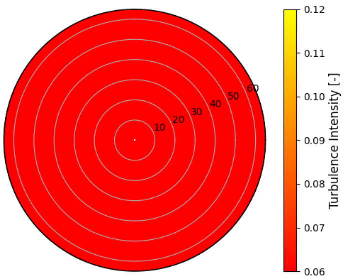

(d) Turbulence intensity across the rotor plane of T0.

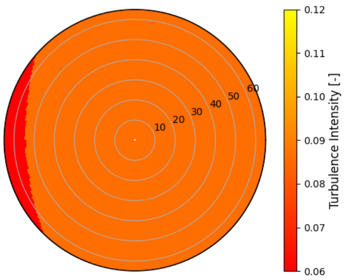

(e) Turbulence intensity across the rotor plane of T1.

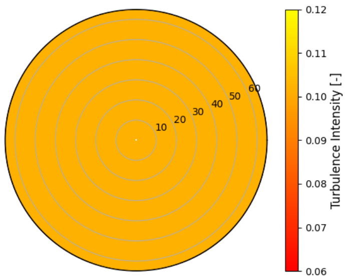

(f) Turbulence intensity across the rotor plane of T2.

Figure 3-4: Top row: wind speed sampled across the rotor planes of T0 (3-4a), T1 (3-4b), and T2 (3-4c) for the case in Figure 3-3. Bottom row: turbulence intensity distributions for the corresponding turbines (3-4d, 3-4e, 3-4f).

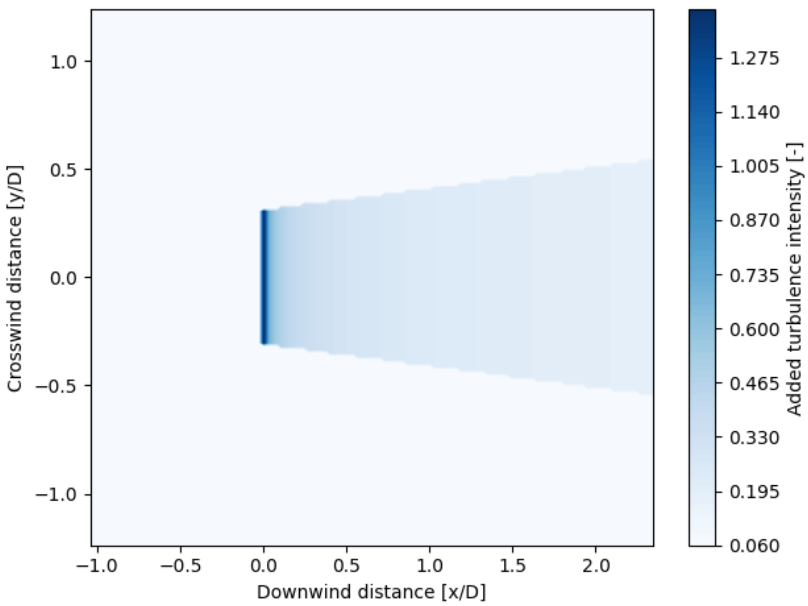

Figure 3-5: Added turbulence intensity field according to the Crespo-Hernandez model [49]. The model shows the spatial growth of turbulence intensity downstream of the turbine, assuming a uniform distribution across the wake cross-section.

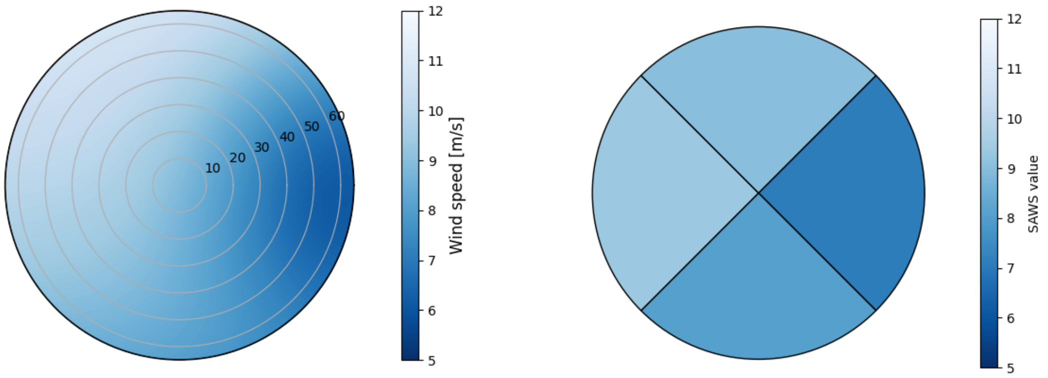

(a) Wind speed field across the rotor plane of T1

(b) Sector-averaged wind speeds (SAWS) for T1, obtained by dividing the rotor plane into four sectors.

Figure 3-6: From the sampled wind speed field (3-6a) across the rotor plane of T1, the rotor plane is divided into four sectors, and the SAWS are computed (3-6b). The SAWS values per sector are 9.4 m/s (left), 9.2 m/s (up), 8.0 m/s (down), and 7.1 m/s (right). The same procedure is applied to compute the SATIs.

Load Surrogate Model Performance in OFF

To evaluate the performance of the load surrogate model functions in OFF, the predicted DELs were compared against the reference values from FAST.Farm, demonstrated in Figure 3-7. In the figure, the solid lines represent the reference DELs from the FAST.Farm dataset, while the dashed lines show the corresponding surrogate predictions for all three turbines. The surrogate somewhat captures the trends in wind direction and yaw misalignment, but the accuracy was not yet sufficient for application of the load surrogate model.

To better understand where these differences come from, the surrogate inputs, the SAWS and SATIs computed in OFF, were compared with the input values from the FAST.Farm training dataset. The SAWS showed a good match in both values and trends, whereas the SATIs deviated significantly.

These deviations can be explained by fundamental differences in underlying submodels that make up wake models. Different wake models use different modelling approaches for aspects such as velocity deficit, wake deflection, TI and the wake structure. As a result, running the same wind farm simulation in different wind farm models can give different flow characteristics.

In this case, the largest error in the inflow quantities comes from differences in the turbulence models. FAST.Farm applies an Ishihara-based model developed by Ishihara *et al.* [62], which relies on a double-Gaussian wake description, as shown in Figure 3-8. In this model, the wake velocity deficit is represented by two Gaussian profiles that correspond to the shear layers on either side of the wake centerline. This formulation produces a more detailed spatial distribution of TI and defines it locally, normalized by the local mean wind speed at hub height. In contrast, the Crespo-Hernandez model [49], used in OFF, adopts a more global definition of turbulence intensity, resulting in lower values in the wake.

These lower TI values lead to an underestimation of the computed DELs. Figure 3-9 illustrates this effect by comparing the DEL predictions of the load surrogate model functions, trained on the FAST.Farm dataset, when applied to inputs from OFF against when applied to inputs from the

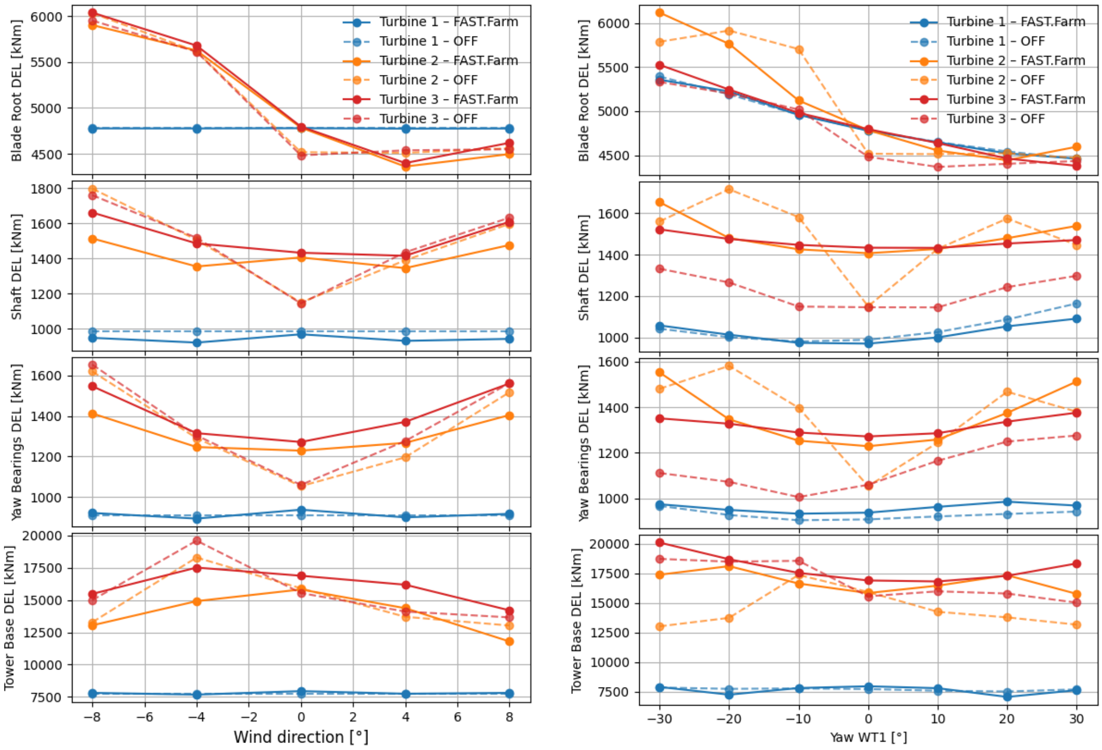

(a) Comparison of surrogate-predicted and reference DELs as a function of wind direction for all three turbines.

(b) Comparison of surrogate-predicted and reference DELs as a function of upstream turbine yaw misalignment.

Figure 3-7: Surrogate-predicted DELs trends for all turbines compared with the reference DELs from the FAST.Farm training dataset.

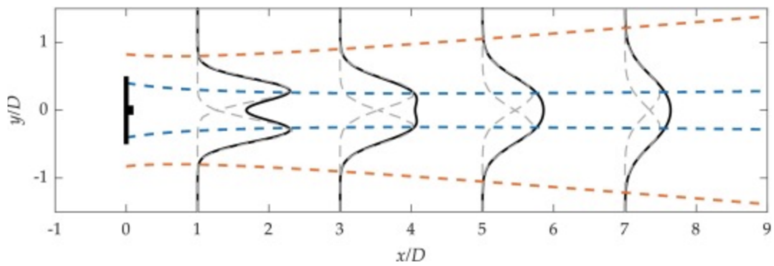

Figure 3-8: The double-Gaussian wake model in the Ishihara model [62]. The black solid line represents the resulting double-Gaussian velocity deficit profile, with the single-Gaussian function as gray dashed lines. The blue dashed lines represent the Gaussian extrema and the orange dashed lines the wake boundary.

FAST.Farm dataset itself. Since curtailment is outside the scope of this thesis, the dataset was reduced to 8 289 cases with a power demand of 100%. The x-axis represents the surrogate predicted DELs using the FAST.Farm inputs, while the y-axis represents the predictions using the corresponding OFF inputs. The result, clustered by rotor-averaged incoming wind speed, shows an underestimation of the predicted DELs on the OFF inputs, which can be explained by the lower TI values resulting from the Crespo-Hernandez model [49]. To quantify the performance, the root mean squared percentage error (RMSPE) was calculated for each load channel.

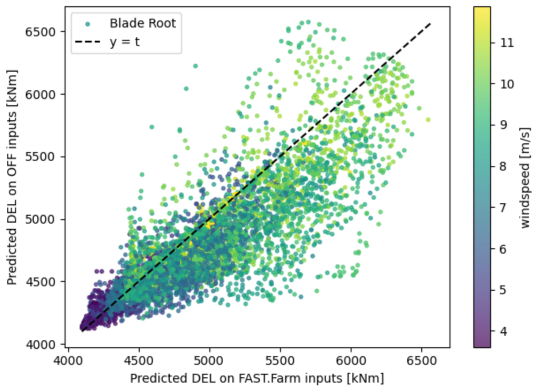

(a) Blade root - RMSPE 5.09%

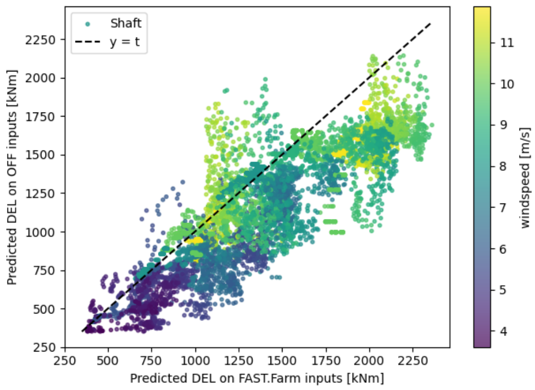

(b) Shaft - RMSPE 20.65%

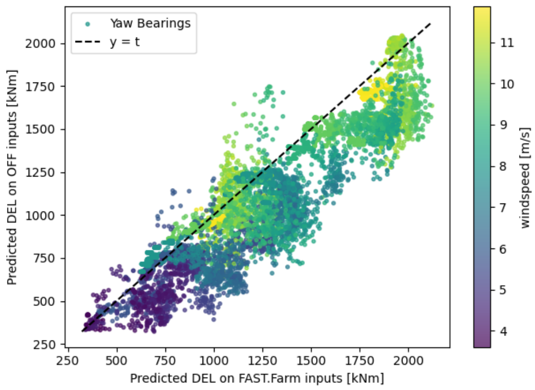

(c) Yaw bearings - RMSPE 19.05%

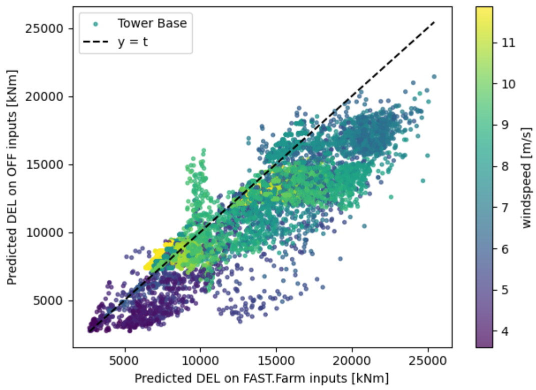

(d) Tower base - RMSPE 19.19%

Figure 3-9: Baseline performance: FAST.Farm-trained surrogate model functions evaluated on OFF inputs for 8 289 simulation cases across the four load channels, clustered by rotor averaged wind speed.

Rescaling the TI Field

To improve agreement and correct for the underestimation, the entire TI field in OFF was rescaled by the ratio of the ambient to the local wind speed,

$$\tilde{I} = I * \frac{u_{ambient}}{u_{local}}, \tag{3-2}$$

which increases the TI in wake regions where the local wind speed is reduced.

The motivation for this correction comes from the normalization approach used in the Ishihara model [50], where the TI is defined relative to the mean wind speed at hub height U_h [31].

$$I = \frac{\sigma_u}{U_h}, \tag{3-3}$$

where σ_u is de turbulence standard deviation.

In contrast, the Crespo-Hernandez model [49] defines the total TI as the combination of the initial ambient turbulence I_0 and the sum of the added turbulence, I_j^+ from upstream turbines:

$$I = \sqrt{\sum_{j=0}^{N} (I_j^+)^2 + I_0^2}, \tag{3-4}$$

where the equation for I_j^+ is given in Equation 2-6.

By applying this rescaling, the TI shifts from a global to a more local formulation, since the normalization now depends on the local wind speed rather than the ambient inflow. This adjustment increases the SATIs within the wake, where the local wind speeds are reduced, and therefore produces a more realistic spatial distribution of TI across the rotor plane. The effect of this correction can be seen in Figure 3-10, where the RMSPE decreases for all load channels.

The correction reduces the RMSPE per channel. However, the vertical clusters of points, already visible in Figure 3-9, remain. These cases correspond to high wind speeds with small turbine spacing, where downstream turbines operate in stronger wakes. Under these conditions, wake models, designed primarily for far-wake regions, struggle to accurately represent the complex turbulence of near-wake interactions. As a result, differences in how the velocity deficit and turbulence intensity are modeled lead to larger deviations in the inflow quantities. After applying the rescaling, the TI in these regions increases, further amplifying the vertical spread of these clusters in Figure 3-10.

Retraining the Load Surrogate Model

Since this adjustment did not provide sufficient accuracy, two further steps were considered: (i) extending OFF with the Ishihara model to better match the flow characteristics in FAST.Farm, or (ii) retraining the load surrogate model using inputs generated by OFF with the DEL outputs from the FAST.Farm dataset. The second option was chosen to ensure consistency between the training and application environment.

Retraining the load surrogate model on OFF-generated inputs further reduced the RMSPE across all load channels, as shown in Figure 3-11. This retraining was performed externally, therefore the training procedure itself could not be adjusted. Consequently, possible improvements, such as using higher-order neural networks or more advanced architectures, could not be explored. Moreover, retraining still combines inputs from OFF with outputs from FAST.Farm and while this improves consistency at the input level, it does not fully eliminate the underlying differences between the two modeling frameworks. However, this final performance provides a consistent and reliable basis for use in the subsequent case studies and control strategies presented throughout this thesis.

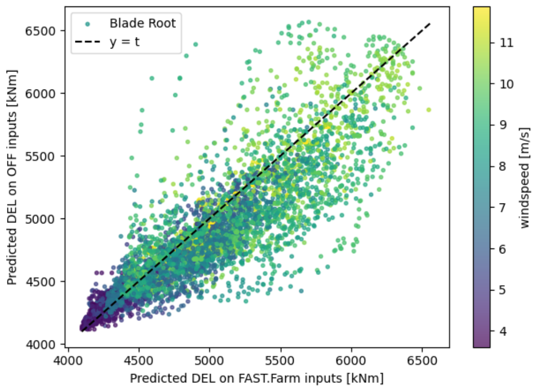

(a) Blade root - RMSPE 4.44%

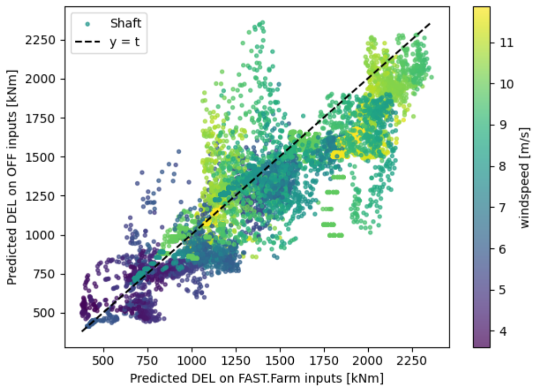

(b) Shaft - RMSPE 16.76%

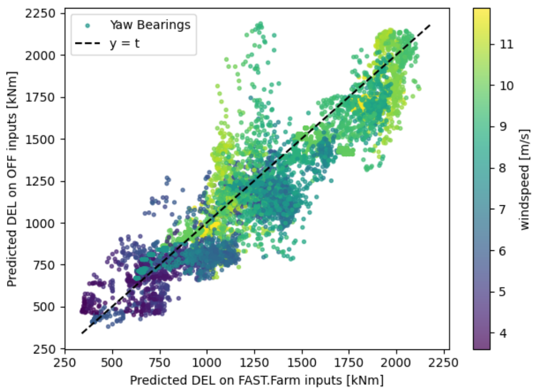

(c) Yaw bearings - RMSPE 14.77%

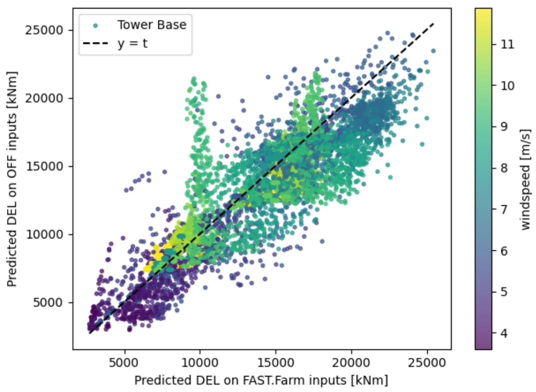

(d) Tower base - RMSPE 17.92%

Figure 3-10: Performance after rescaling the TI field: FAST.Farm-trained surrogate model functions evaluated on OFF inputs for 8 289 simulation cases after rescaling the TI field, across the four load channels clustered by rotor averaged wind speed.

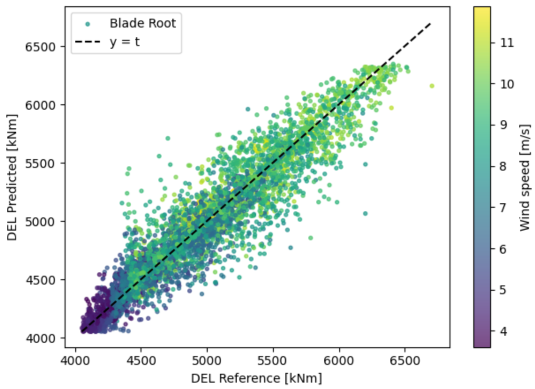

(a) Blade root - RMSPE 2.89%

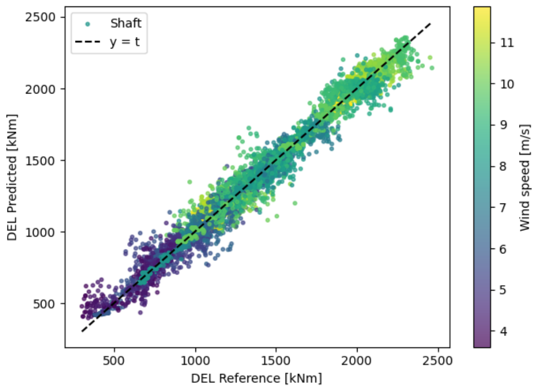

(b) Shaft - RMSPE 6.60%

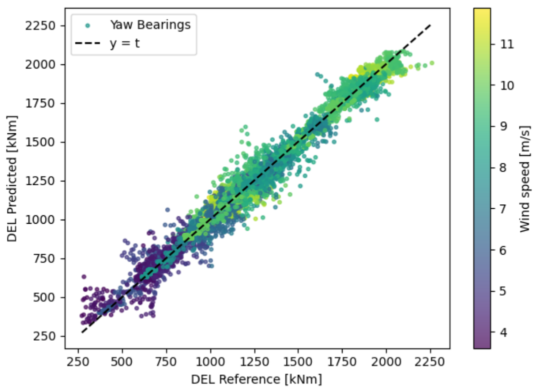

(c) Yaw bearings - RMSPE 6.51%

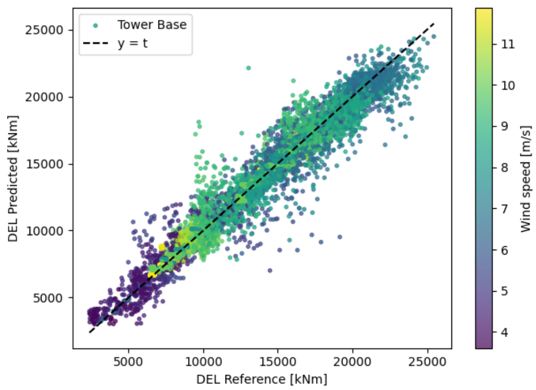

(d) Tower base - 9.50 %

Figure 3-11: Final performance: OFF-trained surrogate model functions evaluated on OFF inputs for 8 289 simulation cases across the four load channels against the reference FAST.Farm DELs from the dataset, clustered on rotor averaged wind speeds.

3-2-1 The Effect of Sampling Time

After validating the sector-averaged load surrogate model in steady-state conditions, it can be applied in a dynamic simulation. The load surrogate model was trained on dynamic simulations in which the inflow, ambient conditions, and turbine operation setpoints were kept constant within each case, so that the predicted DELs represent the 10-minute equivalent loads associated with those fixed conditions. Consequently, the model is designed for static use, and Guilloré *et al.* [8] do not provide a methodology for applying it in dynamic simulations. In dynamic simulations, where the inflow conditions and turbine control setpoints continuously vary, the inflow quantities fluctuate over time. There are several possible approaches for applying the load surrogate model in dynamic cases, such as averaging the inflow quantities over a given time window and using these mean values as inputs to the surrogate, or computing the DELs over discrete time intervals. The latter approach was considered to be the most suitable, as it better captures transient load variations and can be integrated into fast-updating control strategies. This choice makes the sampling interval an important design parameter. A shorter sampling interval allows the surrogate to capture fast load fluctuations more accurately but increases computational cost, as the flow field must be solved more frequently. In contrast, a longer sampling time reduces computational time, but risks missing relevant load dynamics.

To investigate this trade-off, a one-hour simulation with a varying wind direction was performed using a DEL output sampling time of $\Delta t = 2s$. The resulting instantaneous DEL signals for the one-hour simulation were segmented into six ten-minute intervals. The DEL time series in each segment were then downsampled from the original $2s$ resolution up to $20s$ resolution, in order to illustrate how load fluctuations are missed when using a larger DEL sampling time.

This analysis focuses solely on the yaw-bearing channels of turbines T1 and T2, as they exhibit strong variability and clear fluctuations in instantaneous DEL values because they operate in waked conditions.

Figure 3-12 shows the yaw-bearing channel of turbine T1 during the third segment for several downsampled DEL outputs. The reference case with a sampling time of $\Delta t = 2s$ is shown in black. As the sampling interval increases, high-frequency fluctuations in the instantaneous DEL output are increasingly missed, showing the loss of dynamic fidelity.

To quantify this trade-off between accuracy and computational efficiency, a Pareto-type curve was constructed. To evaluate how well the different sampling times capture the trends and fluctuations of the DELs, the fatigue damage rate was calculated based on the formulation in [63].

First, the per-step damage was calculated as

$$d_{jt} = DEL_{jt}^{m} \Delta t, \tag{3-5}$$

where $j = 1,2$ denotes the turbine index and $m = 4$ is the Wöhler exponent for the yaw-bearing channel. The cumulative fatigue damage per turbine is then obtained by

$$D_j = \sum_t d_{jt}, \tag{3-6}$$

and the fatigue damage rate is defined as

$$\text{Damage rate} = \frac{D_j}{t_{sim}}. \tag{3-7}$$

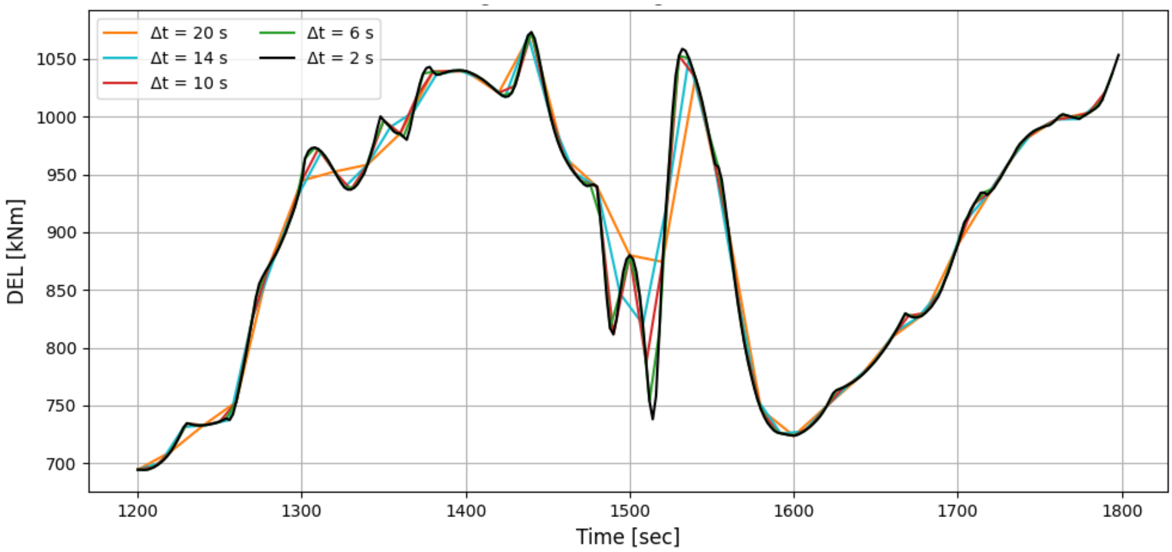

Figure 3-12: Output time series of instantaneous computed DEL for the yaw-bearing channel of T1 for different DEL sampling times during the third segment of the one-hour simulation. Larger sampling intervals increasingly miss dynamic load fluctuations.

The computed fatigue damage values and simulation times were normalized with respect to the baseline case with $\Delta t = 2s$. The resulting trade-off curve is shown in Figure 3-13. Each color represents a sampling time, and the six points per color correspond to the six ten-minute segments. The points for each sampling time are vertically aligned because the simulation time was measured once per DEL sampling interval.

The result shows that sampling times up to approximately 8-10 seconds provide a computational time reduction of approximately 54-57% with only a small loss in accuracy, while larger intervals lead to a rapid increase in fatigue damage error. A trade-off can therefore be made depending on the use case. Since the control strategy considered in the case study does not require a high computational speed and the analysis focuses on comparing achievable load reductions over relatively short time periods, a DEL sampling time of $5s$ is selected to prioritize accurately capturing all load fluctuations.

3-3 Summary

This chapter presented the implementation and validation of the sector-averaged load surrogate model within the OFF framework, thereby addressing Research Question 1 and its sub-questions. The required sector-averaged inflow quantities (SAIQs) were successfully extracted, but the evaluation showed clear discrepancies between FAST.Farm and OFF that were caused by fundamental differences in wake modeling definitions. These inconsistencies led to mismatches in SATI values and, consequently, significant deviations in the predicted DELs.

To reduce these discrepancies, normalizing the TI field in OFF by the local wind speed improved the spatial TI distribution across the rotor plane and partially mitigated the underestimation of the predicted DELs. Retraining the surrogate model using SAIQs extracted from OFF further improved prediction accuracy. The scatterplots in Figure 3-11 show that the retrained surrogate achieved both lower RMSPE values and better trend agreement. The reduction in RMSPE across all evaluated

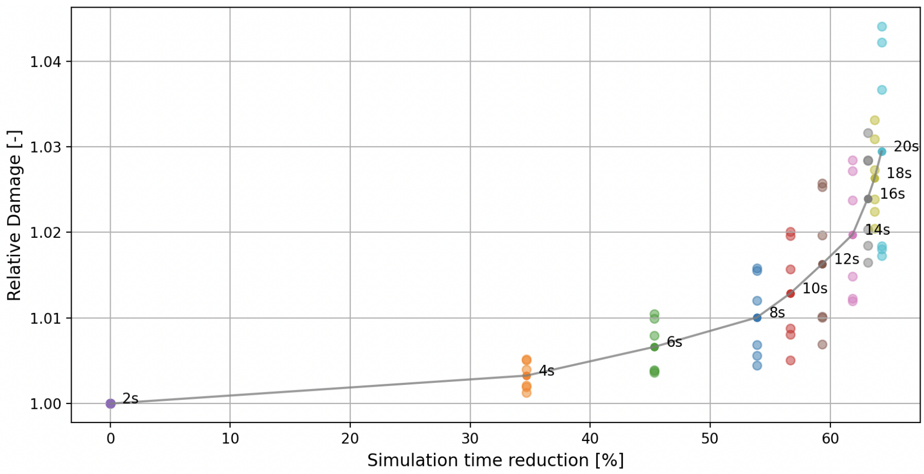

Figure 3-13: Pareto curve illustrating the trade-off between computational speed and fatigue damage accuracy as a function of the DEL sampling time. Results are shown for the yaw-bearing channel of turbines T1 and T2. Both axes are normalized to a sampling time of $\Delta t = 2$.

improvement steps shows that rescaling the TI field reduced the error relative to the baseline, while retraining the surrogate on OFF extracted inputs provided the largest improvement. These findings address Sub-question 1.3 and are summarized in the bar chart in Figure 3-14.

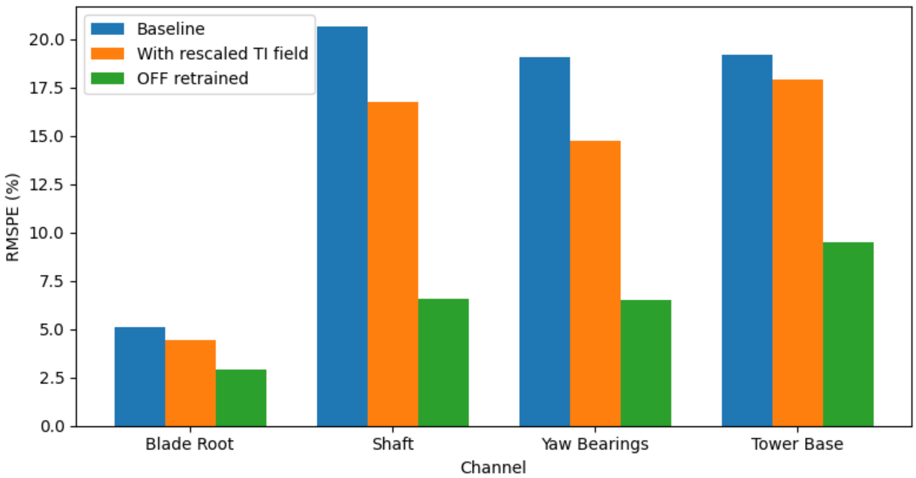

Figure 3-14: RMSPE per load channel between predicted and reference DELs (evaluated on the same OFF inputs) for all 8 289 cases. The bar chart shows that rescaling the TI field reduced the RMSPE, but retraining the load surrogate functions using SAIQs extracted from OFF led to the largest improvement.

Finally, Sub-question 1.4 was addressed by analyzing how the choice of DEL sampling time influences the trade-off between computational efficiency and relative damage accuracy. Shorter sampling times capture load fluctuations more accurately but increase computational cost, while longer sampling times smooth out the signal and fail to capture important load variations. A sampling time of $5s$ is selected in this thesis, as it prioritizes damage accuracy while still providing sufficient computational efficiency.

Overall, this chapter established the role and capabilities of the load surrogate model within OFF and demonstrated both the potential and challenges of transferring surrogate models across different wind farm frameworks.

Chapter 4

A Balanced Power-Load Control Strategy

In this chapter, the three main components of this thesis come together:

1. a dynamic wind farm flow model,
2. a load surrogate model, and
3. a controller.

This chapter addresses Research Question 2, in particular Sub-questions 2.1 and 2.2. The contributions and outline are as follows. Section 4-1 describes the dead-band Look-up Table (LuT)-based yaw controller implemented OFF and its required inputs. Section 4-2 then presents the formulation of a power-load balanced objective function for LuT generation in FLORIS and motivates the inclusion of tower base fatigue loads in the control objective. Finally, the trends in tower base fatigue loads are analyzed to explain the corresponding optimal yaw misalignment behavior of the controller.

4-1 Yaw Steering Dead-Band Control in OFF

The primary objective of this thesis is to integrate and evaluate the sector-averaged load surrogate model within a dynamic wind farm flow model, and to demonstrate how this implementation can be used to make load-aware yaw control decisions. To evaluate this objective, a LuT-based control strategy is developed and applied. This approach can be applied in both the steady-state model FLORIS and the dynamic model OFF, allowing a transparent comparison between the two and making the effect of added flow dynamics clearly observable. It also provides a straightforward way to verify whether control decisions designed in a steady-state context remain effective in a dynamic framework. By avoiding the added complexity of more advanced control strategies, the LuT-based control method allows a clear assessment of the trade-off between power maximization and fatigue-load reduction. More advanced model-based and load-aware control remains important future work, making the controller more robust to inflow uncertainty, disturbances, and modeling inaccuracies, once the behavior of the load surrogate in a dynamic environment has been investigated.

The LuT-based yaw steering dead-band controller in OFF is described by Becker *et al.* in [4], who based their design on the work by Kanev in [64]. The controller maintains an estimate of the wind direction $\hat{\varphi}$, which is used to evaluate the LuT and determine the yaw misalignment setpoints.

The estimate $\hat{\varphi}$ is updated based on its current value and the wind direction input signal. An update occurs when either the difference between the estimate and wind direction input exceeds a predefined dead-band limit, or when a smaller difference persists over multiple time steps such that the accumulated difference, scaled by a predefined integration coefficient, exceeds the same limit. The controller's behavior is described by the following equation from [4]:

$$\hat{\varphi}(k) = \begin{cases} \varphi_f(k), & \text{if } |\varphi_f(k) - \hat{\varphi}(k)| > \varphi_{\lim} \text{ or } k_i \left|\sum_{\tau}^{l=k-1} \varphi_f(l) - \hat{\varphi}(k)\right| > \varphi_{\lim} \\ \hat{\varphi}(k-1), & \text{otherwise} \end{cases} \tag{4-1}$$

$$\gamma(k) = f_{LuT}(\hat{\varphi}(k)), \tag{4-2}$$

where τ denotes the time step of the last update of $\hat{\varphi}(k)$, $\varphi_f(k)$ represents the wind direction signal at time step k, φ_{lim} is the dead-band width, and k_i is the integration coefficient determining the sensitivity to persistent small deviations. $\gamma(k)$ is the optimal yaw misalignment for the wind direction estimate, obtained from the LuT.

The controller needs four elements; the wind direction signal $\varphi_f(k)$, the dead-band width φ_{lim}, the integration coefficient k_i, and the LuT f_{LuT}. Section 4-2 describes how the LuT is generated, while Chapter 5 discusses the wind direction signal $\varphi_f(k)$ and the motivation behind the selection of φ_{lim} and k_i.

In [4], Becker *et al.* conducted a study for 81 combinations of dead-band and integration coefficient values. The performance of these combinations was evaluated using a Pareto curve, illustrating the trade-off between the gain in farm energy and the corresponding increase in yaw travel.

4-2 Formulation of the Objective Function

The first step is to incorporate the predicted DELs into the optimization framework. Several approaches exist to do this. For example, Liew *et al.* [10] formulate the problem using the predicted DELs as constraints. Alternatively, DELs can be translated into other metrics, such as estimated turbine lifetime or maintenance costs, which can then be included in the objective function.

Here, the objective function is formulated following the "load-balance" approach of Anand *et al.* [65]:

$$J(\gamma) = W_P \frac{\sum_i P_i(\gamma)}{\sum_i P_{i,bl}} - W_L \frac{max_i DEL_i^{TB}(\gamma)}{max_i DEL_{i,bl}^{TB}}, \tag{4-3}$$

where i denotes the turbine index. $P_i(\gamma)$ is the power of turbine i under the yaw misalignment γ. The load term represents the tower base DEL of the most heavily loaded turbine in the farm. By penalizing only the maximum load, the formulation aims to reduce the farm-wide maximum fatigue load. This allows turbines with larger available load budget to be used more, while turbines experiencing higher loads are relieved, resulting in a more balanced load distribution across the farm [65]. The weighting coefficients W_P and W_L determine the balance between power maximization and tower base load reduction, and therefore set the relative priority between the two objectives.

The optimization is performed by the Serial Refine (SR) algorithm in FLORIS [66], which conducts a grid search over the yaw angles by evaluating a coarse grid across the allowed yaw range. This process is performed sequentially for each turbine, proceeding from upstream to downstream. The turbines were permitted a yaw misalignment of $\pm 25^\circ$, while the third turbine (T2) was constrained to 0°, which means it is aligned with the wind direction at all times. To derive the LuT, the TI was fixed at 6%, the wind speed at 8 m/s, and the wind direction discretized into 1° bins. For each discrete wind direction, the yaw misalignment set γ that maximizes $J(\gamma)$ is selected. This procedure yields a LuT that provides optimal yaw setpoints for every wind direction. The conditions were selected to match the case study in Chapter 5.

Motivation for Including Tower Base Loads

The motivation for including tower base loads in the objective was made through an analysis using a sinusoidal wind direction signal applied to the three-turbine case. For each turbine and load channel, the relative increase in DELs was computed with respect to turbine T0 under the baseline controller. T0 was chosen as the reference because it operates in the 'ideal' situation, unaffected by wakes from upstream turbines. The results show that the tower base loads experience the largest relative increase when turbines operate under waked conditions, exceeding 100% for T1 and T2. This indicates that tower base loads are the most sensitive to wake-influenced inflow, making the tower base DEL a suitable load metric to include in the objective function, as it represents a channel where wake steering has a great potential to reduce fatigue loads. Figure 4-1 presents the distributions of relative DEL changes during a sinusoidal wind direction signal for two control strategies; the baseline case, where all turbines align with the wind, and a wake-steering case, where a yaw misalignment is applied to increase farm power. These boxplots illustrate the sensitivity of all considered load channels to operating in waked conditions.

Furthermore, Thedin *et al.* [67] state that the tower base channel, among others, provides a solid basis to draw conclusions from because it directly affects the main components of the turbine. They also observed that, under aligned flow, any yaw misalignment introduced by a LuT-based controller leads to an increase in tower base loads. This effect was also observed throughout this thesis and is supported by Figure C-2 in Appendix C, where the DEL response of a turbine operating without wake interaction shows that yaw misalignment introduced by the LuT-based controller increases DEL compared to the baseline controller. The increase in DEL resulting from wake steering further supports the decision to include the tower base channel in the balanced power-load control.

Influence of Power-Load Weighting on Optimal Yaw Misalignment Behavior

For generating the LuTs, six different power-load weighting balances are considered, ranging from the traditional power-only optimization (1:0) to a load-only optimization (0:1). Table 4-1 summarizes all configurations with a brief description.

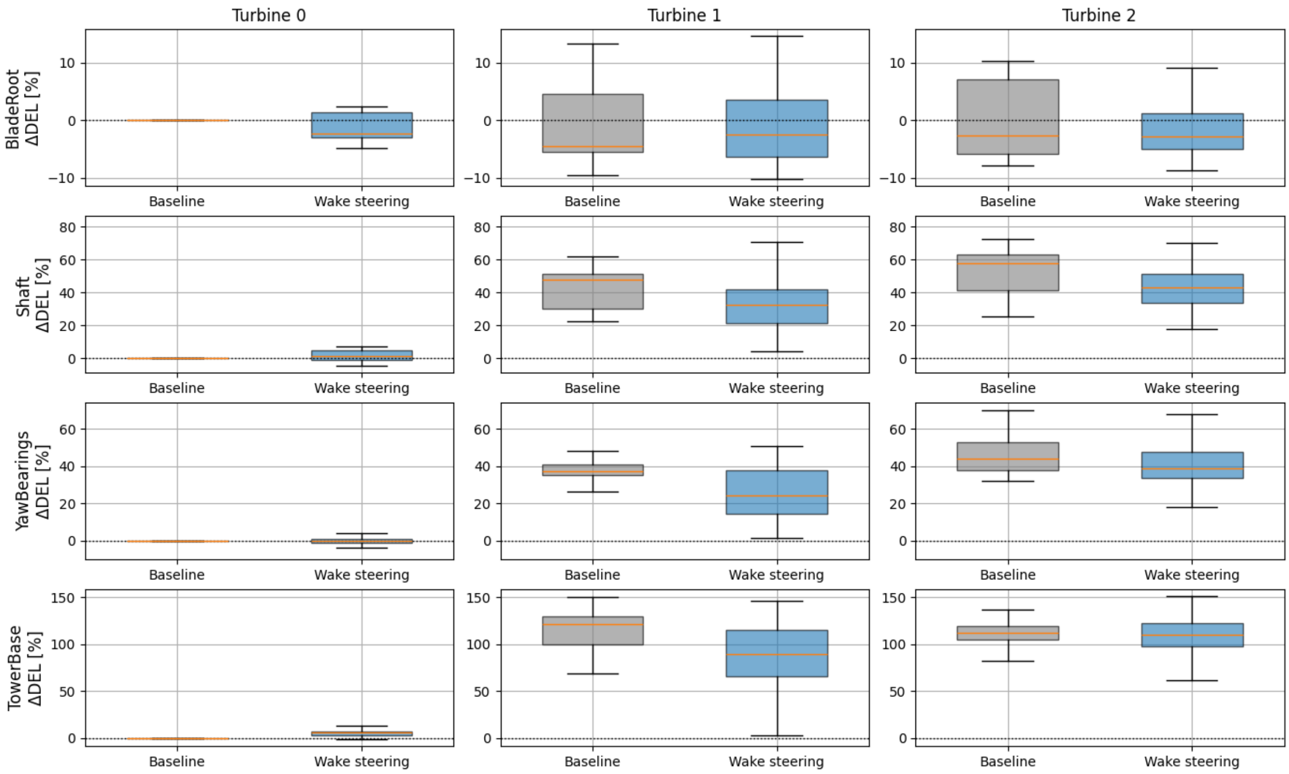

Figure 4-1: Distributions of relative DEL changes obtained from a sinusoidal wind direction signal for two control strategies; the baseline case, where all turbines align with the wind, and a wake-steering case, where yaw misalignment is applied to increase power generation. The boxplots highlight the sensitivity of the load channels to operating in waked conditions. All DEL changes are relative to the baseline of T0, which represents the ideal, unwaked case. The highest relative increase in tower base loads motivated the inclusion of this load channel in the objective function.

Table 4-1: Power–load ($W_P - W_L$) weighting configurations used for generating the LuTs.

Power–load balance	Description
1:0	Power-only optimization
1:0.3	Power-oriented optimization
1:0.8	Balanced optimization
0.7:1	Load-oriented optimization
0.5:1	Load-biased optimization
0:1	Load-only optimization

When examining the generated LuTs, the influence of the power-load weighting on the optimal yaw misalignment behavior in the three-turbine case becomes apparent. Two interesting observations can be made.

- When loads are included in the objective function, the wind direction range in which yaw misalignment angles are applied increases compared to a power-only optimization.
- Second, around the critical 270° wind direction, when all turbines are aligned with the incoming flow, yaw misalignment is not applied and the controller instead follows the wind direction, similar to the baseline controller.

The first observation can be attributed to the fact that the TI field extends over a broader lateral distance that the wind speed deficit field. For instance, at a wind direction of 258°, the power-only (1:0) optimization does not apply any yaw misalignment. However, when loads are considered in the optimization, yaw misalignment angles are applied. This occurs because, although the wind speed deficit no longer overlaps with the downstream rotor plane, the wake-induced TI region still partially overlaps. Consequently, yaw misalignment is applied to steer the increased TI region away from downstream turbines. The difference in lateral extent of the velocity deficit and the TI field is illustrated in Figure 4-2. This observation raises the question of whether the TI modeling in FLORIS is realistic, given that the TI field appears to span more laterally than the velocity deficit.

However, wind tunnel experiments by Linkhan and Buxtion [68] showed that wake width, whether defined by TI or velocity deficit, expands linearly with downstream distance but at different rates. In particular, the wake width based on TI grows faster, resulting in a larger spanwise area than that of the velocity deficit. These findings support the observation that the region of elevated TI can extend farther laterally than the velocity deficit in FLORIS.

The second effect can be explained in two ways. First, when a turbine produces less power, it typically experiences lower loads. Therefore, for the load-only controller (0:1), it is reasonable that the controller follows the wind direction, leading to full wake overlap, reduced power production, and lower DELs. A second explanation is that full wake overlap is preferred over partial overlap. Partial overlap leads to asymmetric loading on the turbine, increasing fatigue and structural imbalances [69].

To investigate the influence of full and partial wake overlap on the tower base (TB) loads, Figure 4-3 presents a case with a constant 270° wind direction, where T0 is yawed ±25°. Figure 4-3b shows the tower base DEL for T0, indicating that for a turbine that does not operate in a wake, any yaw misalignment results in an increase in DEL, which is consistent with the findings by Thedin *et al.* [67]. Figure 4-3a shows the tower base DEL on T1 as a function of the yaw misalignment of T0, while its own yaw misalignment is kept constant at 0°. The figure demonstrates that large yaw misalignment angles of the upstream turbine, which causes partial wake overlap for T1, increases its DELs.

Together, Figure 4-3a and Figure 4-3b demonstrate the fact that when loads are weighted more heavily relative to the power, the LuT tends to follow the baseline controller around the fully aligned wind direction region.

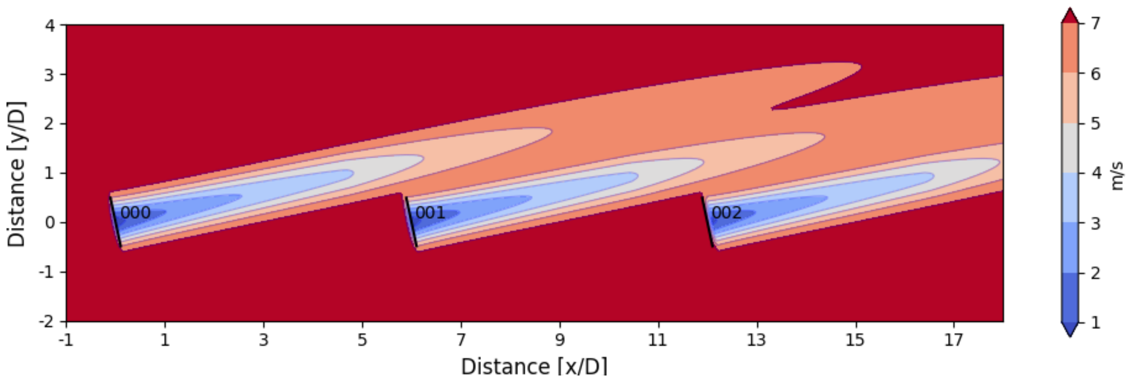

(a) Wind speed field at 258° wind direction. The wake from the upstream turbine does not overlap with the downstream rotor planes.

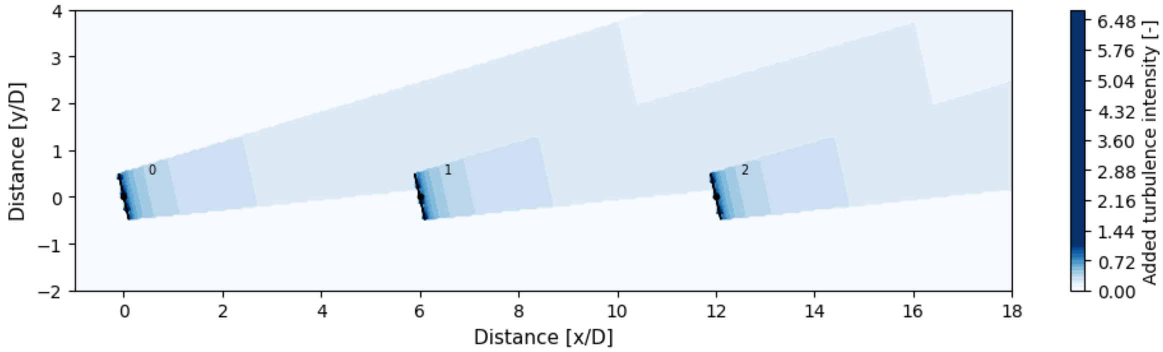

(b) Turbulence intensity field at 258° wind direction. The increased TI region spreads wider and still shows a partial overlap with downstream turbines.

Figure 4-2: Comparison of the wind speed and TI fields at a wind direction of 258°. The TI field exhibits a larger lateral extent than the wind speed deficit, leading to partial overlap with downstream turbines in terms of TI.

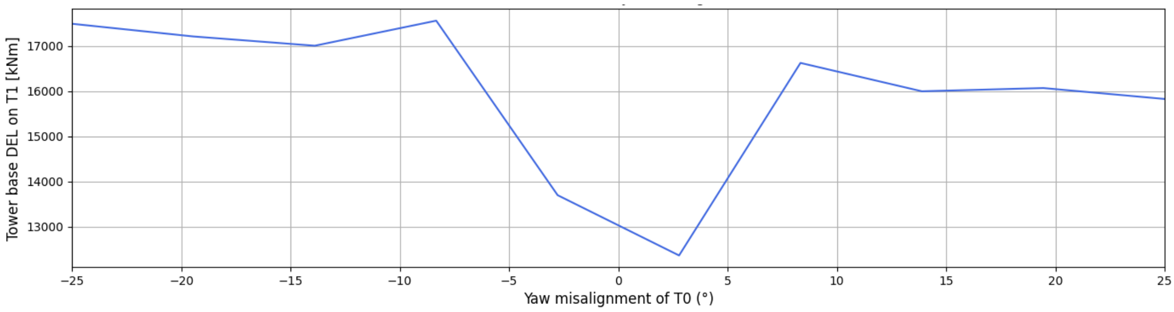

(a) Tower base DEL of Turbine 1 as a function of the yaw misalignment of Turbine 0.

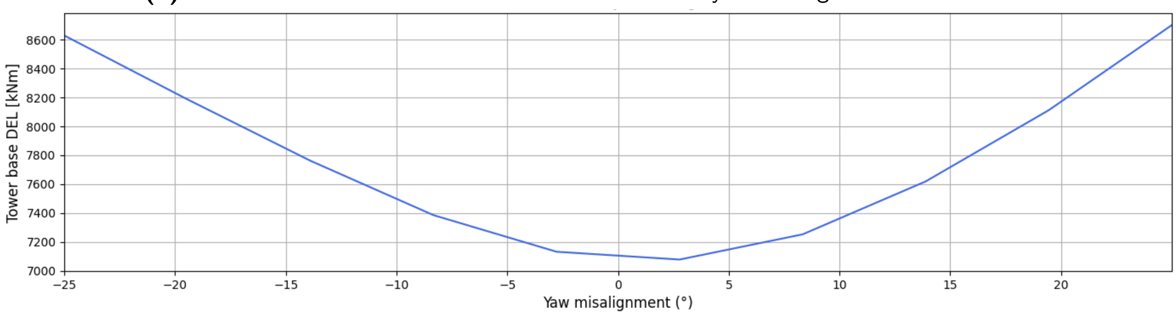

(b) Yaw misalignment versus tower base DEL for Turbine 0.

Figure 4-3: Relation between yaw misalignment and tower base DEL simulated for a $270°$ wind direction. Figure (a) shows the DEL response of T1 as a function of the yaw misalignment angle of T0, illustrating that a full wake overlap is preferred over a partial overlap for the downstream turbine. Figure (b) shows the DEL response of T0 resulting from its own yaw misalignment without wake-induced flow, demonstrating that any yaw misalignment with the incoming wind direction increases the tower base fatigue loading.

4-3 Summary

This chapter introduced the balanced power-load yaw control strategy. First, the LuT-based dead-band yaw controller implemented in OFF was described, including its update logic and required inputs. Next, a methodology for generating LuTs with a balanced power-load objective was presented, in which the tower base was selected as the representative load channel in the objective because it exhibited the largest increase in fatigue loading under wake-induced inflow compared to the other channels.

Sub-questions 2.1 and 2.2 were addressed by demonstrating how different power-load weightings influence the optimal yaw misalignment behavior. When loads are weighted more heavily, the range of wind direction over which wake steering is applied increases because the wake-induced TI region has a greater lateral extent than the velocity deficit. Around the critical 270° wind direction, however, the controller instead aligns with the inflow, similar to the baseline strategy. The analysis of tower base DEL as a function of yaw misalignment further showed that any misalignment increases fatigue loading and that partial wake overlap leads to higher tower base fatigue loads than full wake overlap.

In the next chapter, the developed controller is applied in a case study using both the steady-state model FLORIS and the dynamic model OFF, to evaluate its performance and to assess the influence of time-varying wake dynamics on the resulting power and load predictions.

Chapter 5

Case Study

This chapter addresses Research Question 2 by evaluating the performance of the controllers developed in the previous chapter when applied to the three-turbine reference case shown in Figure 3-3. One of the objectives of this thesis is to determine whether the controllers designed under steady-state conditions maintain their effectiveness in a dynamic flow environment. Therefore, the chapter also compares the controller performance in OFF and FLORIS to assess the influence of dynamic wake behavior on the resulting power and load responses.

The main contributions of this chapter, together with its outline, are as follows:

- Section 5-1 describes the setup for the three-turbine case study, including the considered wind direction time series, ambient conditions, and the tuning of the dead-band yaw controller in OFF.
- Section 5-2 evaluates the performance of the controllers generated with different power-load weightings in terms of power gain and tower base load reduction. Based on these results, it identifies the most suitable power-load balance for further analysis across the three wind direction signals.
- Section 5-4 translates the predicted DELs into a relative tower base lifetime index to assess the impact of different control strategies.
- Section 5-3 compares the behavior of the *power-only* and *balanced controllers* relative to the *baseline controller*.
- Section 5-5 compares the steady-state and dynamic simulations to assess whether the designed controllers remain effective when time-varying wake dynamics are introduced in OFF. This section also analyzes the underlying dynamics that explain differences in predicted power output and load responses between the two modeling frameworks.

Finally, Section 5-6 summarizes the main findings of this chapter.

5-1 Case Study Setup

This section outlines the simulation setup for the three-turbine study case. As described in Section 4-1, four elements have to be provided to the dead-band LuT-based yaw controller in OFF: the wind direction signal $\varphi_f(k)$, the dead-band width φ_{lim}, the integration coefficient k_i, and the LuT f_{lut}. Section 4-2 described how the LuTs were generated for several power-load weighting balances.

For the wind direction signals, the dataset created by Becker *et al.* in [4] was used. They obtained 24-hour wind direction data, recorded by a vertical ZephIR wind LiDAR at the HKN site [70]. To recover the underlying wind direction variations, they processed the signal using a zero-phase, fourth-order Butterworth low-pass filter with a cut-off frequency of 1/600 Hz [71]. This results in a smooth, noise-free signal as shown in Figure 5-1.

From this time series, three segments were selected to use for the simulations to analyze the controllers. A wind direction of 270° is considered the critical wind direction, as this is the direction in which all three turbines are aligned with the incoming flow and the controller switches the sign of yaw misalignment angles. Around this point, the wake steering controllers are actively applied. Therefore, for Segments 2 and 3, the wind direction medians were shifted to 270° to evaluate the controller's performances with realistic wind direction variation and waked conditions. The three resulting segments are shown in more detail in Figure 5-2.

Following [4], a constant ambient wind speed of 8 m/s is assumed, which lies below the turbine's rated wind speed, where wake steering provides the largest potential for power gains. Variations in wind speed are not considered because the incoming wind direction range overlaps with that of a neighboring wind farm near the LiDAR location, which may have influenced the measured wind speeds through wake effects.

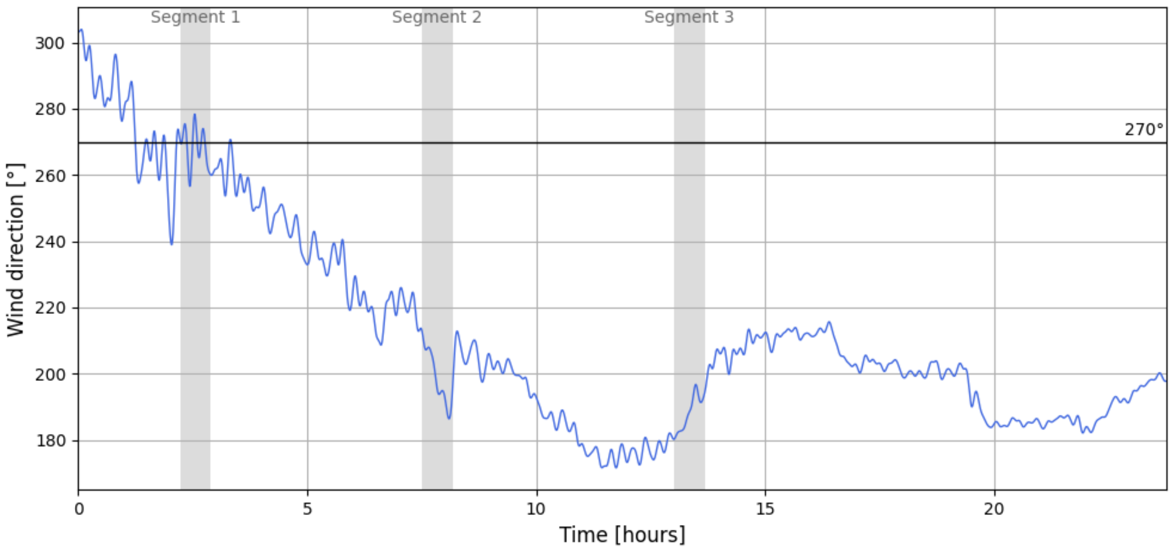

Figure 5-1: Wind direction time series measured by a vertical ZephIR wind LiDAR at the HKN site [70], filtered with a zero-phase, fourth-order Butterworth low-pass filter [71]. The shaded regions indicate the three selected segments to use during simulations to further evaluate the controllers. Segments 2 and 3 are shifted to 270° to evaluate the controller's performance in conditions where wake steering is active.

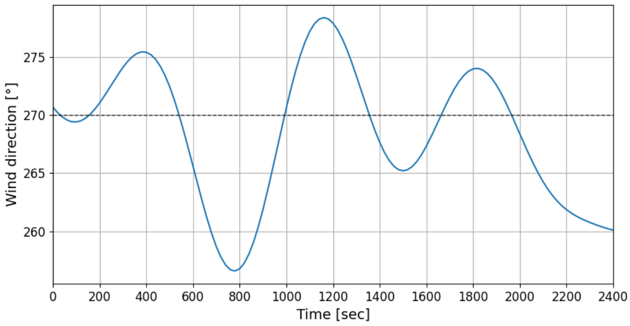

(a) Segment 1

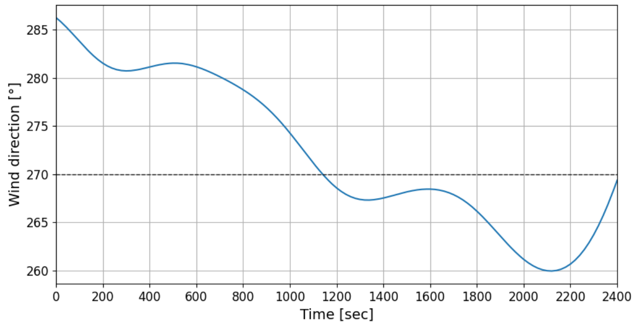

(b) Segment 2

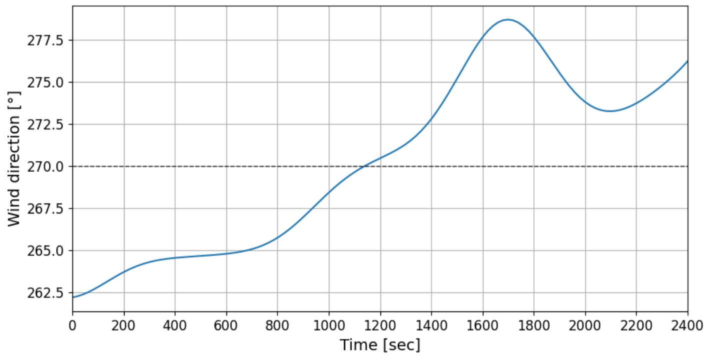

(c) Segment 3

Figure 5-2: The three wind direction segments used to evaluate the controllers, indicated by the shaded regions in Figure 5-1. Segments 2 and 3 where shifted to 270° to evaluate controller performance under waked conditions. Segment 1 contains more wind direction fluctuations with multiple crossings of the critical 270° wind direction, whereas Segments 2 and 3 show smaller variations.

5-1-1 Dead-Band Limit Study

To select an appropriate dead-band width φ_{lim}, a small parameter study was conducted. The integration coefficient was fixed at $k_i = 0.01$, which is considered small and therefore results in relatively few integration-triggered updates of the wind direction estimate, as shown in [4]. This choice isolates the effect of the exceeded dead-band and allows the analysis to focus on a single varying parameter. To illustrate how the dead-band width affects the controller's wind direction estimate $\hat{\varphi}$ in Equation 4-1, Figure 5-3 presents $\hat{\varphi}$ for Segment 1 for dead-band limits of 4° and 2°. The figure clearly shows that with a smaller dead-band of 2°, the controller updates its estimate more frequently, leading to more regular yaw angle updates from the LuT.

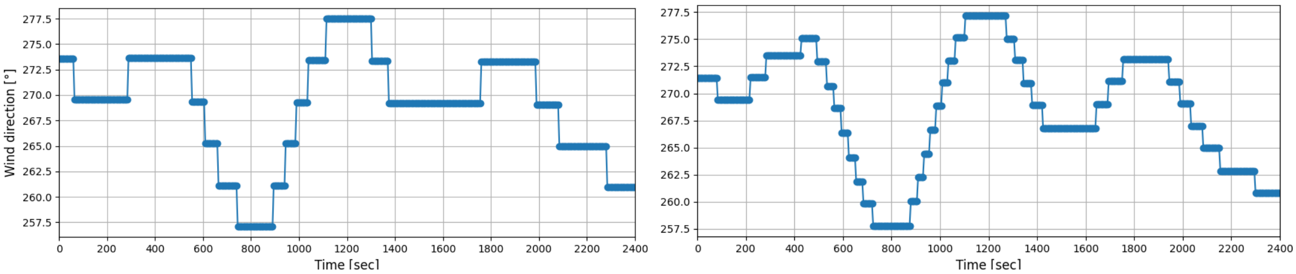

(a) The controller wind direction estimate $\hat{\varphi}$ with a 4° dead-band limit.

(b) The controller wind direction estimate $\hat{\varphi}$ with a 2° dead-band limit.

Figure 5-3: Influence of the dead-band limit on the controller's wind direction estimate $\hat{\varphi}$. A smaller dead-band (b) results in more frequent updates of the estimate, leading to more regular yaw adjustments compared to the 4° limit shown in (a).

This increased update frequency resulted in a power gain of 7.39% for the 2° dead-band, compared to 5.09% for 4° and 5.38% for 3°. However, the 2° dead-band caused 34 yaw activations (one triggered by the integrator), whereas the 3° and 4° dead-band limits resulted in 22 and 17 activations (all direction triggered).

Since minimizing yaw activations or total yaw travel is not the focus, a dead-band of 2° was selected. Nevertheless, it should be mentioned that a higher number of yaw activations leads to a more frequent braking and activating of the yaw mechanism, which in practice contributes to mechanical wear and tear on the system [72]. This study was conducted over a short simulation period, where the wind direction varies significantly and frequently crosses the critical 270 degree wind direction. Therefore, the results may not be fully representative of a realistic 24-hour simulation. In [4], Becker *et al.* conducted a more comprehensive analysis.

For the case study setup, three IEA 3.4 MW [59] turbines were used, aligned in a row with a spacing of six rotor diameters, a TI of 6% and a shear coefficient of 0.2. Based on the DEL sampling time analysis in Subsection 3-2-1, a sampling time of $\Delta t = 5$s is used. This sampling time was chosen, as capturing all load fluctuations is prioritized over computational speed in this case study.

5-2 Control Performance Evaluation

The generated LuTs in FLORIS, as described in Section 4-2, were applied to the three wind direction signals introduced previously. Their performance was first evaluated in FLORIS to verify whether the objective function in Equation 4-2 performs as intended. The analysis focuses on power gain and tower base load reduction relative to the baseline. The results for FLORIS, shown in blue in Figure 5-4, follow the expected trend: increasing the load weighting factor W_L relative to the power weighting factor W_P led to greater load reduction but smaller power gains compared to the baseline.

Next, the transition to the dynamic simulations in OFF was made. For each segment shown in Figure 5-2, an additional 300 s of simulation time was included prior to the segment to ensure that wake steering was already active and the flow field fully developed at the start of each segment. Table 5-1 summarizes all the previously mentioned parameters required for the dead-band LuT-based yaw controller in OFF.

Table 5-1: Simulation parameters in OFF.

Parameter	**Value / Description**
Turbine	IEA 3.4 MW [59]
Wind shear exponent	0.2 (IEC standard)
Wind speed	8 m/s
Turbulence intensity	6%
Dead-band width φ_{lim}	2°
Integration coefficient k_i	0.01
Time step	5 s
DEL sampling time	5 s
Simulation duration	2700 s
Data used for analysis	Last 2400 s

During the simulations in OFF, the results achieved were not as pronounced as those obtained in FLORIS. Figure 5-4 shows, for each segment and for all power-load weightings, the tower base load reduction averaged over the three turbines together with the corresponding power gain relative to the baseline controller. The figure shows that the FLORIS trajectory consistently forms the outermost boundary of achievable performance, with all OFF results remaining inside this range. FLORIS therefore defines the upper bound for both the predicted power gain and load reduction. Part of this behavior comes from the fact that the optimization is performed based on FLORIS, which means that the time-varying dynamics present in OFF are not accounted for in the optimization. Section 5-5 provides a deeper analysis of the origins of these differences.

Although the trend in OFF is not as distinct as in FLORIS, the same overall behavior is observed, allowing a similar optimal weighting to be selected depending on the desired trade-off. Beyond a certain point, it becomes difficult to achieve further load reduction, while the power gain continues to decrease toward the baseline. This behavior is consistent with the earlier observation that heavier load weightings cause the controller to more closely follow the baseline controller around the 270° wind direction.

For further analysis, the power-load weighting of 1:0.8 was selected as the optimal balanced controller, as it prioritizes power maximization while still achieving a significant load reduction. This configuration maintains a primary focus on power production while still achieving a reduction in TB loads, as shown in Figure 5-4. In Segment 2 in particular, this point corresponds with the so-called knee point, the location where the Pareto curve shows the strongest curvature and the trade-off between the two objectives is most balanced. In the remainder of this thesis, this configuration will be referred to as the *balanced controller*. The performance of the *balanced controller* in OFF, in terms of power gain and tower base load change for all segments, is summarized in Figure 5-5, together with the *power-only controller*. To analyze its behavior, it is compared with the *power-only (1:0) controller* and the *baseline* case in the next section.

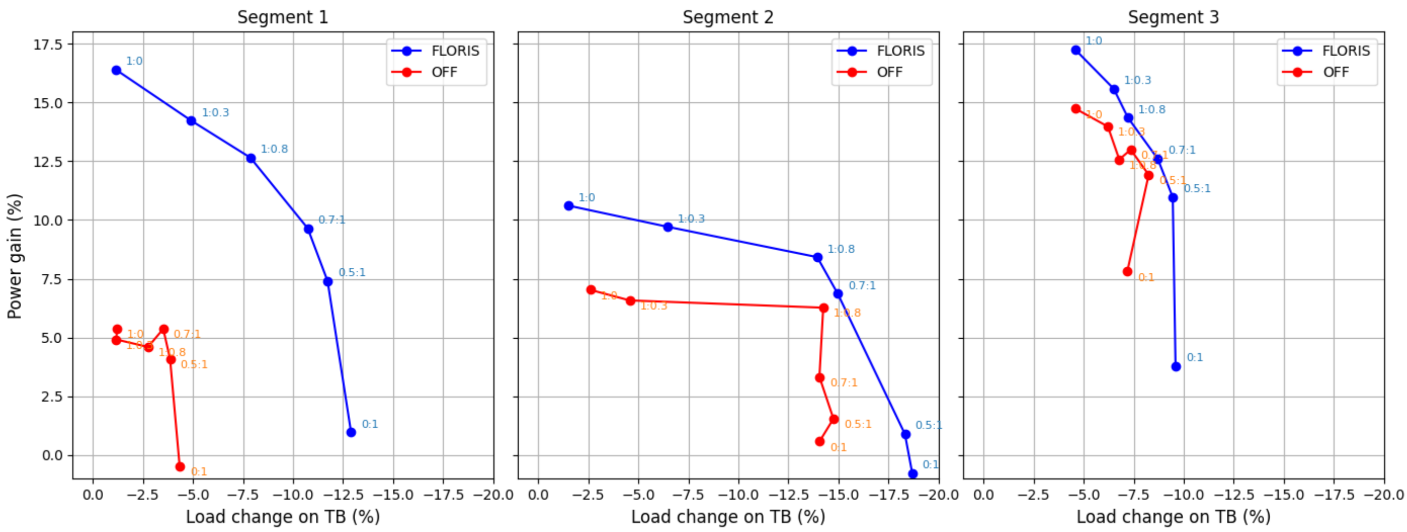

Figure 5-4: Predicted tower base load change, averaged over all three turbines, and power gain for each segment and for all LuTs generated with different power-load weightings, comparing results from FLORIS and OFF. The figure shows that FLORIS consistently forms the upper bound in both predicted power gain and predicted load reduction. The power-load weighting 1:0.8 was selected as the optimal *balanced controller*.

5-3 Controller Performance: Comparison and Discussion

For Segment 2 in OFF, the *balanced controller* achieved a power gain of 6.24% and a TB load reduction of 14.24% compared to the baseline case. This load reduction is distributed among the turbines: T0 experienced a TB load increase of 14.36%, while T1 and T2 showed reductions of 20.50% and 21.86%, respectively.

These results clearly demonstrate the intended behavior of the objective function in Equation 4-2, which aims to achieve a more balanced load distribution across the wind farm. In practice, this allows turbines with a larger available load budget to be used more intensively, while turbines experiencing higher loads are relieved, resulting in a more balanced load distribution across the farm.

To illustrate this load redistribution, the absolute mean DEL values for the *balanced, power-only* and *baseline controllers* in Segment 2 are provided in Table 5-2. The table shows that T0 has a significantly lower mean absolute TB DEL than T1 and T2 in the baseline case, leaving margin for T0 to increase its load contribution under the *balanced controller* while reducing the loads on the other turbines.

This behavior is consistently observed across all segments and controllers. Figure C-1 in Appendix C shows how the results in Figure 5-4 are distributed among the three turbines for all cases in both OFF and FLORIS.

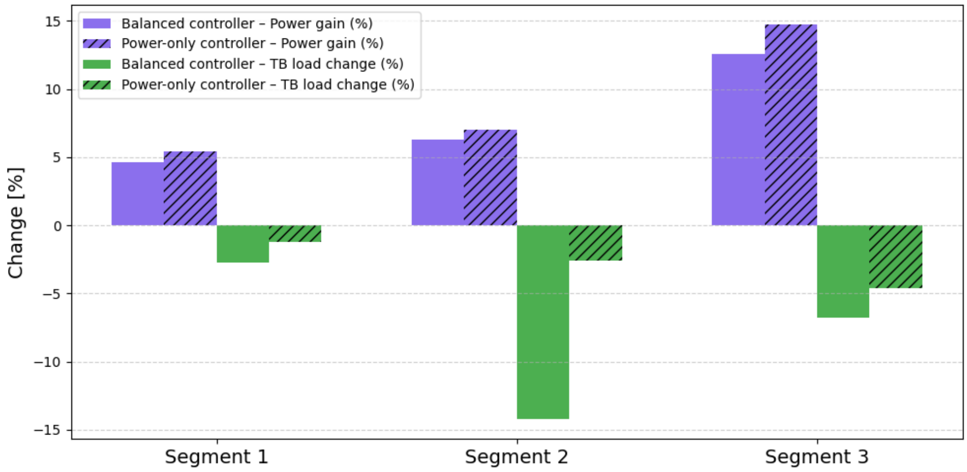

Figure 5-5: Predicted power gain and TB load reduction for the *balanced* and *power-only controllers* across all segments as obtained in OFF. The hatched bars represent the *power-only controller*, showing a higher power gain but smaller TB load reduction, as expected.

Table 5-2: Mean absolute TB DEL values for each turbine and for the total, together with the relative change to the baseline, obtained in OFF for the *power-only* and *balanced controllers* for Segment 2. The results illustrate how T0, which has a larger load budget, experiences an increase in loads, while T1 and T2 show reductions, leading to a more balanced load distribution.

	T0	**T1**	**T2**	**Total**
Baseline controller				
Mean TB DEL [kNm]	7090	14657	14583	12110
Power-only controller				
Mean TB DEL [kNm]	7700	14049	13635	11795
TB load change [%]	**8.60**	**-4.15**	**-6.50**	**-2.60**
Balanced controller				
Mean TB DEL [kNm]	8108	11652	11395	10385
TB load change [%]	**14.36**	**-20.50**	**-21.86**	**-14.24**

Figure 5-6 shows the yaw misalignment trajectories for Segment 2 for the three turbines in OFF under the *balanced* and *power-only controller*. The trajectories clearly illustrate the effect of the dead-band: every time the controller updates its wind direction estimate, the corresponding yaw misalignment angles are adjusted according to the LuT. This results in the sawtooth pattern observed in the curves. The corresponding controller's wind direction estimate can be observed in Figure 5-7.

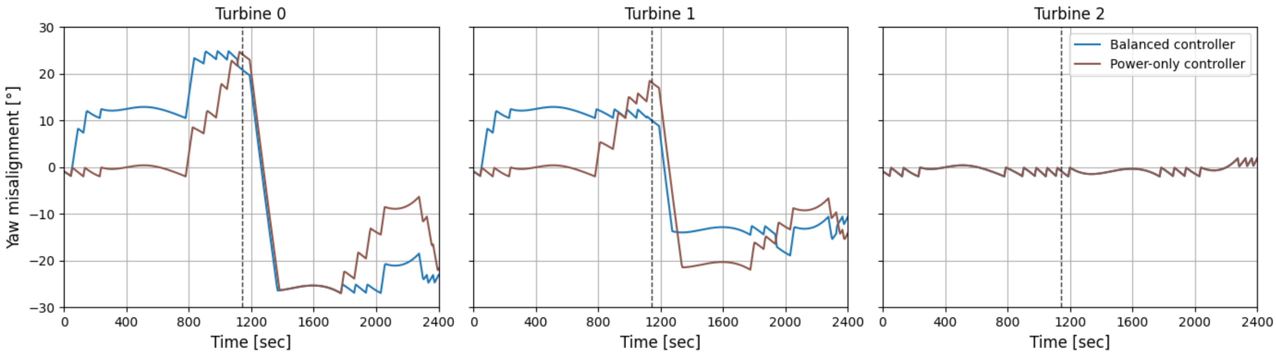

Figure 5-6: Yaw misalignment angles for the three turbines in OFF using the *balanced* and *power-only controller* for Segment 2. The sawtooth pattern results from the dead-band: whenever the controller updates its wind direction estimate, the corresponding yaw misalignment angles are adjusted according to the LuT.

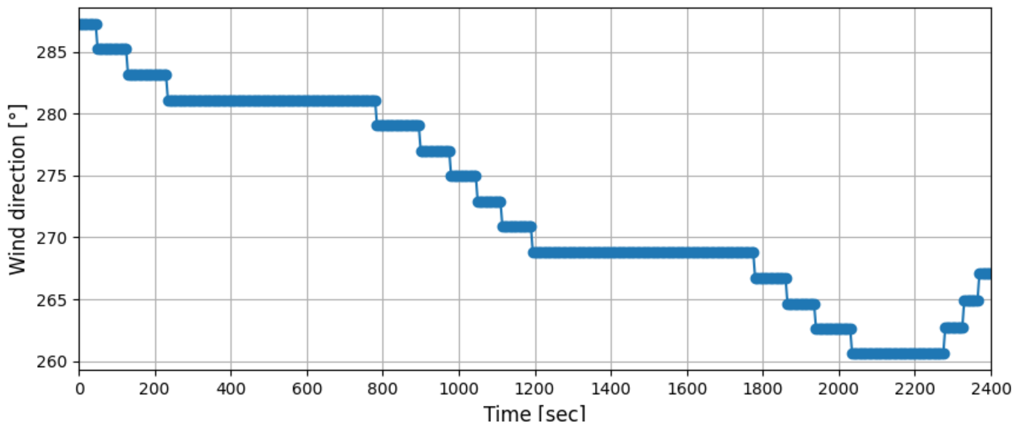

Figure 5-7: Controller wind direction estimate for Segment 2. The estimate shows step-wise behavior due to the dead-band: the controller updates when the deviation, or a small deviation that persists over time, exceeds 2° threshold following Equation 4-1.

The bar chart in Figure 5-5 shows that, for Segment 2, a reduction of only 0.76 percentage points in power gain results in an additional 11.64 percentage points of TB load reduction when using the *balanced controller*.

The generated farm power over time for the simulation of Segment 2 in OFF, comparing the *balanced*, *power-only*, and *baseline controllers*, is shown in Figure 5-8. The *balanced* and *power-only* controllers closely follow one another, with periods where wake steering results in higher power output relative to the *baseline*.

To identify where the load reductions occur compared to the baseline and power-only controller, Figure 5-9 shows the absolute TB DEL output over time for the *balanced*, *power-only*, and *baseline*

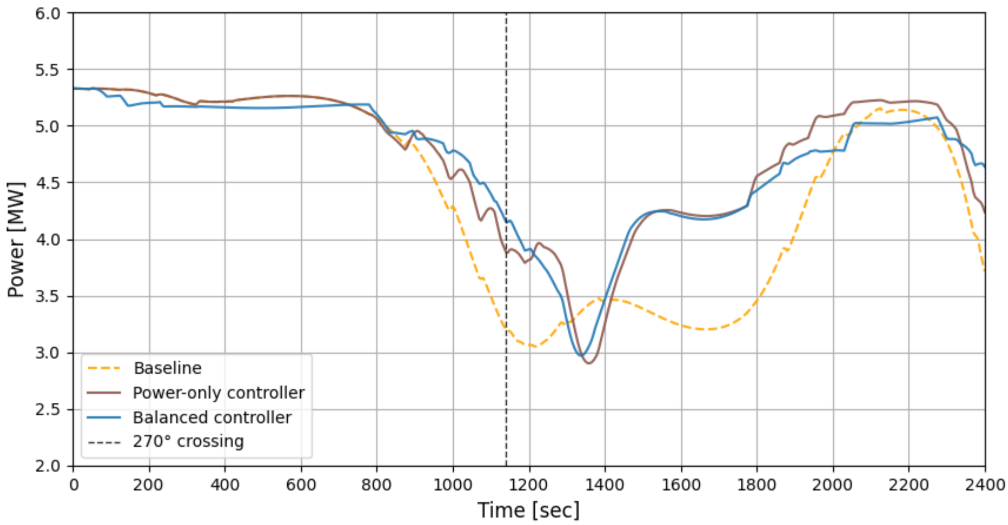

Figure 5-8: Total power generated by all three turbines during the simulation in Segment 2 for the *baseline*, *balanced* and *power-only controllers*.

controllers. The red vertical dashed lines at $t = 600s$ and $t = 2110s$ indicate times when large load reductions occur compared to the *baseline*.

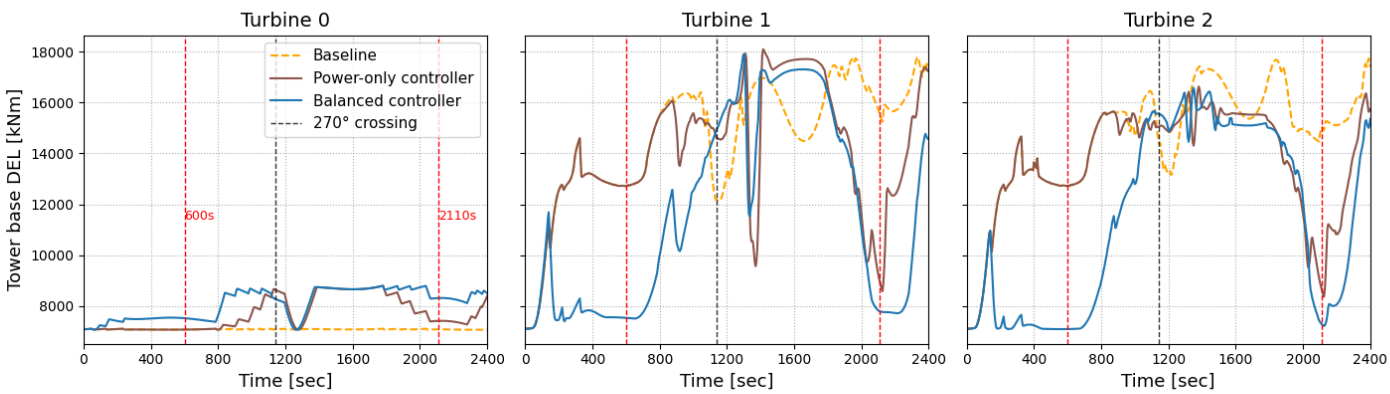

Figure 5-9: Absolute TB DEL over time for the *balanced*, *power-only* and *baseline controllers* in Segment 2. The red vertical dashed lines indicate timestamps at which large load reductions occur and are used for further analysis.

At the time of the first red line ($t = 600s$), the *balanced controller* achieves load reduction compared to both the *power-only* and *baseline controller*. This moment corresponds to a controller estimated wind direction of approximately 281°, as shown in Figure 5-7. As explained in Section 4-2, incorporating loads into the objective function increases the range over which yaw misalignment angles are applied. Consequently, the *power-only controller* follows the *baseline controller* at a wind direction of 281°, whereas the *balanced controller* already introduces yaw misalignment angles of approximately 12° for both T0 and T1, which can also be observed in Figure 5-6 at $t = 600s$. The corresponding flow field snapshots for all three controllers are shown in Figure 5-10. In the *baseline* case, no wake overlap is present in terms of velocity deficit. Consequently, the *power-only controller* does not apply yaw misalignment to increase power production, since power scales with $P \propto U_W^3$. However, as illustrated in Figure 4-2b, the wake-induced TI field spreads farther laterally than the velocity deficit region. For this reason, the *balanced controller* introduces yaw misalignment angles to clear the downstream rotor planes from the elevated TI region.

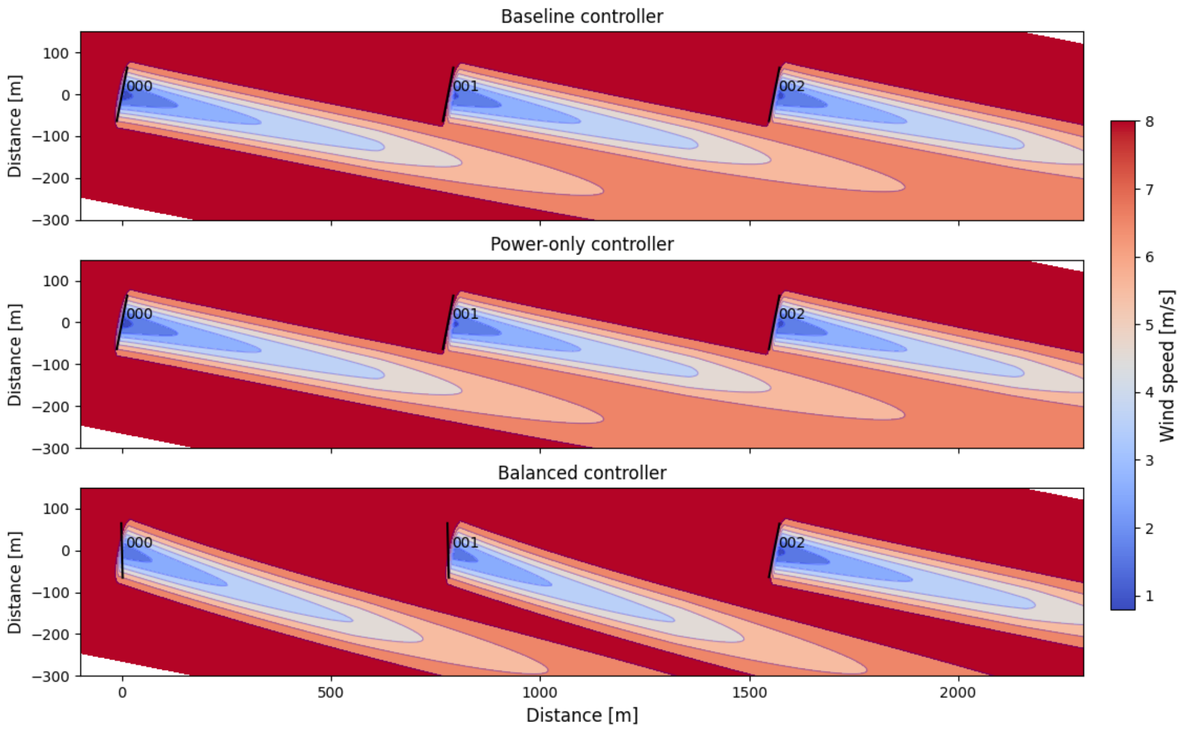

Figure 5-10: Snapshots of the flow field at $t = 600s$ for the *baseline, power-only* and *balanced controllers* in Segment 2. At this moment, turbines T1 and T2 experience substantially lower TB loading under the *balanced controller*. The corresponding wind direction estimate is approximately 281°, at which the *balanced controller*, unlike the *power-only controller*, applies yaw misalignment angles to T0 and T1. This misalignment redirects the wake-induced TI region away from downstream turbines, which spreads farther laterally than the velocity deficit region shown in the figure.

In Figure 5-8, almost no difference in generated power is visible between the *balanced* and *power-only* controller at $t = 600s$. At this moment, the wind direction estimate is approximately 281°, which does not produce wake overlap for the downstream turbines in terms of the velocity deficit field, as shown in Figure 5-10. Because power scales with $P \propto U_W^3$, and none of the rotor planes experience a velocity deficit overlap under any of the controllers, almost no difference in power production occurs. The slight reduction observed for the *balanced controller* is caused by the applied yaw misalignment, which lowers the power production of the turbine. This follows from the dependence of the power coefficient C_P on the yaw misalignment angle through the *cosine-loss* model used in FLORIS.

At the time of the second red vertical dashed line at $t = 2110s$, both the *power-only* and *balanced controller* exhibit a reduction in TB loads relative to the *baseline*, while the difference in total farm power generation remains small for all controllers. This moment corresponds to an estimated wind direction of 261°, as shown in Figure 5-7, where both controllers apply yaw misalignment angles. To further investigate this moment, instant flow field snapshots at this time are shown in Figure 5-11.

For the *baseline controller*, where all turbines are aligned with the inflow direction, turbines T1 and T2 operate under a very small wake-overlap. The *power-only controller* mitigates this by applying yaw misalignment angles of approximately 9° for both T0 and T1. Consequently, its power curve at $t = 2110s$ lies slightly above that of the *baseline*. The *balanced controller*, on the other hand, applies larger yaw misalignment angles, approximately 21° for T0 and 13° for T1, which reduces their own power generation. Figure C-4 in Appendix C shows how the power generation is distributed over all three turbines in OFF, where a power sacrifice for T0 can be observed at $t = 2110s$. This loss in power is not compensated for by the downstream turbines, resulting in slightly lower total farm power compared to the *baseline*.

However, the *balanced controller* applies slightly larger yaw misalignment to fully steer the region of elevated TI away from the downstream turbines. The observed reduction in TB loads for the *balanced controller* relative to the *power-only* controller can therefore be attributed to completely clearing the downstream rotor plane of elevated TI. This effect is illustrated in Figure 5-12, which shows the TI distribution across the rotor plane of T1 for all three controllers. For the *balanced controller*, no overlap in elevated TI is observed; the red region corresponds to the ambient TI of 0.06. The *power-only controller* shows a slight overlap, while the *baseline* exhibits a significant overlap. Additionally, this comparison highlights the influence of TI on TB fatigue loading.

Another observation that supports the trend in TB loading is that just before 1400 s, where the *power-only* and *balanced controllers* show a drop in power production, the TB load for T1 also shows a drop. Around that moment the wake shifts from one side of T1 to the other, bringing the turbine temporarily into full wake overlap. As shown earlier in Figure 4-3a, downstream turbines experience lower fatigue loading under full wake overlap than under partial overlap. Wake steering, however, deliberately redirects the wake from the downstream rotor plane to increase power production. Around the critical 270° wind direction, the controllers therefore balance power gain against increased loading.

5-4 Relative Lifetime Index

To evaluate the effect of the control strategies on structural fatigue, the procedure from [63] is followed. This approach is specifically designed for situations where only instantaneous DEL output is available and design data, such as SN-curves, shape factors, and safety margins, are not.

The load surrogate model provides an instantaneous tower base DEL every 5 seconds. Each DEL represents the 10-minute equivalent load, computed using a reference of 600 cycles, corresponding to a 1 Hz sampling over a 600 s period. To obtain the fatigue damage associated with each 5 s interval, the per-step fatigue damage is computed as

$$d_{TB,jt} = 5DEL_{TB,jt}^{m_{TB}}, \tag{5-1}$$

where $j = 1,2,3$ denotes the turbines, t the time steps, and $m_{TB} = 4$ is the Whöler exponent for the tower base.

Typically, fatigue damage is evaluated using the Miner's rule [73], which expresses the cumulative damage as a fraction of 1, with a value of 1 indicating failure of the component. The calculation

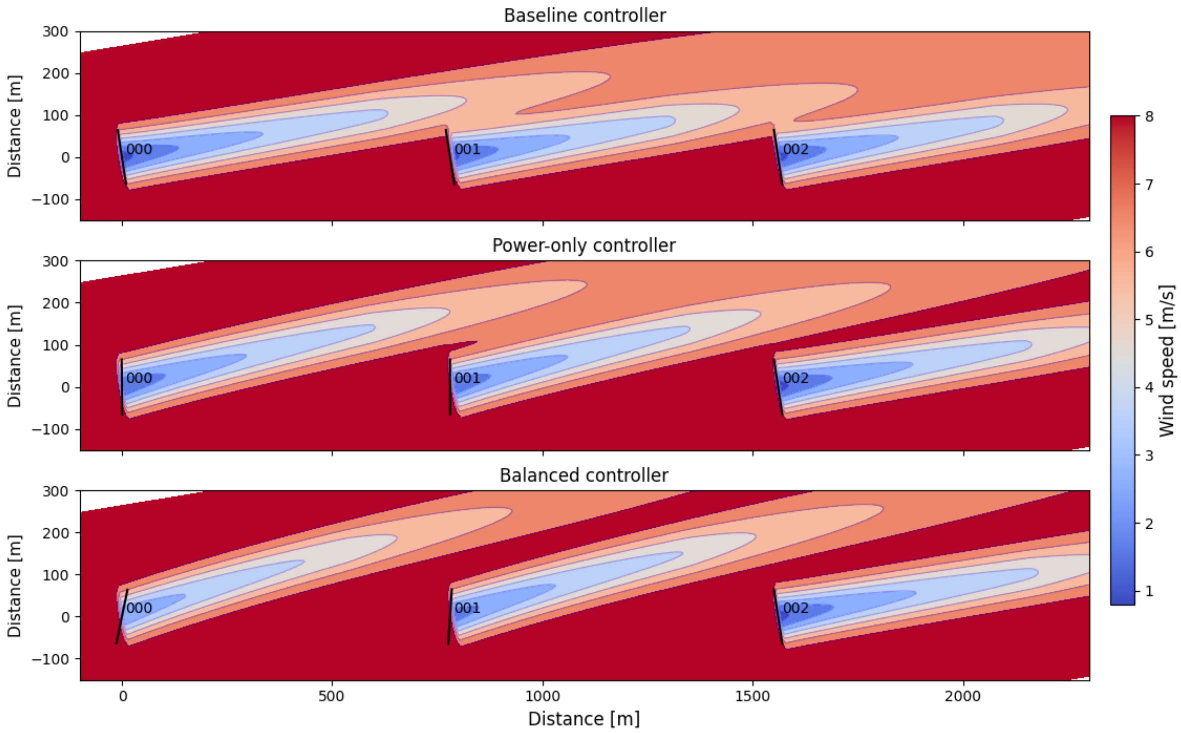

Figure 5-11: Snapshots of the flow field at $t = 2110s$ for the *balanced, power-only* and *baseline controllers* in Segment 2. This moment corresponds to an estimated wind direction of approximately $261°$. The *balanced controller* redirects the wake farther away from the downstream turbines than the *power-only controller*, steering not only the velocity deficit region but also the elevated TI away. As no velocity-deficit overlap occurs in both cases, this reduces their TB loads without sacrificing power.

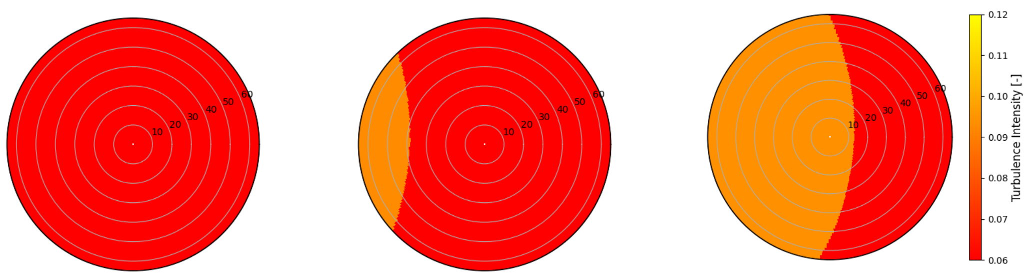

(a) *Balanced* **(b)** *Power-only* **(c)** *Baseline*

Figure 5-12: TI distribution across the rotor plane of T1 at $t = 2110$ s, corresponding to the snapshots in Figure 5-11 for the three controllers. The figure shows that the *power-only controller* redirects most of the elevated TI region away, reducing TB loading compared to the *baseline*, whereas the *balanced controller* completely clears the rotor plane of T1 from elevated TI, further reducing the fatigue loading.

requires the number of cycles to failure for the component, which depends on design specific parameters such as the Safety Factor (SF). However, here these constants from the Miner's rule are omitted, which is allowed when comparing control strategies on the same turbine design.

The cumulative tower base fatigue damage for turbine j over the time series is therefore defined as

$$D_{TB,j} = \sum_t d_{TB,jt}, \tag{5-2}$$

and the corresponding accumulated curves for the three turbines in Segment 2 are shown in Figure 5-13.

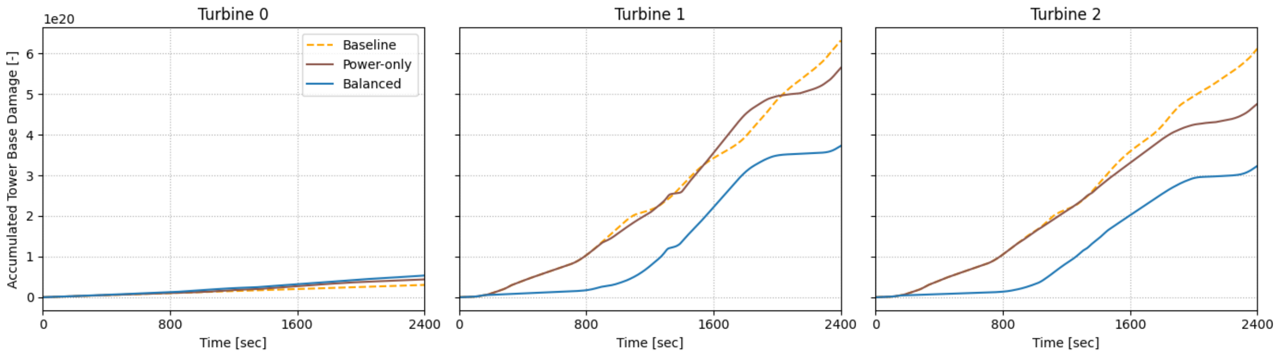

Figure 5-13: Accumulated tower base damage for the three turbines in Segment 2 as obtained from OFF.

To compare control strategies, a fatigue budget is defined as

$$B_{TB}^{greedy} = \max_j D_{TB,j}^{greedy}. \tag{5-3}$$

This is the highest cumulative tower base damage observed in the baseline (greedy) case across all turbines and serves as a design-level normalization constant. This budget depends on specific layout and inflow conditions, making the comparison layout-dependent.

For each control strategy, the normalized fatigue consumption is

$$D_{TB}^{rel} = \frac{D_{TB,j}}{B_{TB}}. \tag{5-4}$$

The relative lifetime index for the tower base, introduced in [63], is then computed as

$$L_{TB,j}^{rel} = (1 - D_{TB,j}^{rel}) + 1. \tag{5-5}$$

The relative lifetime index does not represent an absolute lifetime value. Instead, it serves as an indicator of fatigue consumption for the TB component and should be interpreted qualitatively rather than as a deterministic failure prediction. The metric assumes that differences arise only from the applied control strategy, excluding effects of material variability, installation quality, construction deficits, or other factors that strongly influence the actual lifetime of the components.

The same procedure for computing the relative lifetime indices is applied to the blade root, yaw bearing, and shaft channels, which results in the relative lifetime values shown in Table 5-3, where a value of 1 corresponds to the *baseline*. For the tower base component, T0 shows a decrease of 2%, this is expected as this turbine had a relatively large fatigue load budget in the baseline case. T1 shows a relative lifetime extension of the tower base channel of approximately 11% for the *power-only controller* and 41% for the *balanced controller*. For T2, these values are 21% and 49%, respectively. The relative lifetime values for the tower base in Segments 1 and 3 as obtained in OFF can be found in Appendix D, Table D-1.

The tower base channel was the only component included in the objective function, and its trends and behavior were discussed in detail throughout the thesis. Nevertheless, relative lifetime indices for the other channels are also included in the final results. Summarizing the main observations, the blade root channel shows only small relative lifetime changes, with reductions for T1 and T2. The blade root is particularly sensitive to the sign of its yaw misalignment angle, which determines whether the blades rotate with or against the vertical wind shear [74]. In addition, the yaw bearing channel shows results most similar to those of the tower base, likely because both channels consider the same bending moment orientations, as illustrated in Appendix A, Figures A-1 and A-3. Additional observations and results for the remaining load channels across all segments are provided Appendix D.

It is important to emphasize that these results are based on only 40-minute simulations, during which the wind direction remains close to the critical 270° inflow direction. As shown in Figure 5-1, this is only the case for a short period within the 24-hour LiDAR measurements. The resulting lifetime extensions therefore reflect a worst-case, strongly waked scenario and likely overestimate the values that would result from a realistic 24-hour simulation.

Table 5-3: Relative lifetime indices for the tower base, blade root, yaw bearings, and shaft channels for each turbine in Segment 2, obtained in OFF and computed following the approach in [63]. All values are expressed relative to the baseline case, which corresponds to an index of 1.

Component	Turbine	Power-only controller	Balanced controller
Tower base	T0	0.99	0.98
	T1	1.11	1.41
	T2	1.21	1.49
Blade root	T0	0.97	1.01
	T1	0.92	0.93
	T2	0.95	0.92
Yaw bearings	T0	1.01	1.02
	T1	1.09	1.26
	T2	1.22	1.38
Shaft	T0	1.00	1.00
	T1	0.82	1.08
	T2	1.06	1.25

5-5 Model Performance: Comparison and Discussion

This section investigates the differences between the steady-state simulation in FLORIS and the dynamic simulation in OFF.

Segment 1 is used for this comparison because it exhibits large differences in predicted power gain and load reduction between FLORIS and OFF, which can be seen in Figure 5-4. The *balanced controller* achieves a 12.65% power gain and 7.87% reduction in TB loading relative to the *baseline*, while in OFF the corresponding values are 4.60% and 2.76%, respectively. Segment 1, shown in Figure 5-2a, shows stronger fluctuations and more frequent crossings of the critical 270° wind direction than the other segments. To further understand the behavior in Segment 1, Figure 5-14 illustrates the yaw misalignment angle trajectories of the three turbines during the simulations in FLORIS (in blue) and OFF (in red). It is clearly visible that the turbines in OFF struggle to follow the optimal yaw misalignment angles prescribed by the LuT, where FLORIS can apply these at every timestep.

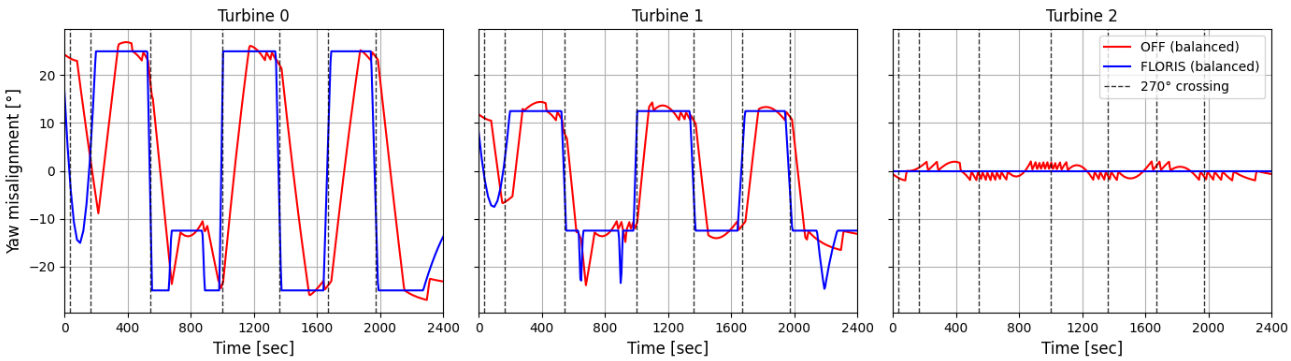

Figure 5-14: Yaw misalignment trajectories for all three turbines in FLORIS and OFF during the simulation in Segment 1 for the *balanced controller*. The dashed vertical lines indicate the timestamps where the wind direction crosses 270°.

Around the 270° wind direction, the optimal yaw misalignment angles switch abruptly from negative to positive values of approximately 25° in order to steer the wake from one side of the downstream turbine to the other. Because FLORIS does not model yaw rate dynamics, it applies a 50° change in yaw misalignment instantaneously. OFF, in contrast, includes realistic yaw rate limitations and therefore applies this adjustment gradually rather than in a single time step. Moreover, because of the dead-band limit, the optimal yaw misalignment angles are not updated at every timestep; the wind direction update behavior of the dead-band is visible in Figure 5-15. Together, these effects cause the turbines in OFF to remain in waked conditions for a longer period during the transition in which the wake shifts from one side to the other, resulting in reduced power production.

Furthermore, the transient flow in OFF causes the impact of yaw adjustments to propagate downstream after some time, by which point the flow field may already have shifted. As a result, the controller continuously lags behind the changing flow conditions. Since Segment 1 crosses the critical 270° wind direction multiple times, the resulting differences in predicted power gain and load reduction between FLORIS and OFF become particularly pronounced.

Figure 5-16 compares the generated farm power over time for the *balanced controller* in Segment 1 for both OFF and FLORIS. In the power curve from FLORIS, the power drops are shorter than those observed in OFF. This behavior is expected, as the yaw misalignment angles are 0° only briefly at this point, placing the downstream turbines in full waked conditions. In OFF, the transition takes longer, resulting in longer lasting drops. The peaks, in contrast, are higher and wider in FLORIS than in OFF. A delay is also visible, as the power drops in FLORIS align exactly with the 270° crossings, whereas in OFF they occur later.

Figure 5-14 has already demonstrated that, in OFF, the yaw misalignment angles lag behind the op-

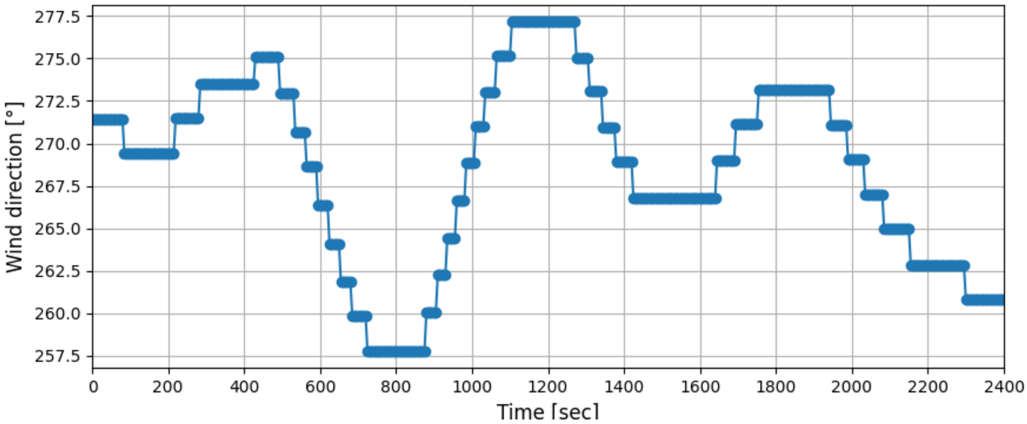

Figure 5-15: Controller estimated wind direction over time for Segment 1. The dead-band limit prevents the estimate from being updated at every timestep.

timal values because of both the yaw-rate limit and the dead-band. OFF also shows a delay in power generation caused by transient wake propagation. Analyzing the 270° crossing around 1000 seconds highlights how wake propagation, together with the yaw-rate limit and the dead-band, introduces a delay in the power response. In OFF, the corresponding power drop appears around 1110 seconds (indicated by the green vertical line in Figure 5-16), approximately 110 seconds later. The delay is consistent with the wake propagation, as the Observation Points (OPs) travel with the ambient wind speed of 8 m/s and the turbines are spaced 6 rotor diameters apart (≈ 780 m).

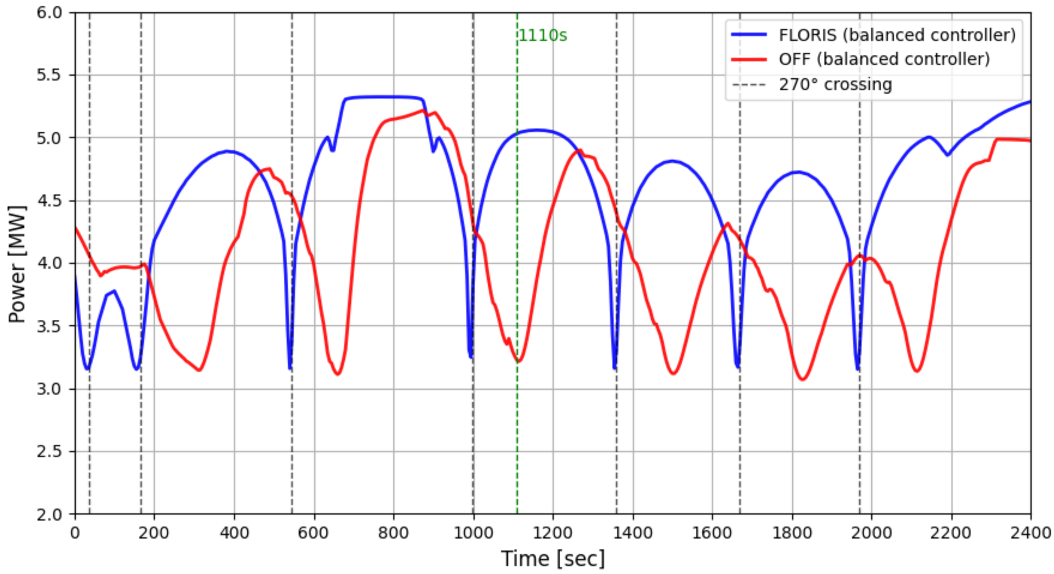

Figure 5-16: Generated farm power for Segment 1 using the *balanced controller* in OFF (red) and FLORIS (blue). The dashed vertical lines mark the moments when the wind direction crosses 270°. The green line indicates a specific timestamp (1110s) used for further analysis.

To analyze this transition more closely, the flow fields in OFF and FLORIS are compared at these three timestamps:

- $t = 980$s, just before the 270° crossing,

- $t = 1010$s, directly after the crossing,
- $t = 1110$s, where OFF shows a power drop while FLORIS is at a peak.

The corresponding flow field snapshots for OFF are shown in Figure 5-17, and those for FLORIS in Figure 5-18.

In OFF the flow field plots appear "tiled" because one tile is generated per turbine. Each tile visualizes a local linearized approximation of the wake that is only valid at the turbine where it is computed. As a result, the plot shows both the wake generated by the upstream turbine and the wake received by the downstream turbine at the same simulation time. This approach is computationally efficient, since these linearized wake fields are already available from the FLORIS turbine evaluations. Between 980 and 1010 seconds, the wind direction crosses 270°, causing the optimal yaw misalignment angles for the *balanced controller* to switch from negative to positive values. In FLORIS, this $\pm$ change in yaw misalignment angles of T0 and T1 is directly visible. However, at $t = 1010s$, the upstream rotor planes in OFF are still negatively yawed, which is also observed in yaw misalignment trajectories in Figure 5-14 at that timestamp.

At $t = 1110s$ in OFF, the upstream turbines are already steering their wakes in the new positive direction, while the downstream turbines still receive the previously generated wake. This delayed wake reaches them frontally at that moment, placing the downstream turbines in full waked conditions. This explains the drop in power and why it occurs some time after the actual 270° crossing. In FLORIS, all turbines operate in free-stream wind flow at $t = 1110s$, which explains why the wind farm experiences a power peak.

However, as shown in Figure 5-1, realistic 24-hour wind direction data do not stay near a single value for a longer period of time. Therefore, this segment is not considered representative of realistic long-term behavior.

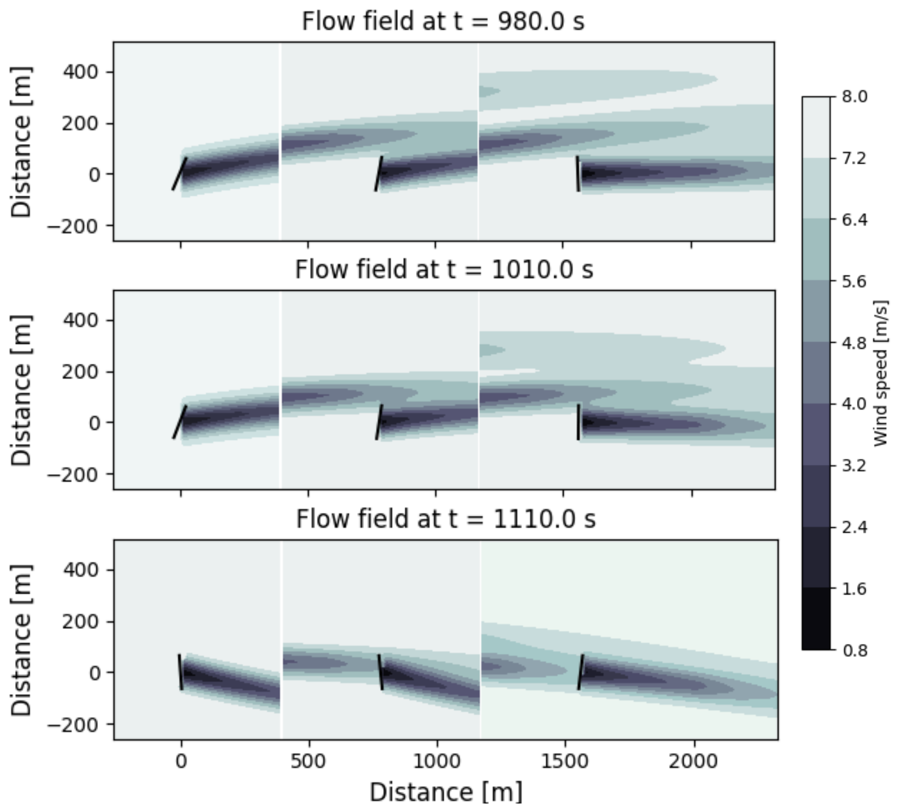

Figure 5-17: Flow field snapshot in OFF at 980, 1010 and 1110 seconds in Segment 1. One tile is created per turbine, each containing a wake field that is only valid at the turbine's location.

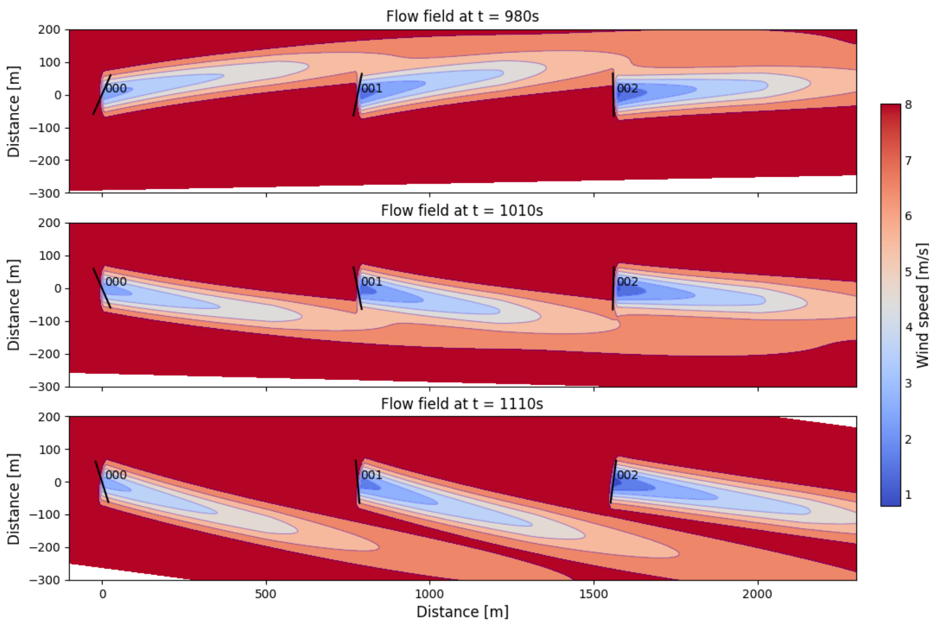

Figure 5-18: Flow field snapshots in FLORIS at 980, 1010 and 1110 seconds in Segment 1, showing the instantaneous application of optimal yaw misalignment.

5-6 Summary

In this chapter, a case study was performed for a three-turbine wind farm in which all building blocks of this thesis were applied in practice: the dynamic flow model OFF with the implemented load surrogate model and the controller. Section 5-1 described the setup used for the case study and summarized the inputs required for the simulation in OFF in Table 5-1, with extra attention given to the dead-band limit and the corresponding trade-off between generated power and yaw activations.

In Section 5-2, all generated controllers with their respective power-load configurations were tested using three different wind direction signals and evaluated in terms of predicted power gain and TB load reduction. This resulted in the Pareto curves shown in Figure 5-4, from which the configuration of 1:0.8 was selected as the optimal balance. This configuration maintains priority on the traditional power gain objective while still achieving load reduction, and was referred to as the *balanced controller*.

For Segment 2, the simulation in OFF using the *balanced controller* achieved a power gain of 6.24% and a TB load reduction of 14.24%, compared to 7.03% and 2.60%, respectively, for the *power-only controller*. The load reduction resulted in a relative tower base lifetime reduction of 2% for T0 and lifetime extensions of 41% and 49% for T1 and T2, respectively. These values reflect only the effect of the change in controller strategy for this specific wind direction signal and wind farm layout.

Section 5-3 addressed Sub-question 2.3 by comparing and discussing the behavior of the *balanced controller* and the *power-only controller*. The analysis showed that much of the load reduction achieved by the *balanced controller* results from applying yaw misalignment to redirect not only the velocity deficit wake away from the downstream rotor plane, but also the wake-induced TI. This is done because the TI field has a larger lateral extent. Steering the elevated TI region away leads to a small power decrease for the yawing turbine but yields a large load reduction for the downstream turbine that is cleared from wake-induced TI. Note that this behavior partially depends on the underlying model assumptions, which is discussed in more detail in the limitations in Subsection 6-3-3.

Subsequently, to answer Sub-question 2.4, the steady-state simulation in FLORIS was compared with the dynamic simulation in OFF for Segment 1. This segment resulted in the largest differences between the two models; FLORIS predicted a power gain and load reduction of 12.65% and 7.87%, respectively, while OFF obtained 4.60% and 2.76%. Segment 1 is characterized by strong wind direction fluctuations, including multiple crossing of 270°. Based on the analysis performed in this section, four reasons were identified that explain the obtained differences in OFF and FLORIS:

1. The yaw rate limit of the turbines, which can be modeled in OFF, prevents rapid changes in yaw misalignment angles.
2. The dead-band limit within the controller in OFF causes the yaw misalignment angles to be updated less frequently.
3. The wake created by an upstream turbine advects downstream, which means that the downstream turbine encounters the impact of the yaw misalignment only after a propagation delay.
4. FLORIS was found to represent the upper bound for achievable power gain and load reduction. This is expected, as the optimization is performed based on FLORIS, which does not model the time-varying dynamics and OP-based propagation present in OFF. As a result, the yaw misalignment angles obtained from the optimization are optimal for the steady-state behavior of FLORIS, but not necessarily for OFF.

Together, these factors explain the lower and delayed power generation observed in OFF. They also clarify why, in Figure 5-4, FLORIS consistently forms the upper bound across all segments and all controllers for both power gain and TB load reduction.

Chapter 6

Conclusion

This chapter begins by repeating the main objective of the thesis and summarizing the main results. Sections 6-2 and 6-3 then reflect on the findings, insights, and limitations associated with the two main research questions. Finally, Section 6-4 provides recommendations for future work.

6-1 Overall Thesis Conclusion

Research Objective

"The objective of this thesis is to develop and evaluate a power-load balanced wake steering control strategy that couples a dynamic flow model with a load surrogate model, aiming to achieve both power gain and load reduction."

The main objective of this thesis has been successfully achieved. The sector-averaged load surrogate model was implemented in OFF, after which the tower base loads were included into a dynamic LuT-based dead-band controller. An objective function was formulated that allows a balance between power production and load change based on a predefined weighting. This controller was evaluated on three different wind direction signals. The resulting *balanced controller* achieved both power gain and TB load reduction relative to the baseline in all segments, as shown in Figure 5-5.

With this, the overall goal of the thesis was met. The process showed several insights and limitations, which are discussed in the following sections for each of the two main research questions.

6-2 Research Question 1

Research Question 1

"What is the role and performance of a load surrogate model when applied within a dynamic wind farm flow modeling framework?"

6-2-1 Result

The sector-averaged load surrogate model was successfully implemented in OFF to predict DELs on individual turbines within a wind farm. The required sector-averaged inflow quantities (SAIQs) were extracted in OFF by creating a rotor sampling plane, after which the effective wind speed could be sampled at all points across the rotor plane. A similar function for the TI was developed as part of this thesis, enabling the extraction of TI at arbitrary coordinates. The rotor plane was then divided into four sectors, and the wind speeds and turbulence intensities within each sector were averaged to compute the SAWS and SATIs, as illustrated in Figure 3-6.

The achieved RMSPE between the surrogate predictions in OFF and the reference DELs from FAST.Farm for all load channel are:

- 2.89% for the blade root,
- 6.60% for the shaft,
- 6.51% for the yaw bearings, and
- 9.50% for the tower base.

Although the accuracy is not yet optimal, the performance gap was substantially reduced during the implementation process, and the resulting surrogate accuracy was considered sufficient for deployment in the case study.

During dynamic simulations, the load surrogate was applied to provide instantaneous DEL estimates at discrete time steps. A sampling time of 5 seconds was selected to prioritize capturing relevant load fluctuations while still maintaining computational efficiency.

6-2-2 Insights

The process of implementing the load surrogate model in OFF gave several important insights. When comparing the SAIQs between OFF and FAST.Farm, the SAWS matched reasonably well, however, the SATIs did not match in both trends and magnitude. This mismatch is primarily caused by differences in the underlying turbulence models. The Crespo-Hernandez model in FLORIS assumes a uniform cross-section, whereas in FAST.Farm the TI formulation depends on the local wind speed, which uses a double-Gaussian formulation. To mitigate this difference, the TI field in FLORIS was normalized using the local wind speed as formulated in Equation 2-16. This reduced the RMSPE for all load channels but not sufficiently for utilization. Finally, the load surrogate model was retrained using SAIQs extracted from OFF as input and the DELs from FAST.Farm as output. The model's performance, shown in Figure 3-11, was sufficient for practical use.

This process showed that simply extracting the required inputs is not sufficient to apply a load surrogate model across different wake models with varying underlying flow models. Therefore, the predicted DELs must be validated, and retraining the surrogate model using data from the framework where the load surrogate model is to be utilized proved to be the most reliable approach.

6-2-3 Limitations

Despite the successful implementation, several limitations remain. The remaining performance gap in the predicted DELs can be caused by the following factors:

- The training data set was reduced from 30.783 to 8.289 cases after excluding curtailment, as this control strategy was outside the scope of this thesis. Since this reduced data set was then split into training and testing subsets, the training data became even smaller. This limits the surrogate's ability to fully learn the mapping between the input and output.
- Retraining the surrogate improves consistency between OFF input and FAST.Farm output but does not remove the underlying differences between the two modeling frameworks.
- Because retraining was performed externally, there was no control over the training procedure. Possible improvements, such as using higher-order neural networks or more advanced architectures, could not be explored.

Overall, the final performance is consistent and reliable enough for the case study and control strategies presented in this thesis. Nevertheless, the limitations discussed should be taken into account when interpreting the results.

6-3 Research Question 2

Research Question 2

"What power-load trade-offs arise when fatigue loads are included in a wake steering control strategy under dynamic flow conditions?"

6-3-1 Result

The overall performance of the *balanced controller* in terms of power gain and load reduction is summarized in Figure 5-5. For Segment 2, the controller reduced the tower base lifetime of T0 by approximately 2% relative to the *baseline*, while extending tower base lifetime of T1 and T2 by 41% and 49% respectively over this 40-minute time series.

A LuT-based control strategy was selected because it can be applied in both steady-state and dynamic simulations, ensuring a fair comparison. The LuTs were generated using an objective function that balances power gain and load reduction using predefined weights. Tower base loads were included because this channel showed the largest increase in fatigue loading under operation in waked conditions, making it a channel where wake steering has the potential to make significant reductions.

The LuTs were evaluated for three wind direction signals centered around 270°, the region in which wake steering is active for this wind farm layout. In FLORIS, the behavior was consistent with expected design trends: increasing the relative load weighting reduced tower base loads at the cost of power gain. Similar trends were observed in OFF, but were less pronounced. Across all wind direction signals and power-load configurations, FLORIS consistently represented the upper bound in both achievable load reduction and power gain. Both the performance of the controllers and the differences between FLORIS and OFF are illustrated in Figure 5-4. The trends and differences are explained in more detail in the subsequent Insights section.

The objective function successfully produced a more balanced load distribution throughout the wind farm by reducing tower base loads on the heavily loaded turbines T1 and T2 and slightly increasing the load on T0, with a higher available fatigue budget in the *baseline* case.

6-3-2 Insights

- Two trends in tower base loading were observed:
    1. Tower base loading is lower in full wake overlap than in partial wake overlap (Figure 4-3a).
    2. Tower base DEL increases when yaw misalignment angles are applied (Figure 4-3b).
- The *balanced controller* achieved TB load reductions compared to the *power-only controller* for the three-turbine setup primarily for two reasons:
    1. **A broader range of wind directions in which yaw misalignment is applied**
    The *power-only controller* introduces yaw misalignment only when the downstream turbines experience a velocity deficit wake. However, because the wake-induced TI extends farther laterally, the downstream turbines may still experience elevated TI overlap in wind direction regions where no velocity-deficit overlap occurs, leading to increased loads. The *balanced controller* steers the TI region away at a small power and load cost for the upstream turbine, while significantly reducing tower base loads downstream.
    2. **The behavior around the critical 270° wind direction**
    In the critical wind direction region, around 270° for the layout in this case study, the turbines are fully aligned with the inflow. Here, the *power-only* controller redirects the wake to maximize power production, resulting in a partial wake overlap that increases tower base loads. The load-aware controllers instead make a trade-off between power gain and load reduction around 270°. The stronger the load weighting, the more the controller favors full wake overlap to reduce TB loading, at the cost of power gain.
- The results from FLORIS formed the upper bound for the predicted power gain and tower base load reductions. This can be explained by several factors:
    1. The LuTs were optimized based on FLORIS, which does not consider the dynamic behavior present in OFF.

2. OFF considers yaw rate limits, which prevent the turbines from following the large yaw misalignment adjustments at each time step.
3. The dead-band in OFF reduces the frequency of yaw angle updates, which means that the turbines do not adopt the optimal yaw misalignment angles at each timestep.
4. Because the wake propagates downstream, the downstream turbines experience the effects of a yaw misalignment only after a delay. By the time this delayed wake reaches them, the wind direction has already shifted from the value that triggered the adjustment. As a result, the controller effectively operates with a delay relative to the evolving inflow conditions.

6-3-3 Limitations

The following limitations were identified when addressing the second research question.

- Part of the predicted load reduction is model dependent and is therefore uncertain. In particular, the Crespo-Hernandez TI model used in FLORIS is highly simplified, and it is questionable whether it correctly represents the lateral spreading of wake-induced TI. Although experiments have shown that the TI formulated wake-width grows faster than the velocity deficit wake [68], assuming an uniform profile is not physically realistic. In reality, wake-induced TI tends to be elevated in the shear layer region and lower near the wake center. This raises questions about the physical accuracy of the TI model. Steady-state models have focused primarily on accurately capturing the velocity deficit, since power production scales with $P \propto U_W^3$ and consequently determines AEP. As a result, low-fidelity models have prioritized advanced velocity deficit models over accurate TI models. However, TI strongly effects fatigue loading, making the accuracy of the TI field particularly important for load mitigation studies. As the use of load surrogate models and their coupling with lower-fidelity models is a continuously growing research topic, the need for more advanced TI formulations within these lower-fidelity frameworks is becoming increasingly evident. Models such as the Ishihara formulation [31], which compute TI in the wake based on a double-Gaussian distribution rather than a uniform profile, would likely provide a more reliable basis to predict fatigue loads.
- The lifetime extension indices computed for the load channels require several important considerations:
  1. The index is a relative metric. It does not provide absolute lifetime values but reflects only the relative change resulting from the use of different control strategies.
  2. The computed lifetime extensions apply to the individual components and not to the turbine as a whole.
  3. The approach is design-dependent and should be interpreted specifically for the present setup and inflow conditions.
  4. The results are based on 40-minutes simulations in which the median of the wind direction is fixed around 270°, causing the downstream turbines to operate in waked conditions. In a realistic 24-hour wind direction time series, this situation would occur only for a small period. The lifetime extensions therefore likely overestimate the gains that would be achieved over longer, more representative simulations.

- The tower base channel showed the highest RMSPE in DEL prediction (Figure 3-11), which may limit the reliability of the absolute predicted DEL values. Moreover, outliers may have led the optimization to select yaw misalignment angles that would not be optimal in reality.
- No validation has been performed in a higher-fidelity model that includes aeroelastic simulations, such as FAST.Farm, which is needed to confirm whether the observed trends in load reduction and power gain hold under more accurate flow descriptions. Ultimately, field experiments at an operating wind farm would be required to fully verify the results.

6-4 Recommendations for Future Work

This thesis focused on the integration of a load surrogate model within a dynamic wind farm simulation and demonstrated how it can be used in a simple control strategy. Future work can take three main directions: improving the implementation and further reducing the performance gap in the predicted loads, validating the results in more realistic and higher-fidelity settings, and exploiting the load surrogate model within more advanced control approaches. The following points provide several concrete recommendations for future work.

- Validation using a higher-fidelity model is recommended to determine whether the designed yaw trajectories lead to similar power and load predictions.
- The simplified Crespo-Hernandez TI formulation, which assumes a uniform cross-sectional distribution, was a limiting factor in this thesis. Implementing more advanced TI models, such as the Ishihara formulation, where TI follows a double-Gaussian shape in the wake, would increase the reliability of load predictions for load-focused wind farm control studies in general.
- The results were based on 40-minute time series around 270° inflow direction, corresponding to a worst-case wake interaction scenario. Performing a longer and more realistic simulation would provide more representative power gain and load reduction results, and consequently indices that more accurately represent the component's relative lifetime over operational timescales.
- Future work could focus on translating the results into metrics that incorporate additional design-specific factors, such as SN-curves, material constants, installation effects, and other structural properties, to make statements about absolute lifetime, maintenance costs, or overall reliability.
- Future work could explore more advanced closed-loop control strategies that explicitly leverage the dynamic behavior present in OFF. Although the current LuT-based controller is applied within a dynamic environment, the LuT itself is generated using steady-state optimization in FLORIS. As a result, the optimization does not account for transient wake development, evolving inflow and operating conditions, or the influence of past system states. A more advanced closed-loop control framework in OFF, such as model-predictive control (MPC) or a controller that incorporates the predicted DELs as feedback signals or constraints to make control decisions, could make more effective use of the load surrogate model. Such approaches can improve robustness to disturbances and modeling inaccuracies, and reduce sensitivity to outliers in the predicted DELs.

- In this thesis, only tower base loads were considered in the objective function. Including additional load channels would enable the controller to achieve reductions for all components or make balanced trade-offs between them, and would offer a more complete view of the structural loading across the turbine.

- Applying the current surrogate model to a larger wind farm case study must be done with caution. The load surrogate was trained on a three-turbine configuration. Therefore, the range of inflow quantities in the training set is limited. Using it for much larger farms would likely result in inaccurate DEL predictions.

Appendix A

Additional Background Information

This appendix provides additional background information. The sector-averaged load surrogate estimates the damage equivalent load (DEL) for the following load channels:

- **Blade root DEL**: blade root in-plane and out-of-plane bending moments.
- **Shaft DEL**: shaft out-of-plane and yaw bending moments.
- **Yaw bearings DEL**: tower top fore-aft and side-side bending moments.
- **Tower base DEL**: tower bottom fore-aft and side-side bending moments.

The corresponding turbine components are shown in Figure A-1. The orientation of the bending moments associated with these channels is illustrated in Figure A-2 and Figure A-3.

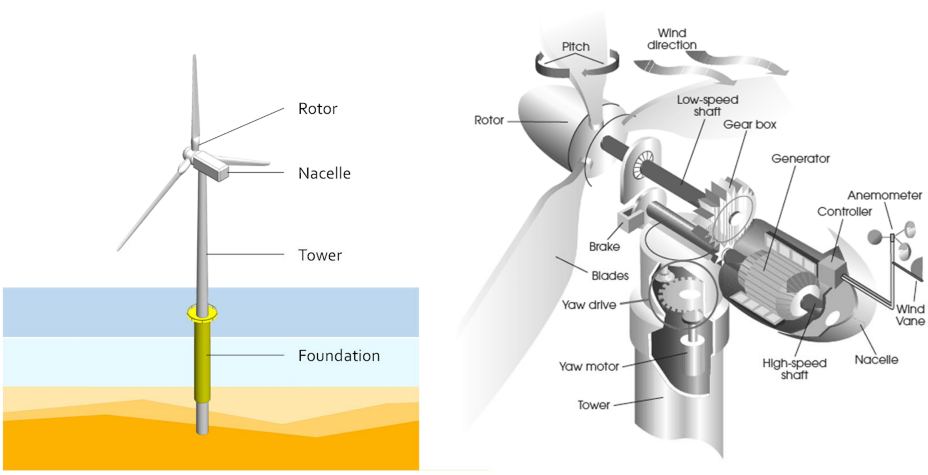

Figure A-1: Structural components of a wind turbine [75].

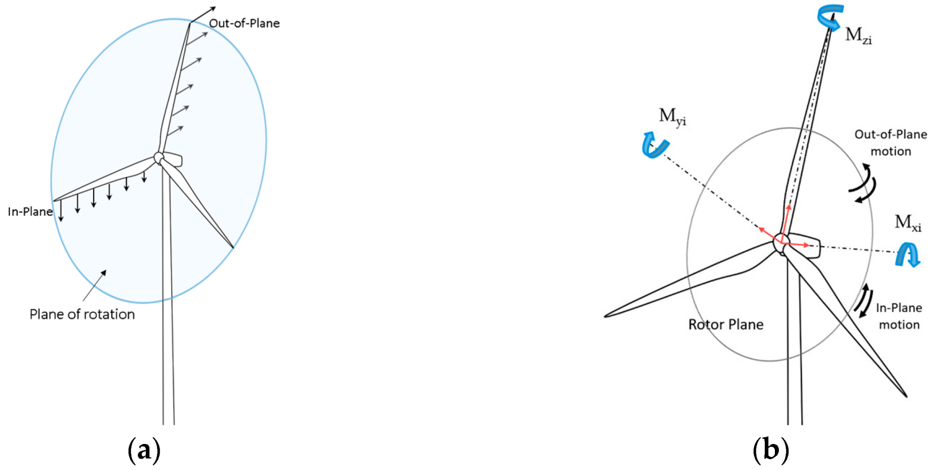

Figure A-2: Bending moments: out-of-plane versus in-plane orientations [76].

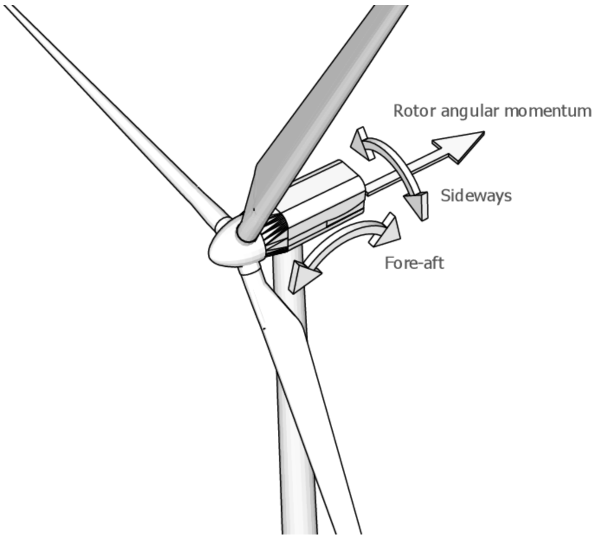

Figure A-3: Fore-aft and side-side tower bending moment orientations [77]

The literature review conducted prior to this thesis included a comparison of existing wind farm flow models, categorized by their level of fidelity. A structured overview of these models is presented in Table A-1.

Table A-1: Overview of wind farm flow model characteristics by fidelity level, with representative model examples.

	Low-Fidelity Models	**Medium-Fidelity Models**	**High-Fidelity Models**
Model examples	FLORIS, PyWake, Frandsen, FOXES	DWM, FLORIDyn, WFSim, PossPOW	SOWFA, UTDWF, SP-wind
Accuracy	Simplified, based on parametric equations, captures general trends but lacks detail	Captures time-dependent dynamics	Detailed turbulent flow representation based on the Navier-Stoke equations
Computational Speed	Fast (order of seconds on a desktop PC [13])	Moderate	Slow (order of days on a cluster of 10^2 CPUs [13])
Steady-State vs Dynamic	Steady-state	Dynamic	Dynamic
Suitability Control	Limited, good for open-loop control	Suitable for online closed-loop control	Too slow for real-time closed-loop control
Strengths	Best for optimization, fast computation	Balance between fidelity and speed. Suited for real-time control	High accuracy for turbulence-resolving, used for verification of other models
Limitations	Possibly oversimplifying interactions, less suitable for closed-loop control	Requires tuning and calibration and larger computational demand	Computationally expensive
Typical use-cases	wake steering, layout optimization	Online closed-loop wake steering	Verification, high-accuracy studies, turbulence flow

Appendix B

Sampling of the Inflow Quantities

Section 3-2 described how the wind speed and turbulence intensity were sampled across the rotor plane. The rotor plane is created and rotated with the yaw misalignment angle. However, when the rotor plane yaws, part of it rotates into its own wake, as illustrated in Figure B-1a. This effect becomes visible when the wind speed is sampled over the rotor plane, shown in Figure B-1b, where a sharp vertical edge appears at the location where the rotor plane intersects with its own wake.

Although the rotor plane rotates, the deflection angle of the wake at the rotor plane remains almost zero in the flow field. As a result, not rotating the rotor sampling plane and placing it several meters upstream avoided the wake intersection. This produced almost identical values for the computed SAWS and SATIs. Nevertheless, to completely eliminate the possibility for the rotor sampling plane to rotate in its wake, a more robust solution is to set the velocity deficit for its own created wake to 0 around the rotor. This modification is visualized in Figure B-2.

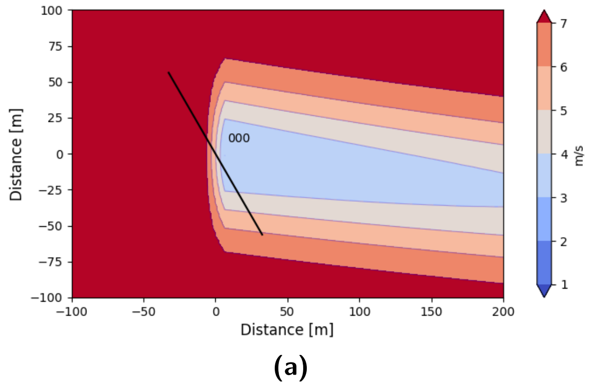

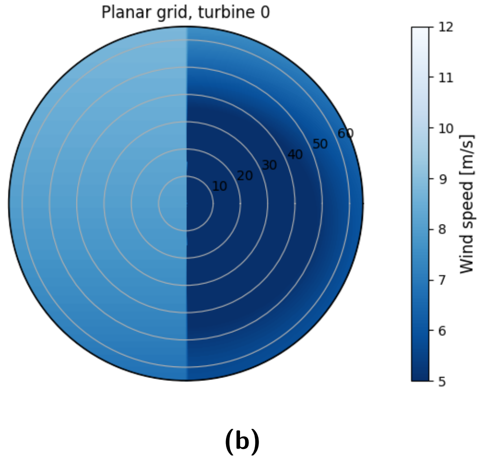

Figure B-1: Rotor plane rotating in its own wake and the wind speed sampled over the corresponding turbine's rotor plane. Figure **(a)** shows the rotor plane with a yaw misalignment angle to partially rotate into its own wake, while Figure **(b)** shows the wind speed sampled over the yawed rotor plane. The sharp vertical edge shows where the rotor intersects its own wake.

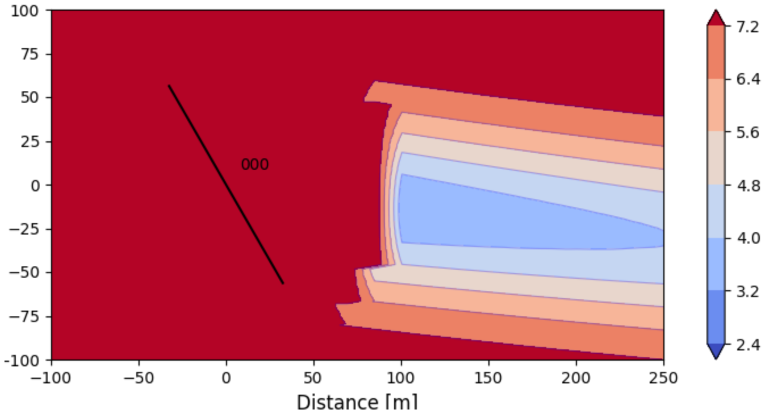

Figure B-2: Rotor plane with a yaw misalignment angle after removing the rotor's own created wake by setting the local velocity deficit to zero within a small spherical region around the rotor.

Appendix C

Additional Controller Performance

The Pareto plot in Figure 5-4 presents the predicted power gain and tower base load reduction, averaged over the three turbines, for all power-load controllers across the three segments. This averaged result can be decomposed into the individual tower base load contributions of each turbine, as shown in Figure C-1. Similar to the total farm results, FLORIS (dashed line) again provides the upper bound on the predicted power gain compared to OFF (solid line). The figure also clearly illustrates the intention behind the objective function, which was designed to achieve a more balanced load distribution across the wind farm. In practice, this led to T0, having the highest available load budget in the *baseline* case, increasing its tower base loading, allowing T1 and T2 to reduce their fatigue loading.

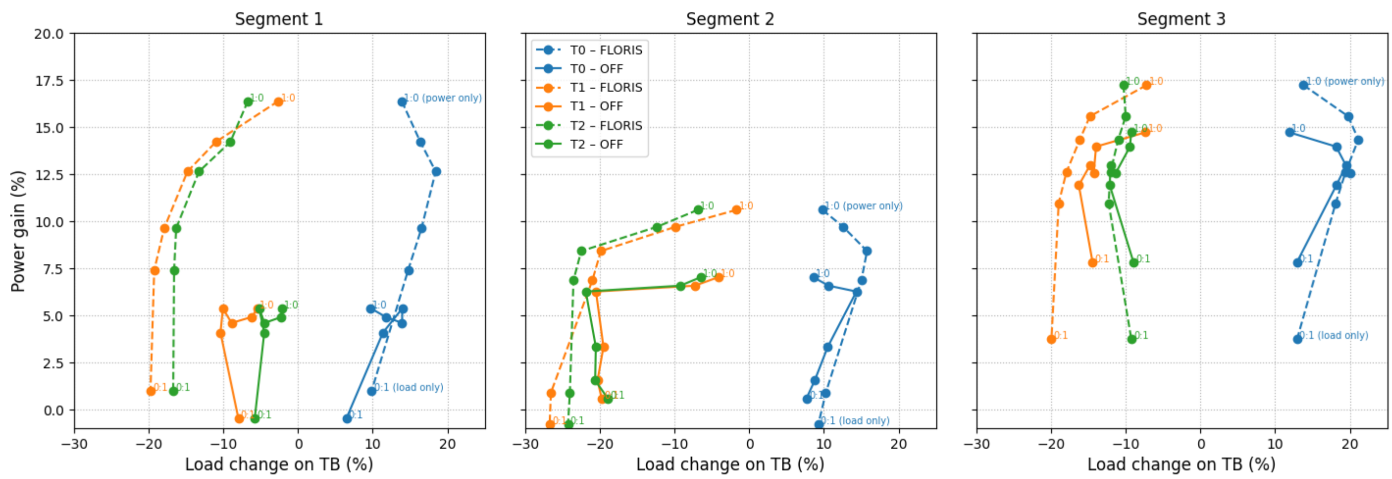

Figure C-1: Tower base load change distributed across the three turbines for all power-load controllers across the three segments, comparing results from FLORIS (dashed line) and OFF (solid line). The figure illustrates how turbine T0 sacrifices part of its tower base load budget to reduce the loads on downstream turbines T1 and T2.

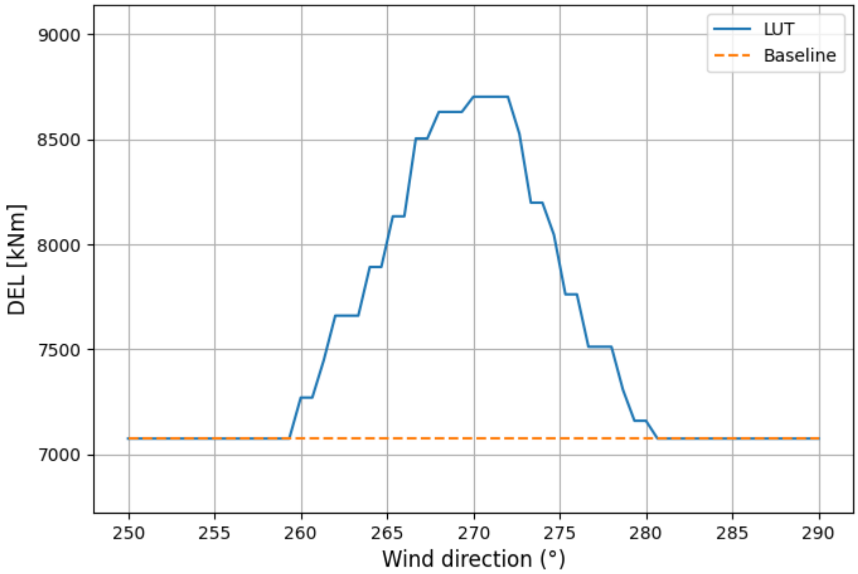

Figure C-2: Tower base DEL output for turbine T0, which operates without wake influence in the three-turbine setup. Under aligned inflow conditions, the yaw misalignment introduced by the LuT controller increases tower base loads compared to the *baseline controller*.

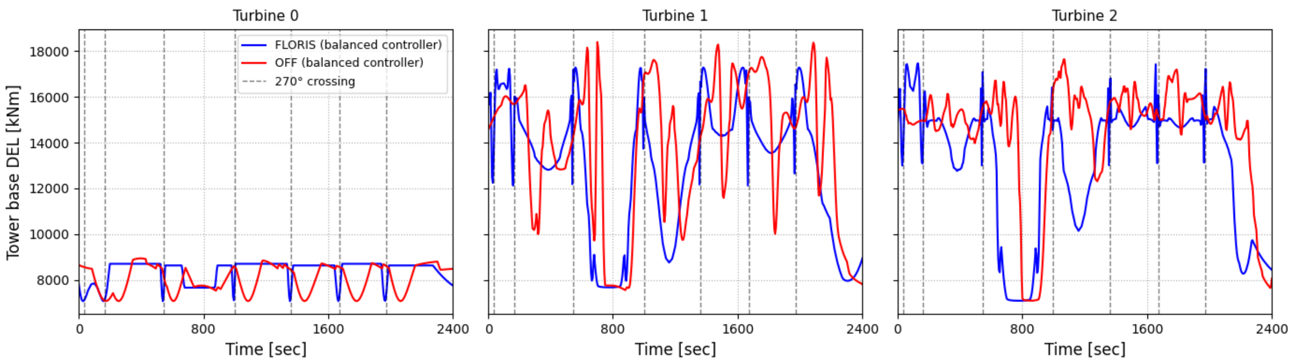

Figure C-3: TB DEL output for Segment 1 under the *balanced controller* for the three turbines in OFF (red) and FLORIS (blue), corresponding to the analysis in Section 5-5 comparing the two models. The peaks and drops follow broadly similar trends, though OFF exhibits a delay, consistent with the factors discussed in Section 5-5.

Section 5-3 provided a detailed comparison of the controllers in Segment 2, with Figure 5-8 showing the total farm power for the *balanced, power-only* and *balanced controllers*. Figure C-4 presents the corresponding power output per turbine. The red dashed vertical line marks $t = 2110$ s, a moment where both wake steering controllers achieve a substantial load reduction, with the *balanced controller* achieving slightly more. At this time, the *power-only* controller applies a misalignment for T0 and T1. This results in a small power loss for the yawing turbines, but redirects the wakes from downstream turbines, increasing their power production and reducing TB loading on T1 and T2. The *balanced controller* applies a slightly larger misalignment for T0, which leads to a slightly lower power output for T0, visible as the blue line slightly below the brown line in the T0 plot, but achieves an additional reduction in TB loading for downstream turbines.

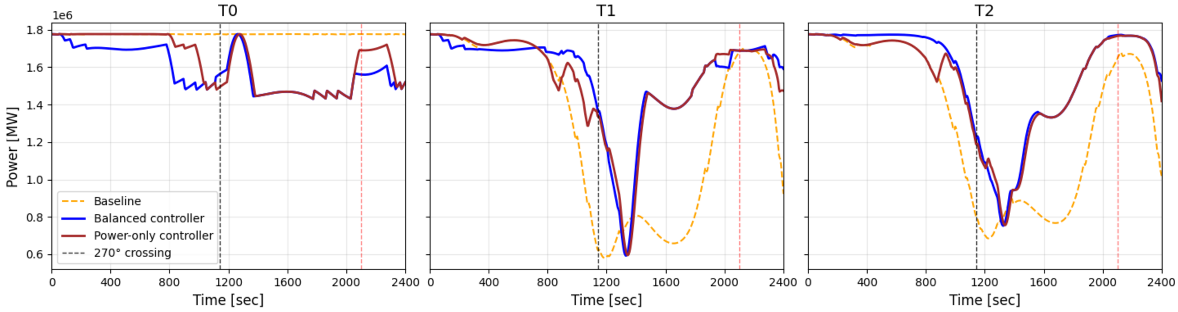

Figure C-4: Power generation per turbine in OFF for Segment 2. The red dashed line marks $t = 2110s$, the timestamp examined in more detail in Section 5-3. At this moment, the *balanced controller* applies a slightly larger yaw misalignment angle to T0 than the *power-only controller*, resulting in lower power production under the *balanced controller*. This is visible for T0, where the blue line lies slightly below the brown line.

Yaw Travel

Since yaw motion contributes to mechanical wear and fatigue of the yaw mechanism [72], it is relevant to compare the yaw travel of the *balanced controller* with that of the *power-only controller* and the *baseline*. The yaw travel was calculated in degrees, based on the nacelle orientation of each turbine. Figure C-5 shows the nacelle orientation exhibited under both controllers for Segment 2. It can be observed that the *power-only* controller results in larger nacelle travel for T0 and T1. Since T2 is restricted from applying yaw misalignment, its orientation follows the wind direction estimate for all controllers.

Across all segments, both wake steering controllers resulted in an increase in total yaw travel compared to the baseline. However, the *balanced controller* resulted in lower total yaw travel than the *power-only* controller. The yaw travel values across all segments and controllers are summarized in Table C-1.

Table C-1: Wake steering increases total yaw travel relative to the *baseline*. The *balanced controller* showed a smaller increase in yaw travel than the *power-only controller*.

Segment	Baseline [°]	Balanced [°]	Power-only [°]	Increase vs. Baseline [%]
Segment 1	220.55	592.54	675.26	+169 / +206
Segment 2	99.33	213.17	274.88	+115 / +177
Segment 3	63.84	121.56	193.65	+90 / +203

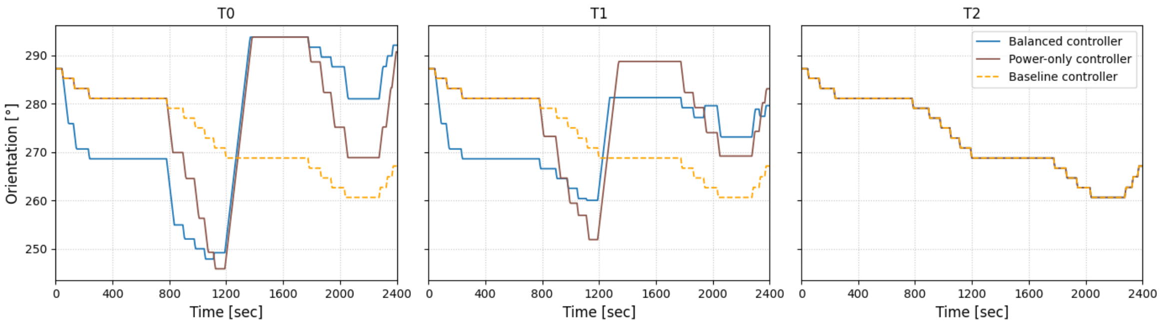

Figure C-5: Nacelle orientation of the turbines for the *balanced*, *power-only* and *baseline controllers*. The *power-only controller* results in the larger yaw travel in degrees than the *balanced controller*.

Appendix D

Response of the Remaining Load Channels

In this thesis, only the tower base load channel was included in the objective function. However, the sector-averaged load surrogate model also provides DEL output on the blade root, shaft and yaw bearing channels. The response of these additional channels was not used in the optimization and their behavior was not further analyzed in this thesis. Figures D-1, D-2, and D-3 show their responses for Segments 1, 2, and 3, respectively, in OFF. The results are presented as boxplots that display the 90th-percentile range: the vertical lines indicate the spread, the orange horizontal line marks the median, and the dashed line shows the mean.

Although their behavior is not analyzed in detail, several observations can be made. For Segment 1, the relative changes in the mean DEL for all channels remain small, similar to the results observed for the tower base channel. As described in Section 5-5, this is mainly due to the wind direction trajectory in Segment 1, which contains large fluctuations and frequent crossings of the critical 270° direction, where all three turbines are aligned with the inflow direction and the applied yaw misalignment angle changes sign.

The blade root channel shows a clear trend: it is less sensitive to wake-induced flow conditions but exhibits strong response to its own direction of yaw misalignment angle. In the process of this thesis, it was observed that the blade root preferred positive yaw misalignment angles. This trend is also supported in literature [78]. Blade root fatigue loads are strongly influenced by vertical wind shear. The yaw misalignment direction determines whether the blades rotate with or against this shear, which reduces or increases the loading, respectively [74]. This is also observed in the figures, where turbine T0 shows the largest range in experienced DELs compared to the other channels. Across all Segments, however, the yaw misalignment angles switch between positive and negative angles due to the wind direction crossing of 270°, causing the mean to stay close to a relative value of 0.

Finally, the yaw bearing channel shows a mean load reduction most similar to that of the tower base channel. This is likely because both channels consider the same bending moment orientations and therefore exhibit similar trends under wake-induced flow and yaw misalignment angles.

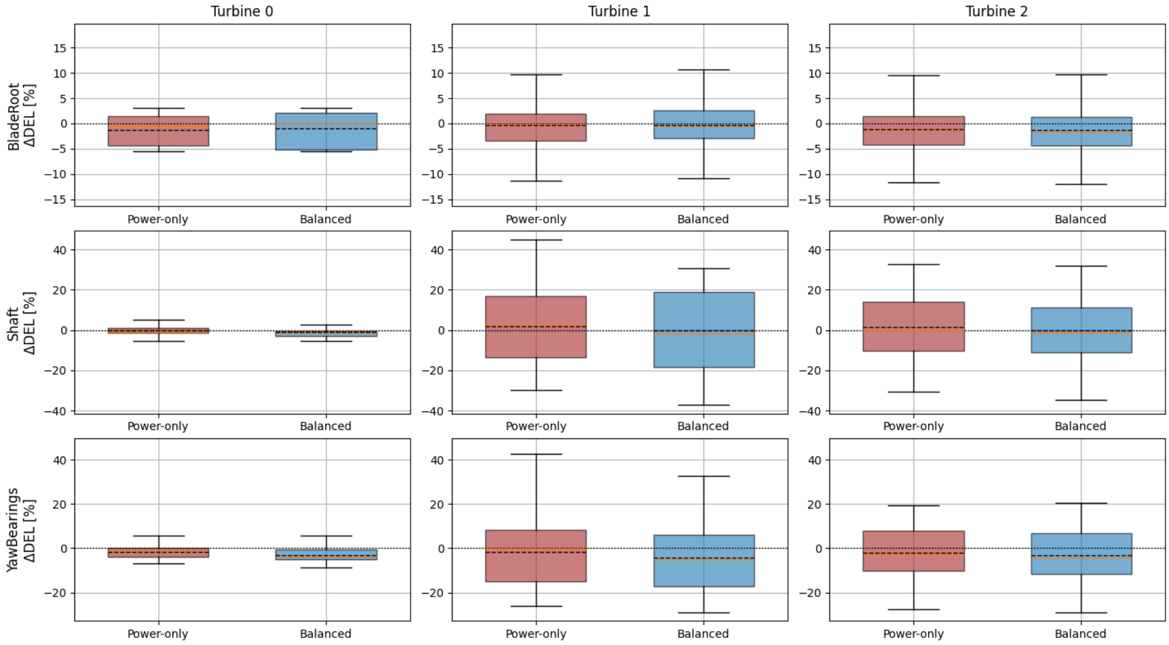

Figure D-1: DEL change for the remaining load channels for Segment 1 in OFF, comparing the *power-only* and *balanced controllers* relative to the *baseline*.

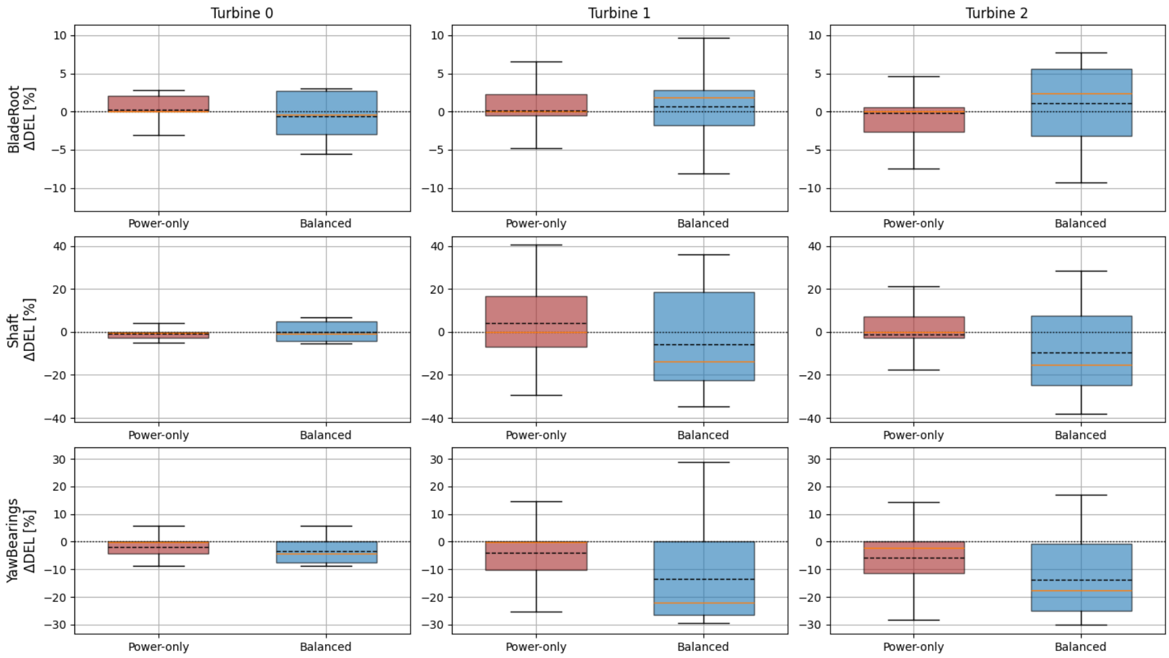

Figure D-2: DEL change for the remaining load channels for Segment 2 in OFF, comparing the *power-only* and *balanced controllers* relative to the *baseline*.

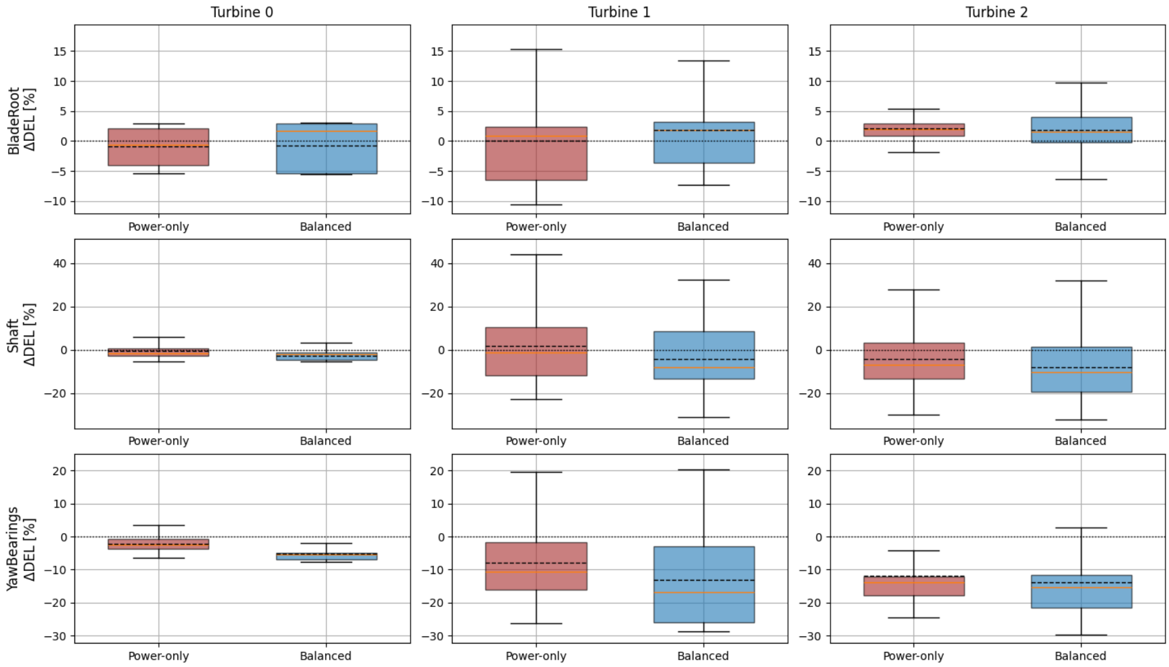

Figure D-3: DEL change for the remaining load channels for Segment 3 in OFF, comparing the *power-only* and *balanced controllers* relative to the *baseline*.

D-0-1 Relative Lifetime Indices

Section 5-4 presented the relative lifetime indices for all load channels for Segment 2 in OFF. These indices are used to illustrate the effect of applying different control strategies relative to the *baseline*. This section shows the relative lifetime indices obtained for the remaining segments in OFF, without further analysis. Table D-1 summarizes the resulting values.

Table D-1: Relative lifetime indices for the tower base, blade root, yaw bearings, and shaft channels for each turbine, obtained in OFF and computed following the approach in [63]. Results are shown for Segment 1 and Segment 3. All values are expressed relative to the baseline case, which corresponds to an index of 1.

Component	Turbine	Segment 1		Segment 3	
		Power-only	Balanced	Power-only	Balanced
Tower base	T0	0.99	0.98	0.99	0.98
	T1	1.13	1.19	1.25	1.41
	T2	1.04	1.07	1.26	1.27
Blade root	T0	1.07	1.04	1.03	1.01
	T1	1.06	1.10	1.10	0.96
	T2	1.15	1.16	0.83	0.90
Yaw bearings	T0	1.01	1.01	1.01	1.02
	T1	1.02	1.07	1.14	1.21
	T2	1.07	1.08	1.39	1.42
Shaft	T0	1.00	1.00	1.00	1.01
	T1	0.94	0.98	1.00	1.10
	T2	0.98	1.02	1.18	1.29

Appendix E

Results for Segment 3

Segments 1 and 2 were analyzed in detail in this thesis. This Appendix chapter presents selected results for Segment 3, with a few brief observations. For Segment 3, the *balanced controller* in OFF achieved a power gain of 12.57% and a load reduction of 6.78% relative to the *baseline*. The difference compared to the *power-only controller*, which achieved 14.73% power gain and 4.59% load reduction, is small in this segment.

Figure E-1 shows the predicted farm power for all three controllers obtained in OFF for Segment 3.

Figure E-2 shows the instantaneous TB DEL output across all turbines. Turbine T1 exhibits a drop in TB loading after the 270° wind direction crossing. This corresponds to the moment when the wake transitions from one side of T1 to the other, bringing the turbine temporarily into full wake overlap. Under the *power-only controller*, this load drop occurs slightly earlier than under the *balanced controller*. In Figure E-3, the yaw misalignment angle of T0 switches from negative to positive earlier for the *power-only controller*. Because the wake is directed to the other side sooner, T1 experiences full wake overlap earlier, resulting in the earlier drop in TB loading.

Between approximately 1600 and 2000 seconds, both controllers achieve a load reduction with almost no difference in generated power compared to the baseline. This period corresponds to a controller wind direction estimate of around 278° (see Figure E-4). During this period, both controllers apply yaw misalignment to T0 and T1 (see Figure E-3) to clear the downstream turbines from wake overlap. The *balanced controller*, however, applies a slightly larger yaw misalignment, to clear the downstream rotor planes not only from velocity deficit but also from the elevated TI region, which has a larger spanwise wake-width. This behavior is similar to what was observed in Segment 2 at $t = 2110s$ and is discussed in more detail in Section 5-3, with additional support from Figure 5-11.

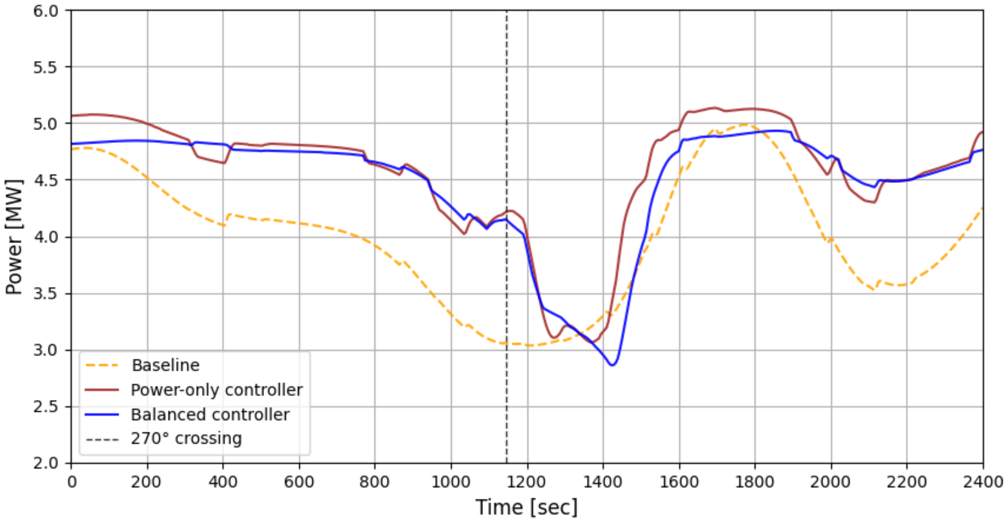

Figure E-1: Predicted generated farm power in Segment 3 for the *power-only*, *balanced*, and *baseline controllers* in OFF.

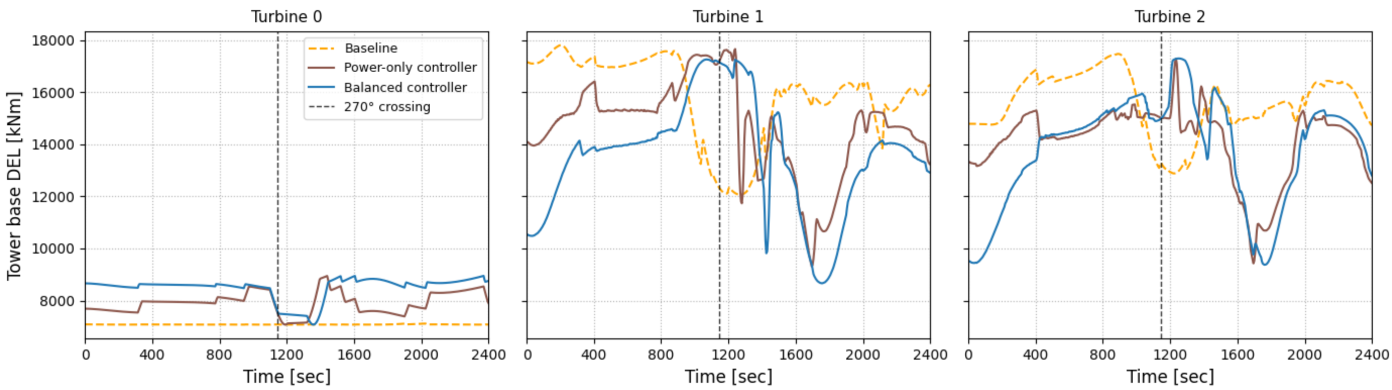

Figure E-2: Instant TB DEL output for Segment 3 in OFF for the *power-only*, *balanced*, and *baseline controllers*.

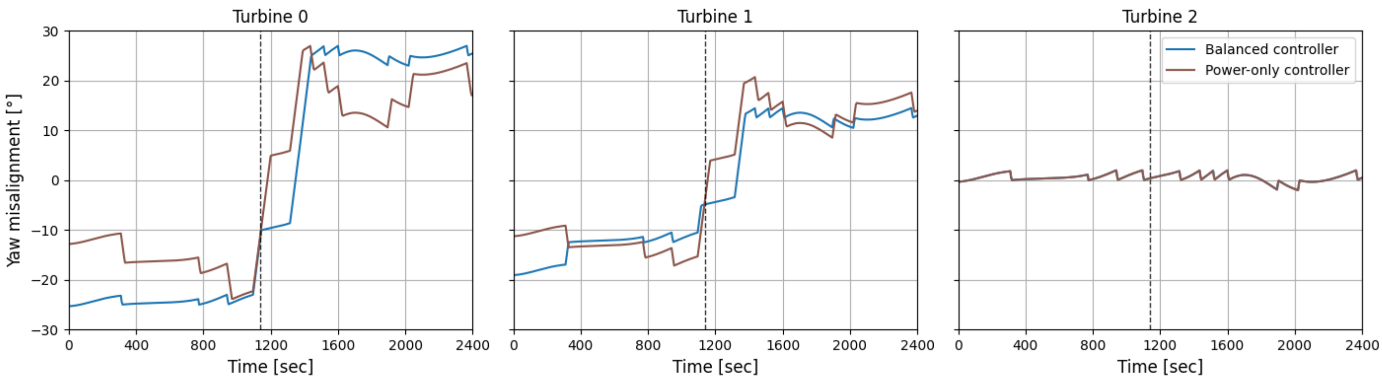

Figure E-3: Yaw misalignment angle trajectories for all three turbines for Segment 3 in OFF for the *power-only*, *balanced*, and *baseline controllers*.

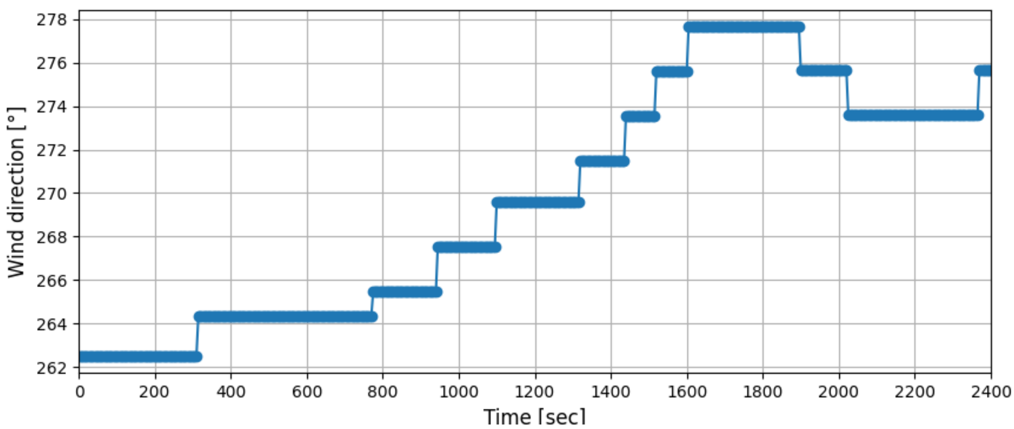

Figure E-4: The wind direction estimate of the controller for Segment 3 in OFF.

Bibliography

[1] A. King and L. Cassidy. "Earth Is Already Shooting through the 1.5°C Global Warming Limit, Two Major Studies Show". In: 2025. URL: https://theconversation.com/earth-is-already-shooting-through-the-1-5-c-global-warming-limit-two-major-studies-show-249133.

[2] European Environment Agency. "Share of energy consumption from renewable sources in Europe". In: 2025. URL: https://www.eea.europa.eu/en/analysis/indicators/share-of-energy-consumption-from.

[3] WindEurope. "Wind Energy in Europe: 2024 Statistics and the Outlook for 2025-2030". In: 2025. URL: https://windeurope.org/intelligence-platform/product/wind-energy-in-europe-2024-statistics-and-the-outlook-for-2025-2030/.

[4] M. Becker et al. "A dynamic open-source model to investigate wake dynamics in response to wind farm flow control strategies". In: 2024. DOI: 10.5194/wes-2024-150. URL: https://wes.copernicus.org/preprints/wes-2024-150/.

[5] B. Doekemeijer, D. van der Hoek, and J.-W. van Wingerden. "Closed-loop model-based wind farm control using FLORIS under time-varying inflow conditions". In: vol. 156. Elsevier Ltd, 2020, pp. 719–730. DOI: 10.1016/j.renene.2020.04.007.

[6] M. Howland, S. Lele, and J. Dabiri. "Wind farm power optimization through wake steering". In: vol. 116. 29. 2019, pp. 14495–14500. DOI: 10.1073/pnas.1903680116. URL: https://www.pnas.org/content/116/29/14495.

[7] P. Gebraad et al. "Maximization of the annual energy production of wind power plants by optimization of layout and yaw-based wake control". In: vol. 19. 1. 2016, pp. 95–107. DOI: 10.1002/we.1993. URL: https://doi.org/10.1002/we.1993.

[8] A. Guilloré, F. Campagnolo, and C. Bottasso. "A control-oriented load surrogate model based on sector-averaged inflow quantities: Capturing damage for unwaked, waked, wake-steering and curtailed wind turbines". In: *Journal of Physics: Conference Series*. Vol. 2767. Institute of Physics, 2024. DOI: 10.1088/1742-6596/2767/3/032019.

[9] A. Guilloré et al. *Surrogate Load Model / D2.1*. Technical Report. SUDOCO, 2025. URL: https://sudoco.eu.

[10] J. Liew et al. "Wind Farm Control Optimisation Under Load Constraints Via Surrogate Modelling". In: *Journal of Physics: Conference Series*. Vol. 2767. Institute of Physics, 2024. DOI: 10.1088/1742-6596/2767/9/092039.

[11] De Windcentrale. *Waarom verschilt de stroomproductie per windmolen?* 2024. URL: https://www.windcentrale.nl/blog/waarom-verschilt-de-stroomproductie-per-windmolen/.

[12] R. He et al. "Site-specific Wake Steering Strategy for Combined Power Enhancement and Fatigue Mitigation Within Wind Farms". In: *Renewable Energy*. Vol. 225. Elsevier, 2024, p. 120324. DOI: 10.1016/j.renene.2024.120324. URL: https://doi.org/10.1016/j.renene.2024.120324.

[13] S. Boersma et al. "A Tutorial on Control-Oriented Modelling and Control of Wind Farms". In: *Proceedings of the American Control Conference (ACC)*. 2017.

[14] J. Frederik et al. "The helix approach: Using dynamic individual pitch control to enhance wake mixing in wind farms". In: vol. 23. John Wiley and Sons Ltd, 2020, pp. 1739–1751. DOI: 10.1002/we.2513.

[15] M. Coquelet et al. "A reinforcement-learning approach for individual pitch control". In: vol. 25. John Wiley and Sons Ltd, 2022, pp. 1343–1362. DOI: 10.1002/we.2734.

[16] W. Munters and J. Meyers. "An optimal control framework for dynamic induction control of wind farms and their interaction with the atmospheric boundary layer". In: vol. 375. 2091. 2017, p. 20160100. DOI: 10.1098/rsta.2016.0100. URL: https://royalsocietypublishing.org/doi/10.1098/rsta.2016.0100.

[17] D. van den Berg et al. "Wake Mixing Control for Floating Wind Farms: Analysis of the Implementation of the Helix Wake Mixing Strategy on the IEA 15-MW Floating Wind Turbine". In: vol. 44. 5. 2024, pp. 81–105. DOI: 10.1109/MCS.2024.3432341. URL: https://doi.org/10.1109/MCS.2024.3432341.

[18] R. Balakrishnan and S. Hur. "Maximization of the Power Production of an Offshore Wind Farm". In: *Applied Sciences*. Vol. 12. 8. MDPI, 2022, p. 4013. DOI: 10.3390/app12084013. URL: https://doi.org/10.3390/app12084013.

[19] J. Meyers et al. "Wind Farm Flow Control: Prospects and Challenges". In: vol. 7. 2022, pp. 2271–2306. DOI: 10.5194/wes-7-2271-2022. URL: https://doi.org/10.5194/wes-7-2271-2022.

[20] J. Vitulli et al. "Optimal open loop wind farm control". In: vol. 1256. 1. 2019, p. 012027. DOI: 10.1088/1742-6596/1256/1/012027. URL: https://doi.org/10.1088/1742-6596/1256/1/012027.

[21] M. Becker et al. "Closed-loop model-predictive wind farm flow control under time-varying inflow using FLORIDyn". In: 2025. URL: http://arxiv.org/abs/2503.02790.

[22] J. Liew et al. "Model-free closed-loop wind farm control using reinforcement learning with recursive least squares". In: *Wind Energy*. John Wiley and Sons Ltd, 2023. DOI: 10.1002/we.2852.

[23] D. Madjidian and G. Andersson. "A Model-Free Approach to Wind Farm Control Using Game Theoretic Methods". In: vol. 21. 4. 2013, pp. 1207–1214. DOI: 10.1109/TCST.2013.2257780. URL: https://doi.org/10.1109/TCST.2013.2257780.

[24] P. Hulsman et al. "Assessing Closed-Loop Data-Driven Wind Farm Control Strategies within a Wind Tunnel". In: *The Science of Making Torque from Wind (TORQUE 2024)*. Vol. 2767. Journal of Physics: Conference Series. IOP Publishing, 2024, p. 032049. DOI: 10.1088/1742-6596/2767/3/032049. URL: https://doi.org/10.1088/1742-6596/2767/3/032049.

[25] National Renewable Energy Laboratory. *FLORIS Wake Models*. https://nrel.github.io/floris/wake_models.html. Accessed: 2025-11-17. 2023.

[26] S. Frandsen et al. "Analytical Modelling of Wind Speed Deficit in Large Wind Farms". In: vol. 9. 1-2. 2006, pp. 39–53. DOI: 10.1002/we.189. URL: https://doi.org/10.1002/we.189.

[27] M. Pedersen et al. "PyWake 2.5.0: An Open-Source Wind Farm Simulation Tool". In: 2023. URL: https://topfarm.pages.windenergy.dtu.dk/PyWake/.

[28] J. Schmidt et al. "FOXES: Farm Optimization and Extended Yield Evaluation Software". In: vol. 8. 86. 2023, p. 5464. DOI: 10.21105/joss.05464. URL: https://doi.org/10.21105/joss.05464.

[29] N. Jensen. "A Note on Wind Generator Interaction". In: Risø-M-2411. Roskilde, Denmark, 1983.

[30] M. Bastankhah and F. Porté-Agel. "Experimental and theoretical study of wind turbine wakes in yawed conditions". In: vol. 806. 2016, pp. 506–541. DOI: 10.1017/jfm.2016.595. URL: https://doi.org/10.1017/jfm.2016.595.

[31] T. Ishihara and G. Qian. "A New Gaussian-Based Analytical Wake Model for Wind Turbines Considering Ambient Turbulence Intensities and Thrust Coefficient Effects". In: vol. 177. 2018, pp. 275–292. DOI: 10.1016/j.jweia.2018.04.010. URL: https://doi.org/10.1016/j.jweia.2018.04.010.

[32] P. Chatelain et al. "Large Eddy Simulation of Wind Turbine Wakes". In: vol. 91. 3. 2013, pp. 587–605. DOI: 10.1007/s10494-013-9474-8. URL: https://link.springer.com/inproceedings/10.1007/s10494-013-9474-8.

[33] M. Churchfield et al. "A Large-Eddy Simulation of Wind-Plant Aerodynamics". In: *50th AIAA Aerospace Sciences Meeting including the New Horizons Forum and Aerospace Exposition*. American Institute of Aeronautics and Astronautics (AIAA). 2012. DOI: 10.2514/6.2012-537. URL: https://doi.org/10.2514/6.2012-537.

[34] L. Martínez Tossas, M. Churchfield, and S. Leonardi. "Large eddy simulations of the flow past wind turbines: actuator line and disk modeling". In: vol. 18. 6. 2014, pp. 1047–1060. DOI: 10.1002/we.1747. URL: https://doi.org/10.1002/we.1747.

[35] J. Meyers and C. Meneveau. "Large Eddy Simulations of Large Wind-Turbine Arrays in the Atmospheric Boundary Layer". In: *48th AIAA Aerospace Sciences Meeting Including the New Horizons Forum and Aerospace Exposition*. 2010. DOI: 10.2514/6.2010-827. URL: https://doi.org/10.2514/6.2010-827.

[36] S. Boersma et al. "A Control-Oriented Dynamic Wind Farm Flow Model: "WFSim"". In: *Journal of Physics: Conference Series*. Vol. 753. 2016, p. 032005. DOI: 10.1088/1742-6596/753/3/032005. URL: https://doi.org/10.1088/1742-6596/753/3/032005.

[37] M. Becker, D. Allaerts, and J.-W. Van Wingerden. "FLORIDyn - A dynamic and flexible framework for real-time wind farm control". In: *Journal of Physics: Conference Series*. Vol. 2265. Institute of Physics, 2022. DOI: 10.1088/1742-6596/2265/3/032103.

[38] T. Göçmen et al. “Possible Power of Downregulated Offshore Wind Power Plants: The PossPOW Algorithm”. In: vol. 22. 2. 2019, pp. 205–218. DOI: 10.1002/we.2279. URL: https://doi.org/10.1002/we.2279.

[39] J. Liew et al. “Extending the dynamic wake meandering model in HAWC2Farm: A comparison with field measurements at the Lillgrund wind farm”. In: vol. 8. Copernicus Publications, 2023, pp. 1387–1402. DOI: 10.5194/wes-8-1387-2023.

[40] J. Ainslie. “Calculating the flowfield in the wake of wind turbines”. In: vol. 27. 1-2. 1988, pp. 213–224.

[41] G. Larsen et al. “Dynamic Wake Meandering Modeling”. In: Risø-R-1607(EN). Denmark, 2007. URL: https://orbit.dtu.dk/files/7703042/ris_r_1607.pdf.

[42] J. Jonkman and K. Shaler. “FAST.Farm User’s Guide and Theory Manual”. In: NREL/TP-5000-78485. Golden, CO, 2021. URL: https://www.nrel.gov/docs/fy21osti/78485.pdf.

[43] T. Göçmen et al. “Data-driven wind farm flow control and challenges towards field implementation: A review”. In: vol. 216. Elsevier Ltd, 2025. DOI: 10.1016/j.rser.2025.115605.

[44] H. Gielen. *Review of Dynamic Wind Farm Flow Control with Load Surrogate Integration*. Tech. rep. TU Delft, 2025.

[45] M. Becker and M. Lejeune. “OFF: Open-source Framework for Flow Control”. In: 2024.

[46] M. Lejeune, M. Moens, and P. Chatelain. “A meandering-capturing wake model coupled to rotor-based flow-sensing for operational wind farm flow prediction”. In: vol. 10. 2022, p. 884068. DOI: 10.3389/fenrg.2022.884068. URL: https://doi.org/10.3389/fenrg.2022.884068.

[47] A. Niayifar and F.Porté-Agel. “Analytical Modeling of Wind Farms: A New Approach for Power Prediction”. In: *Energies*. Vol. 9. 9. MDPI, 2016, p. 741. DOI: 10.3390/en9090741. URL: https://doi.org/10.3390/en9090741.

[48] A. Jiménez, A. Crespo, and E. Migoya. “Application of a LES technique to characterize the wake deflection of a wind turbine in yaw”. In: *Wind Energy*. Vol. 13. 6. Journal article cited as inproceedings to satisfy template constraints. 2010, pp. 559–572. DOI: 10.1002/we.380. URL: https://doi.org/10.1002/we.380.

[49] A. Crespo and J. Hernández. “Turbulence characteristics in wind-turbine wakes”. In: *Journal of Wind Engineering and Industrial Aerodynamics*. Vol. 61. 1. Journal article cited as inproceedings to satisfy template constraints. 1996, pp. 71–85. DOI: 10.1016/0167-6105(95)00033-X. URL: https://doi.org/10.1016/0167-6105(95)00033-X.

[50] M. Bastankhah and F. Porté-Agel. “A new analytical model for wind-turbine wakes”. In: *Renewable Energy*. Vol. 70. Journal article cited as inproceedings to satisfy template constraints. 2014, pp. 116–123. DOI: 10.1016/j.renene.2014.01.002. URL: https://doi.org/10.1016/j.renene.2014.01.002.

[51] P. Gebraad et al. “Wind Plant Power Optimization through Yaw Control Using a Parametric Model for Wake Effects—A CFD Simulation Study”. In: *Wind Energy*. Vol. 19. 1. Wiley, 2014, pp. 95–114. DOI: 10.1002/we.1822. URL: https://doi.org/10.1002/we.1822.

[52] I. Katic, J. Højstrup, and N. O. Jensen. “A Simple Model for Cluster Efficiency”. English. In: *Proceedings of the European Wind Energy Association Conference and Exhibition (EWEC’86), Vol. 1*. Ed. by W. Palz and E. Sesto. European Wind Energy Association Conference and Exhibition, Rome, Italy, 6–8 October 1986. A. Raguzzi, 1987, pp. 407–410.

[53] J. Annoni et al. "Analysis of Control-Oriented Wake Modeling Tools Using Lidar Field Results". In: *Wind Energy Science*. Vol. 3. Copernicus Publications, 2018, pp. 819–831. DOI: 10.5194/wes-3-819-2018. URL: https://doi.org/10.5194/wes-3-819-2018.

[54] R. Riva et al. "Wind farm layout optimization with load constraints using surrogate modelling". In: vol. 1618. 4. 2020, p. 042035. DOI: 10.1088/1742-6596/1618/4/042035. URL: https://doi.org/10.1088/1742-6596/1618/4/042035.

[55] M. Bertelè et al. "Wind inflow observation from load harmonics". In: vol. 2. 2017, pp. 615–640. DOI: 10.5194/wes-2-615-2017. URL: https://doi.org/10.5194/wes-2-615-2017.

[56] N. Dimitrov. "Surrogate models for parameterized representation of wake-induced loads in wind farms". In: vol. 22. John Wiley and Sons Ltd, 2019, pp. 1371–1389. DOI: 10.1002/we.2362.

[57] H. Reyes et al. "Validation of a Lookup-Table Approach to Modeling Turbine Fatigue Loads in Wind Farms under Active Wake Control". In: vol. 4. 4. 2019, pp. 549–561. DOI: 10.5194/wes-4-549-2019. URL: https://doi.org/10.5194/wes-4-549-2019.

[58] H. Sutherland. "On the Fatigue Analysis of Wind Turbines". In: 1999. DOI: 10.2172/9460. URL: https://www.osti.gov/biblio/9460.

[59] P. Bortolotti et al. "IEA Wind TCP Task 37: Systems Engineering in Wind Energy - WP2.1 Reference Wind Turbines". In: 2019. URL: https://www.nrel.gov/docs/fy19osti/73492.pdf.

[60] F. Zahle et al. "Definition of the IEA Wind 22-Megawatt Offshore Reference Wind Turbine". In: 2024. DOI: 10.11581/DTU.00000317. URL: https://doi.org/10.11581/DTU.00000317.

[61] National Renewable Energy Laboratory (NREL). "OpenFAST: An open-source wind turbine simulation tool". In: 2023.

[62] G.-W. Qian and T. Ishihara. "A novel double-gaussian full wake model for wind turbines considering dependence on thrust coefficient and ambient turbulence intensity". In: vol. 391. 2025, p. 125859. DOI: 10.1016/j.apenergy.2025.125859. URL: https://doi.org/10.1016/j.apenergy.2025.125859.

[63] V. Pettas et al. *Health Model / D2.2*. Technical Report. SUDOCO, 2025. URL: https://sudoco.eu.

[64] S. Kanev. "Dynamic Wake Steering and Its Impact on Wind Farm Power Production and Yaw Actuator Duty". In: *Renewable Energy*. Vol. 146. Elsevier, 2020, pp. 9–15. DOI: 10.1016/j.renene.2019.06.064. URL: https://doi.org/10.1016/j.renene.2019.06.064.

[65] A. Anand et al. "Economic Lifetime-Aware Wind Farm Control". In: *Wind Energy Science Discussions*. Preprint; in review. 2025. DOI: 10.5194/wes-2025-67. URL: https://doi.org/10.5194/wes-2025-67.

[66] P. A. Fleming et al. "Serial-Refine Method for Fast Wake-Steering Yaw Optimization". In: *The Science of Making Torque from Wind (TORQUE 2022)*. Vol. 2265. Journal of Physics: Conference Series 1. IOP Publishing, 2022, p. 032109. DOI: 10.1088/1742-6596/2265/1/032109.

[67] R. Thedin et al. “Impact of Wake Steering on Loads of Downstream Wind Turbines at an Above-Rated Condition”. In: *The Science of Making Torque from Wind (TORQUE 2024)*. Vol. 2767. Journal of Physics: Conference Series. IOP Publishing, 2024, p. 032020. DOI: 10.1088/1742-6596/2767/3/032020. URL: https://doi.org/10.1088/1742-6596/2767/3/032020.

[68] E. H. Lingkan and O. R. H. Buxton. “An Assessment of the Scalings for the Streamwise Evolution of Turbulent Quantities in Wakes Produced by Porous Objects”. In: *Renewable Energy*. Vol. 209. Open Access. Elsevier, 2023, pp. 1–9. DOI: 10.1016/j.renene.2023.03.101. URL: https://doi.org/10.1016/j.renene.2023.03.101.

[69] D. Houck. “Review of Wake Management Techniques for Wind Turbines”. In: *Wind Energy*. Open Access Review Article. Wiley, 2021. DOI: 10.1002/we.2668. URL: https://doi.org/10.1002/we.2668.

[70] S. Knoop. *Wind – Lidar Wind Profiles Measured at North Sea Wind Farm TenneT Platforms: 1-Second Raw Data*. Dataset, data.europa.eu. Accessed via: https://data.europa.eu/data/datasets/57583-wind-lidar-wind-profiles-measured-at-north-sea-wind-farm-tennet-platforms-1-second-raw-data?locale=no. 2019.

[71] M. Van Den Broek et al. “Dynamic wind farm flow control using free-vortex wake models”. In: vol. 9. Copernicus Publications, 2024, pp. 721–740. DOI: 10.5194/wes-9-721-2024.

[72] F. Zhang et al. “Evaluation of Aging Characteristics in Wind Turbine Performance Based on Yaw Power Loss”. In: *Sustainable Energy Technologies and Assessments*. Vol. 72. Elsevier, 2024, p. 104094. DOI: 10.1016/j.seta.2024.104094. URL: https://doi.org/10.1016/j.seta.2024.104094.

[73] A. Miner. “Cumulative Damage in Fatigue”. In: *Journal of Applied Mechanics* 12.3 (1945), A159–A164. DOI: 10.1115/1.4009458.

[74] K. Kragh and M. Hansen. “Load Alleviation of Wind Turbines by Yaw Misalignment”. In: *Wind Energy*. Vol. 17. 7. Wiley, 2014, pp. 971–982. DOI: 10.1002/we.1612. URL: https://doi.org/10.1002/we.1612.

[75] J. Li et al. “Typhoon Resistance Analysis of Offshore Wind Turbines: A Review”. In: *Atmosphere*. Vol. 13. 3. MDPI, 2022, p. 451. DOI: 10.3390/atmos13030451. URL: https://doi.org/10.3390/atmos13030451.

[76] M. Lara et al. “Analysis of Adaptive Individual Pitch Control Schemes for Blade Fatigue Load Reduction on a 15 MW Wind Turbine”. In: *Applied Sciences*. Vol. 14. 1. MDPI, 2024, p. 183. DOI: 10.3390/app14010183. URL: https://doi.org/10.3390/app14010183.

[77] T. Knudsen, T. Bak, and S. Tabatabaeipour. “Detection of Excessive Wind Turbine Tower Oscillations Fore-Aft and Sideways”. In: *Proceedings of the American Control Conference (ACC)*. IEEE, 2012, pp. 3822–3827. DOI: 10.1109/ACC.2012.6314930. URL: https://doi.org/10.1109/ACC.2012.6314930.

[78] R. Thedin et al. “Load Assessment of a Wind Farm Considering Negative and Positive Yaw Misalignment for Wake Steering”. In: *Wind Energy Science Discussions*. Preprint, discussion started: 23 January 2024. 2024. DOI: 10.5194/wes-2024-6. URL: https://doi.org/10.5194/wes-2024-6.

Glossary

List of Acronyms

WFFC	Wind Farm Flow Control
LuT	Look-up Table
MPC	Model Predictive Control
LES	Large Eddy Simulation
AEP	Annual Energy Production
SCADA	Supervisory Control and Data Acquistion
LiDAR	Light Detection and Ranging
FLORIS	FLOw Redirection and Induction in Steady-state
FLORIDyn	FLOw Redirection and Induction Dynamics
SOWFA	Simulator for Offshore Wind Farm Applications
NREL	National Renewable Energy Laboratory
CFD	Computational Fluid Dynamics
LES	Large Eddy Simulation
TUM	Technical University of München
ANN	Artificial Neural Network
SAWS	Sector-averaged wind speeds
SATI	Sector-averaged turbulence intensities
DEL	damage equivalent load
DWM	dynamic wake meandering
OP	Observation Point
TWF	Temporary Wind Farm
RMSE	root-mean-squared-error
MPC	model-predictive control
UTDWF	UTD Wind Farm

TI	turbulence intensity
RMSPE	root mean squared percentage error
SAIQs	sector-averaged inflow quantities
SR	Serial Refine
SOSFS	Sum of Squares Freestream Superposition
HKN	Hollandse Kust Noord
TB	tower base